CHARLES UNIVERSITY PRAGUE

Faculty of Mathematics and Physics

Department of Low-Temperature Physics

Investigation of Crystal Lattice Defects in Deformation and Irradiation Damaged Solids by Means of Positron Annihilation

Jakub Čížek

Doctoral Thesis

Prague, 2001

Acknowledgment

Contents

1 Introduction

The aim of the present work consists in investigation of metallic materials damaged by irradiation or plastic deformation by means of positron annihilation spectroscopy (PAS). The scientific work performed in the present thesis involves methodological development of positron-lifetime (PL) spectroscopy and application of PAS to study of reactor pressure vessel (RPV) steels and ultra-fine grained (UFG) metals. The investigations of RPV steels and UFG metals in the present work was accompanied also by development of theoretical models of positron behavior in these materials. The PAS studies of RPV steels and UFG materials were correlated with other methods as transmission electron microscopy (TEM) and X-ray diffraction (XRD). Moreover, further aim of the present work was an attempt to popularize PAS especially among students of solid state physics and wide group of other people who are interested in modern powerful methods in for characterization of condensed matter.

PAS is a well established experimental technique for microstructure characterization of solids [1, 2]. PAS represents non-local and non-destructive method with high sensitivity to open-volume defects as vacancies, vacancy clusters, voids, dislocations, grain boundaries etc. The high sensitivity is due to positron trapping in the open-volume lattice defects. Information about type of defects, their density, local electronic structure as well as arrangement can be obtained by PAS. It has to be pointed out that PAS provides unique information about point defects (vacancies, vacancy clusters), which can hardly be obtained by other techniques due to small size of these defects. Another important advantage of PAS consists in fact that well developed theory of positron annihilation especially for metals is available [3]. Hence, experimental results can be directly compared with theoretical predictions of various models of studied material. In order to obtain complete description of microstructure of some material, it is necessary to accompany PAS with some other independent experimental techniques, e.g. TEM, XRD or microhardness measurements, complementary information of those was used in the present work.

The investigations regarding methodology of PL spectroscopy performed in the present work cover study of processes, which cause deterioration of timing properties of PL spectrometer during its long-time operation. Attempt to find ways how to remedy this undesirable worsening of timing properties was successful. Explanation of the deterioration processes and procedures of their remedy are explained in appendix A. Moreover, alternative configuration of conventional fast-slow PL spectrometer was developed and tested in the present work. The difference from conventional configuration consists in use of sum of energy signals in the slow branch, which remarkably improves throughput of the spectrometer with no worsening of timing properties. Description of this technique can be found in appendix B. The second main part of methodological work made in the present thesis was development and building of three-detector PL spectrometer, which uses is able to recognize triple coincidences of γ-rays connected with positron annihilation (the start γ and the two annihilation γ) and, therefore, strongly suppress the prompt peak contribution of ^{60}Co nucleus in PL spectrum. Use of such PL spectrometer is inevitable for investigation of neutron irradiated RPV steels. Detailed description of the three-detector PL spectrometer developed in the present work is given in appendix C.

It is economically desirable to extend the service life of nuclear reactors. One of the main factors, which limit lifetime of reactors, is radiation-induced embrittlement of the RPV steels. Irradiation of RPV by fast neutrons (E > 5 MeV) during operation of reactor causes significant changes of microstructure of the RPV steels, which, consequently, substantially affect their mechanical properties [4]. One of the fundamental demand, to assure the RPV integrity during whole operation period under all conceivable operation conditions, is to understand the neutron-induced degradation of RPV materials in terms of microstructural characterization. Despite a number of techniques including TEM, atom-probe field ion microscopy (APFIM), small-angle neutron scattering (SANS) anomalous small angle X-ray scattering (ASAXS) etc., employed in characterization of radiation-induced changes of microstructure of RPV steels, nature of radiation-induced

defects and microstructural changes, which lead to deterioration of mechanical properties (embrittlement), is not yet clear [5]. From investigations already performed by other authors, it can be concluded that point defects (vacancies and vacancy clusters) and fine precipitates (size ≤ 5 nm) created due to neutron irradiation and their mutual interaction play key role in the radiation-induced microstructural changes. PAS is highly sensitive to vacancies and vacancy clusters and under some conditions also to the fine precipitates and represents, therefore, ideal tool for study of radiation-induced microstructural changes. In the present work Western type of RPV steels as well as Eastern VVER-type steels were studied. Results of PAS investigations of radiation-induced changes of microstructure of studied RPV steels are given in chapter 4 and appendixes E, G and H. Firstly, it was necessary to make complete description of microstructure of non-irradiated RPV steels using PAS correlated with TEM. Results of this investigations of various RPV steels are shown in appendix E. Results investigations of the RPV steels irradiated at various conditions (neutron fluence, flux) are described in appendix G and H.

Nanocrystalline and UFG materials are polycrystals with the mean grain size about 10 and 100 nm, respectively. These materials attract high interest among researchers due to their unusual physical and mechanical properties connected with significant volume fraction of grain boundaries (GBs) [6]. Recently, a new technique based on severe plastic deformation (SPD) was developed [7, 8] This technique provides UFG materials with grain size between 50 and 150 nm. Contrary to the other preparation techniques, the UFG materials prepared by SPD are bulk specimens, which contain no gas impurities. Both the UFG materials prepared by SPD and NC ones prepared by conventional techniques as gas condensation method (GCM) exhibit a number of similar physical properties. On the other hand, microstructure of the UFG and the NC materials differs substantially due to completely different ways of preparation. PAS has proved itself as valuable tool for investigation of microstructure of NC materials prepared by GCM [9, 10]. These investigations have revealed that open-volume point defects represent important structure elements of these materials. However, there is still lack PAS data for UFG materials prepared by SPD. Therefore, PAS and TEM investigations of microstructure of UFG Cu and Ni prepared by SPD were performed in the present work and the obtained results are explained in chapter 5 and appendixes I, J and K.

Important topic in study of UFG and NC materials consists in investigation of their thermal stability, i.e. study of evolution of microstructure with increasing temperature. It is interesting from physical pint of view, as one obtains information about recovery of highly non-equilibrium structure. Moreover, information about thermal stability is highly important also for further exploitation of these materials in industry because their advantageous properties are connected with the UFG structure. Detailed investigations of processes, which take place during thermal recovery of UFG structure of Cu and Ni were studied in the present work. Complete description of changes of microstructure was achieved using PL spectroscopy correlated with other methods (TEM, XRD). The obtained results are explained in chapter 5 and appendixes I, J and K.

Common feature of the RPV steels and UFG materials studied in the present work is complex microstructure with relatively high number of lattice defects. Dislocations represent main type of defects in both kind of materials. Moreover, both in the case of RPV steels and UFG materials, spatial distribution of the dislocations is strongly inhomogeneous. In both kind of studied materials, regions of various sizes with relatively low number of dislocations are separated by distorted layers with high dislocation density. Because of this strongly inhomogeneous arrangement of dislocations, it is not possible to use the simple trapping model (STM) [2] for interpretation of measured PL data, see appendixes F and J. Therefore, theoretical models, which takes into account specific microstructure of the studied materials, were developed and successfully applied in the present work. Complete description of these models, which allow for proper determination of defect densities as well as some other important physical parameters of the studied specimens, can be found in appendixes F, I and J.

Finally, the last part of the present work was devoted to popularization of PAS among students of physics as well as wide group of people interested in physics of condensed matter. It seems to be desirable, as after rapid development PAS becomes an experimental technique routinely used especially for investigation of defects in solids. However, there is still relatively poor knowledge

about PAS and its principles and possibilities among solid-state physicists. In order to improve this situation short and intelligible introduction to PL spectroscopy with explanation of its principles, experimental configuration and interpretation of results with respect to investigations of metallic materials was elaborated in the present work, see appendix L. This paper, which represents first publication of this kind regarding popularization of PL spectroscopy in Czech language, was published in journal "Pokroky matematiky fyziky a astronomie" accessible to relatively wide group of readers including physical students and other people interested in attractive topics of physics.

2 Physical principles of positron annihilation spectroscopy

When a positron is emitted from a source, and penetrates into a solid, it quickly decreases its kinetic energy to thermal energy. Thermalized positron moves in the solid by diffusion and finally annihilates with one of environment electrons. The whole energy of electron-positron annihilation pair is converted to two annihilation γ-rays which may be detected. The annihilation rate of a positron is determined by local electron density in site of the positron. Thus, positron serves as probe of local electronic structure of solids. Moreover a positron may be trapped by some defects in a solid due to decrease of repulsion between positron and positive ions at these defects. Therefore positron annihilation spectroscopy (PAS) provide also valuable information about electronic structure of defects. In addition identification of defects in solids as well as determination of their concentration is possible using PAS. The details of positron interaction with metallic materials will be explained in next sections.

2.1 Positron sources

Positrons for PAS measurements are usually obtained from β^+-radioactive sources. The β^+- decay is described by reaction

$$\underset{Z}{\overset{A}{}}X \rightarrow \underset{Z\text{-}1}{\overset{A}{}}X^{\text{`}} + e^+ + \nu, \tag{2.1}$$

where Z and A denote atomic and mass number, respectively. Parent nucleus $\underset{Z}{\overset{A}{}}X$ decays into daughter nucleus $\underset{Z\text{-}1}{\overset{A}{}}X^{\text{`}}$. The decay is accompanied by emission of positron e^+ and neutrino ν. A basic characteristics of β^+- decay is the continuous energy spectrum of the positron. This is because the available energy for the decay (Q-value) is shared between the positron and neutrino which usually goes undetected. Kinetic energy E of the emitted positron cannot be greater than so called end-point energy $E_{max} = Q - 2mc^2$. Energy distribution of the emitted positrons may be approximated by the formula [11]

$$\frac{dN}{dE} = D\sqrt{E(E + 2mc^2)}(E + mc^2)(E_{max} - E)^2, \tag{2.2}$$

where m is positron rest mass and D is a normalization coefficient. It should be pointed out that Coulombic interaction between the flying out positron and the nucleus is neglected in (2.2). The emitted positrons are accelerated by repulsive Coulombic interaction with the nucleus. It causes slight enhancement of the distribution in high energy part and on the other hand decrease in low energies. When one takes into account this effect, coefficient D becomes dependent on positron energy and atomic number of the nucleus $D = D(E, Z)$.

For many β^+- sources the daughter nucleus is left after emission of e^+ and ν in excited state which deexcitates almost immediately via the emission of one or more γ photons. These secondary photons are used in positron lifetime measurements for determination of time when the positron was emitted (see section 3.1). Basic properties of useful positron sources important for application in PAS are listed in Tab. 2.1. It includes half-life of the source in the first column and positron yield, i.e. probability that positron will be emitted in given decay, in the second column. End-point energy of the emitted positron is shown in the third column and energies of secondary γ rays are given the next column. Number of γ rays per positron is evaluated in the last two columns. The photons are divided into the secondary photons, i.e. the photons that coincide with emitted positron, and the other ones which do not coincide with the positron.

Nuclear level diagram of ^{22}Na β^+- source, which is widely used in PAS, is shown in Fig .2.1. The shape of energy spectrum of positrons for ^{22}Na source described by the formula (2.2) is given in Fig. 2.2.
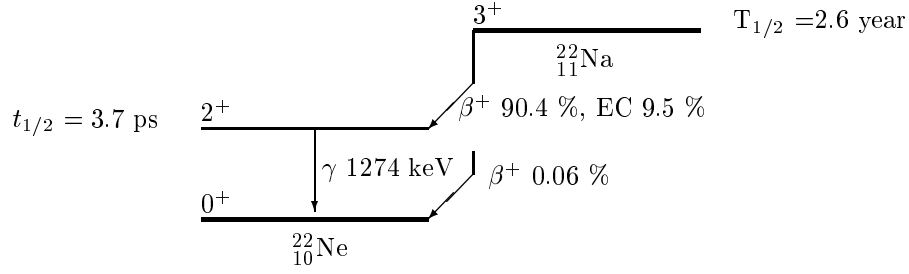
Figure 2.1 ^{22}Na decay scheme [12].

Table 2.1 Properties of some useful positron sources [13]

Isotope	Half-life	Positron yield	End-point energy [MeV]	Energy of secondary γ-ray [MeV]	γ-rays per positron secondary	others
^{13}N	9.96 min	1	1.20	–	0	0
^{15}O	123 s	1	1.74	–	0	0
^{18}F	110 min	0.97	0.635	–	0	0
^{19}Ne	17.4 s	1	2.22	–	0	0
^{22}Na	2.6 y	0.9	0.545	1.274	1	0.11
^{26}Al	8×10^5 y	0.85	1.17	1.81	1	0.11
^{44}Ti	47 y	0.94	1.47	1.156	1	0.08
^{48}V	16 d	0.50	0.696	$1.312 + 0.983$	2	2.2
^{58}Co	71 d	0.15	0.474	0.811	1	5.8
^{57}Ni	36 h	0.46	0.85	1.37	1	1.15
^{64}Cu	12.8 h	0.19sotopeCu64	12.8 h	0.19		
^{68}Ge	275 d	0.88	1.90	1.078	0.017	0.03
^{89}Zr	79 h	0.22	0.90	–	0	2.5

2.2   Positron thermalization

Typical kinetic energy of positron emitted by radioactive nuclei is of order of $\sim 10^2$ keV, see Tab. 2.1 and eq. (2.2). Energetic positrons in condensed media rapidly lose their energy. In condensed medium positrons slow down to thermal energies $E \approx kT$, where k is the Boltzman constant.

At highest positron energies ($E > 10^2$ eV) the most important processes are elastic ion core scattering and inelastic scattering off both core and valence electrons [14, 15]. In the case of metals the excitations of conduction electrons dominates at lower energies (0.1 eV $< E < 10^2$ eV) [16]. Finally, when the positron energy has degraded to a fraction below ~ 0.1 eV, scattering off phonons prevails [14, 17].

Simple model of positron thermalization in metals is presented in [18]. I use this approach for estimation of positron thermalization times for the metals which are considered in this work.

Positron energy loss per unit distance in the medium may be expressed by the *stopping power*

$$S = -\frac{dE}{dx}.\tag{2.3}$$

5
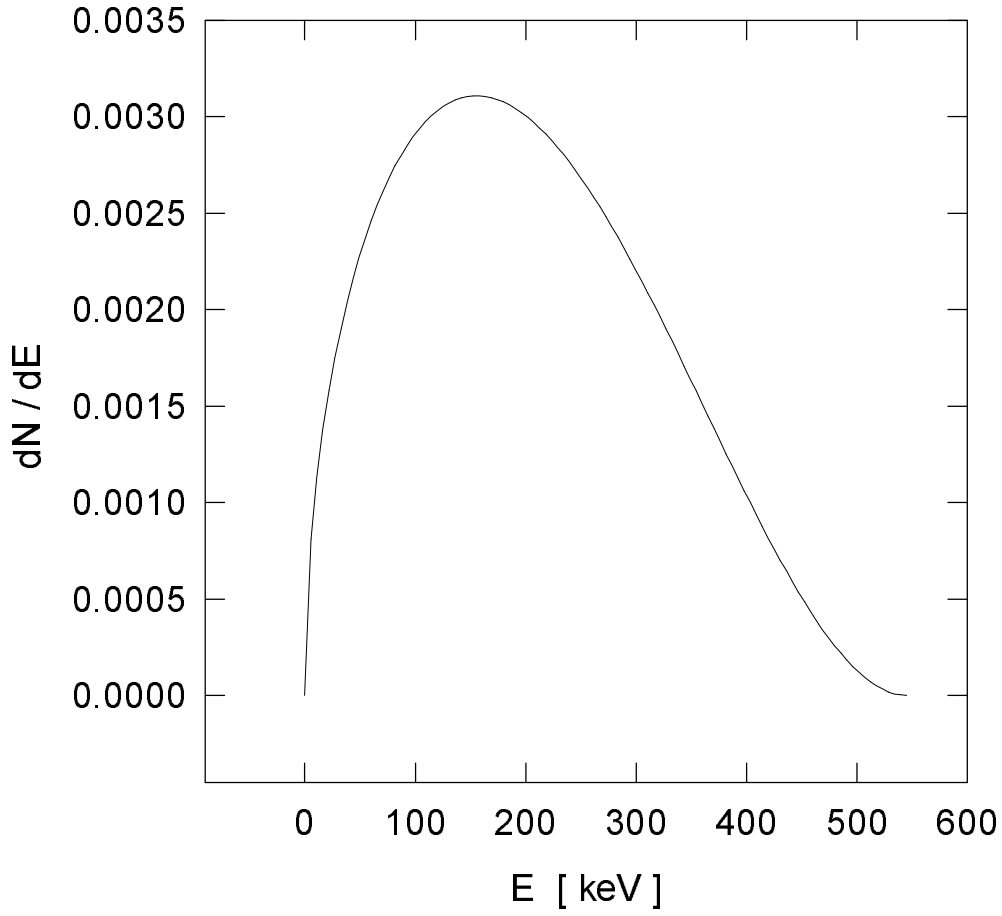
Figure 2.2 Energy distribution of positrons emitted by ^{22}Na source.

The stopping power is usually calculated in terms of "continuous slowing – down approximation", according to which energy losses occur almost continuously in small portions through collisions with electrons in the medium. Hence this approximation neglects the link between energy change and momentum (directional) change induced by collisions.

Slowing – down time of positron from initial energy E_i to final energy E_f is

$$t = -\sqrt{\frac{m}{2}} \int_{E_i}^{E_f} \frac{dE}{\sqrt{E}S}. \tag{2.4}$$

The stopping power S differs from that of heavy particles or electrons by the fact that positrons are light but distinguishable from electrons. The stopping power for positrons reaches its maximum at energy E_m. Positron stopping times t_s in the highest energy region ($E > E_m \sim 10^2$ eV) may be estimated very accurately with the formula [18]

$$t_s \text{ [ps]} \simeq \frac{17.2}{d \text{ [g/cm}^3\text{]}} E_i^{1.2} \text{ [MeV]}, \tag{2.5}$$

where d is density of the medium. End-point energy of emitted positrons may be treated as E_i for estimation of maximum t_s. Since β^+- sources of interest emit positrons with $E_i > 0.5$ MeV, it is clear that $t_s \leq 1$ ps in all metals. Thus t_s values are very short compared to lifetime τ_B of free positrons. In metals the lifetime τ_B lies in interval 100 ps $< \tau_B <$ 200 ps (see section ..). The

6

stopping times t_s for the materials of interest in this work are shown in Tab. 2.2, where I used end-point energy for ^{22}Na (see table 2.1).

Further energy losses of positron with energy $E < 10^2$ eV are caused mainly by excitations of conduction electrons. Stopping power S_R for excitations of conduction electrons was derived by Ritchie [16] for positrons in a conduction electron gas with Fermi energy E_F

$$S_R = \frac{2\pi}{105} \frac{m}{\hbar} \sqrt{\frac{2}{m}} \frac{E^{5/2}}{E_F}. \tag{2.6}$$

Equation (2.6) yields for positron slowing $-$ down time t_R to energy $E_f \ll E_m$

$$t_R = \frac{105}{8\pi} \frac{\hbar}{E_f^2} \frac{E_F}{E_f^2}. \tag{2.7}$$

Finally when positron energy decreases to a fraction of an eV scattering off longitudinal acoustic phonons dominates [14, 19, 17].

The formula for positron stopping power S_{ph} for phonon excitations is given in [18]. The notion of S_{ph} is based on a continuum representation of the material. The local atomic structure is ignored. Deformation potential energy W, which is related to the energy necessary to deform the medium locally, is introduced. This quantity is not well defined and is model dependent. The phonon stopping power of the medium of density d

$$S_{ph} = \frac{2}{\pi} \frac{m^3 W^2}{d \, \hbar^4} E \tag{2.8}$$

is proportional to W^2, which makes S_{ph} sensitive to the choice of W. A relation appears to exist between the deformation potential W and Fermi energy E_F

$$W = bE_F. \tag{2.9}$$

Depending on the model, the constant b can have values between 2/5 and 2/3. In the following calculations I set $b = 0.575$ [18].

Table 2.2   Positron thermalization times.
[a] The values of E_F were obtained from [18].
[b] The values of t_s belong to ^{22}Na β^+- source , i.e. end-point energy $E_{max} = 0.545$ MeV.
[c] Thermalization times t_{ph} and t_t correspond to room temperature $T = 20$ $^\circ$C.

metal	d [g/cm^3]	$^a E_F$ [eV]	E_c [eV]	$^b t_s$ [ps]	t_R [ps]	$^c t_{ph}$ [ps]	$^c t_t$ [ps]
Cu	8.96	14.96	0.12	0.93	2.86	8.92	12.71
Fe	7.86	11.69	0.08	1.06	5.02	9.10	15.18
Al	2.70	11.15	0.15	3.08	1.56	5.76	10.40
Ni	8.90	15.46	0.13	0.94	2.52	8.60	12.05
V	6.10	17.75	0.21	1.36	1.11	6.02	8.49
Cr	7.19	20.85	0.26	1.16	0.85	5.51	7.52

Dependence of S_R and S_{ph} on positron energy is shown in Figs. 2.3, 2.4, 2.5 for Cu, Fe and Al. Clearly there is some critical energy E_c. Phonon scattering dominates for $E < E_c$ while the most
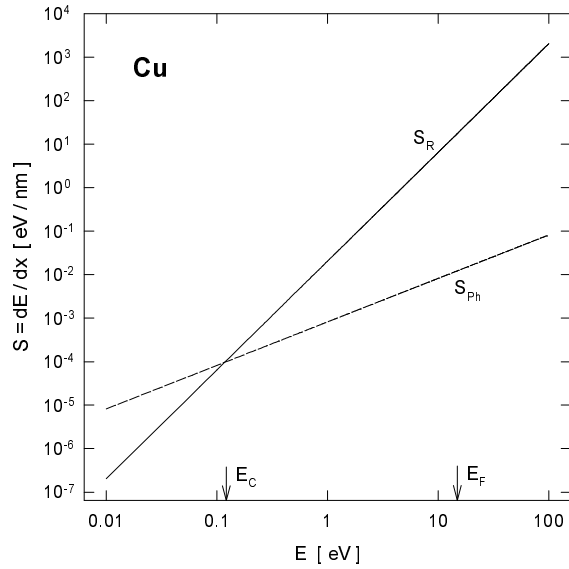
Figure 2.3 Dependence of stopping power on positron energy for Cu.

important process for $E > E_c$ appears to be excitations of conduction electrons. Critical energy E_c may be obtained from equation

$$S_{ph}(E_c) = S_R(E_c). \tag{2.10}$$

Using of expressions (2.6, 2.8) gives

$$E_c = \left(\frac{105\, b^2}{\sqrt{2}\pi^2} \frac{m^{5/2} E_F^3}{d\, \hbar^3} \right)^{2/3}. \tag{2.11}$$

Values of E_c for some metals are shown in Tab. 2.2.

Thermalization time t_R in energy region $E_c \leq E < E_m$ where excitations of conduction electrons play dominant role may be calculated from equation (2.7) with substitution $E_f = E_c$. Integration of equation (2.4) with (2.8) over the range $\frac{3}{2}kT \leq E \leq E_c$ yields the phonon scattering thermalization time t_{ph}

$$t_{ph} = 4\, t_R \left(\sqrt{\frac{E_c}{\frac{3}{2}kT}} - 1 \right). \tag{2.12}$$

Increasing temperature results in slow decrease of t_{ph}. Temperature dependence of t_{ph} for the metals considered in this work i.e. Cu, Al, Fe, V, Ni and Cr is shown in Fig. 2.6. Thermalization times t_R, t_{ph} are collected in Tab. 2.2. Values of t_{ph} correspond to room temperature $T = 20\ ^\circ C$. Total thermalization time

$$t_t = t_s + t_R + t_{ph} \tag{2.13}$$

is shown in the last column of Tab. 2.2.

Thermalization times for slowing-down process of positrons with $E < E_m$ were calculated in [17] by solving the Boltzmann equation for the positron momentum distribution in a homogeneous medium. Positron scattering off conduction electrons and phonons were included. It was found that the approach of positron energy E to thermal energy $\frac{3}{2}kT$ is very close to exponential function when $E < 3kT$. In the case of Al the times needed to reach mean energies of 1.01 $\frac{3}{2}kT$ and 1.001 $\frac{3}{2}kT$ are 5.65 ps and 8.38 ps, respectively, at room temperature. Note that these results are in surprisingly good agreement with the simple model used here which for Al gives (Tab. 2.2) $t_R + t_{ph} = 7.32$ ps.

8
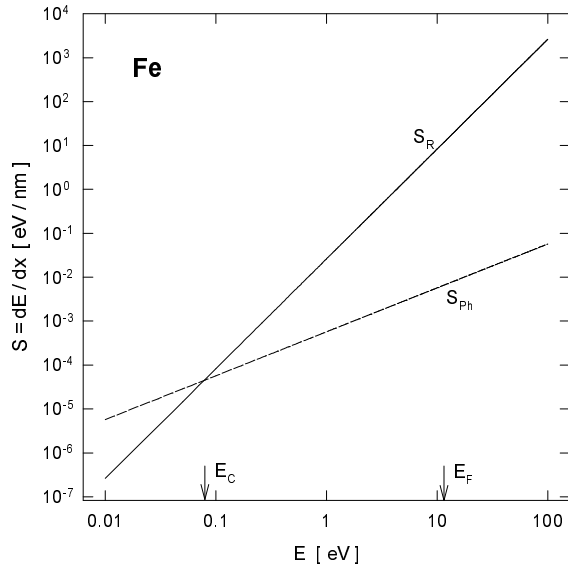
Figure 2.4   Dependence of stopping power on positron energy for Fe.

One can immediately conclude that thermalization times are very short compared to positron bulk lifetimes τ_B. The fact that positron reach very quickly thermal energies is important for application of the positron method. Clearly only thermalized positrons annihilate. Hence momenta of positrons are very small compared to the momenta of electrons with which they annihilate.

It is evident from Tab. 2.2 that positron scattering off phonons occupies more than 50 % of thermalization time. Hence positron spends the main part of slowing-down process with energy slightly above the thermal energy. This fact is important for possible trapping of non-thermalized positrons.

2.3   Positron stopping profile

The penetration of high energy positrons emitted from β^+- source into a solid can be described by an empirical law [20]. It states that depth distribution of positrons in a solid after thermalization has form

$$P(z) = \alpha e^{-\alpha z}, \qquad \alpha \ [\text{cm}^{-1}] \approx 16 \frac{d \ [\text{g/cm}^3]}{E_{max}^{1.4} \ [\text{MeV}]}, \tag{2.14}$$

where E_{max} is end-point energy of emitted positrons and d denotes density of the material.

Thus probability that positron penetrates into the material at the depth z, measured from the surface of the specimen faced the β^+- source , decays exponentially with the depth.

Mean penetration depth of positrons into material is

$$\int_0^\infty P(z)\,dz = \frac{1}{\alpha}. \tag{2.15}$$

The positron mean penetration depths into the metals investigated in this work are presented in Tab. 2.3, where ^{22}Na β^+- source is considered. Thus positrons from a nuclear β^+- emitter annihilate in the solid within a depth of the order of hundreds μm and therefore they probe bulk properties of the specimen. The approximation (2.14) for the penetration depth is an important planning parameter for the samples in PAS.

9

Figure 2.5 Dependence of stopping power on positron energy for Al.

2.4 Positronium Formation

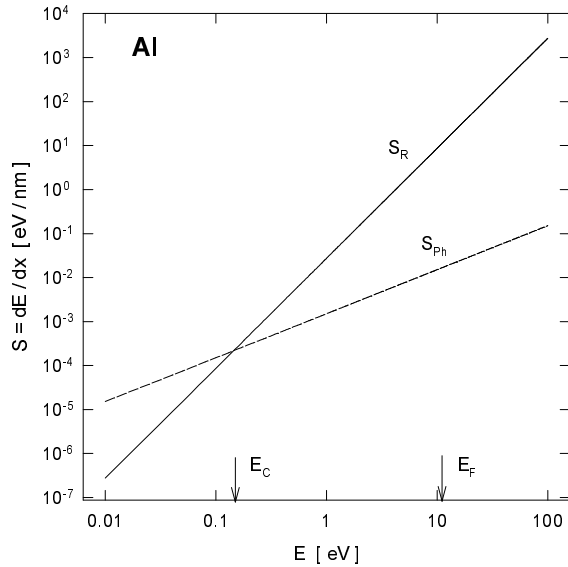A positron in a solid can capture an electron from the surrounding medium and a positronium atom (Ps), the bound state of the positron-electron pair, is formed. As the size of Ps is twice that of the hydrogen atom, Ps formation occurs mainly in molecular media with relatively open structures. Tight bound structure of metals causes that usually there is no Ps formation. Nevertheless Ps was observed in nanocrystalline metals prepared by compactization of ultrafine powders (see section 5.1) [6, 10, 9].

Formation of Ps is possible during thermalization of positron and it may be described by so called *Ore gap model*.[24] It states that Ps formation is most probable when the positron energy during its slowing-down lies within a gap where no other electronic energy transfer process is possible. To capture an electron from a molecule of the medium with ionization energy E_i, the kinetic energy E of the positron must be greater than $E_i - E_{Ps}$, where E_{Ps} is the binding energy of Ps. In vacuum E_{Ps} is 6.8 eV but may be smaller in the medium. When $E > E_i$ the Ps is formed with kinetic energy greater than its binding energy and it will rapidly break up in collisions. Furthermore inelastic collisions will compete with Ps formation until the positron energy is less then E_{ex}, the lowest excitation energy. Thus Ps formation is most probable for positron with energy

$$E_i - E_{Ps} < E < E_{ex}. \tag{2.16}$$

This energy interval is called the *Ore gap*. In metals excitation of conduction electrons competes with Ps formation. It is the next reason why Ps are not formed in metals.

Thermalized positrons may also form Ps by capture of free electron created by ionization during positron thermalization [25, 26]. This is so called *spur mechanism* . In metals however mutual shielding of conduction electrons does not allow formation of bound state of positron with individual conduction electron. Hence Ps formation in conventional metals does not occur by Ore mechanism nor by spur mechanism.

The ground states of Ps are the singlet 1^1S_0 state (*parapositronium* p-Ps) and the triplet 1^3S_1 state (*orthopositronium* o-Ps). Probability that Ps will be formed in the singlet state is 1/4 while
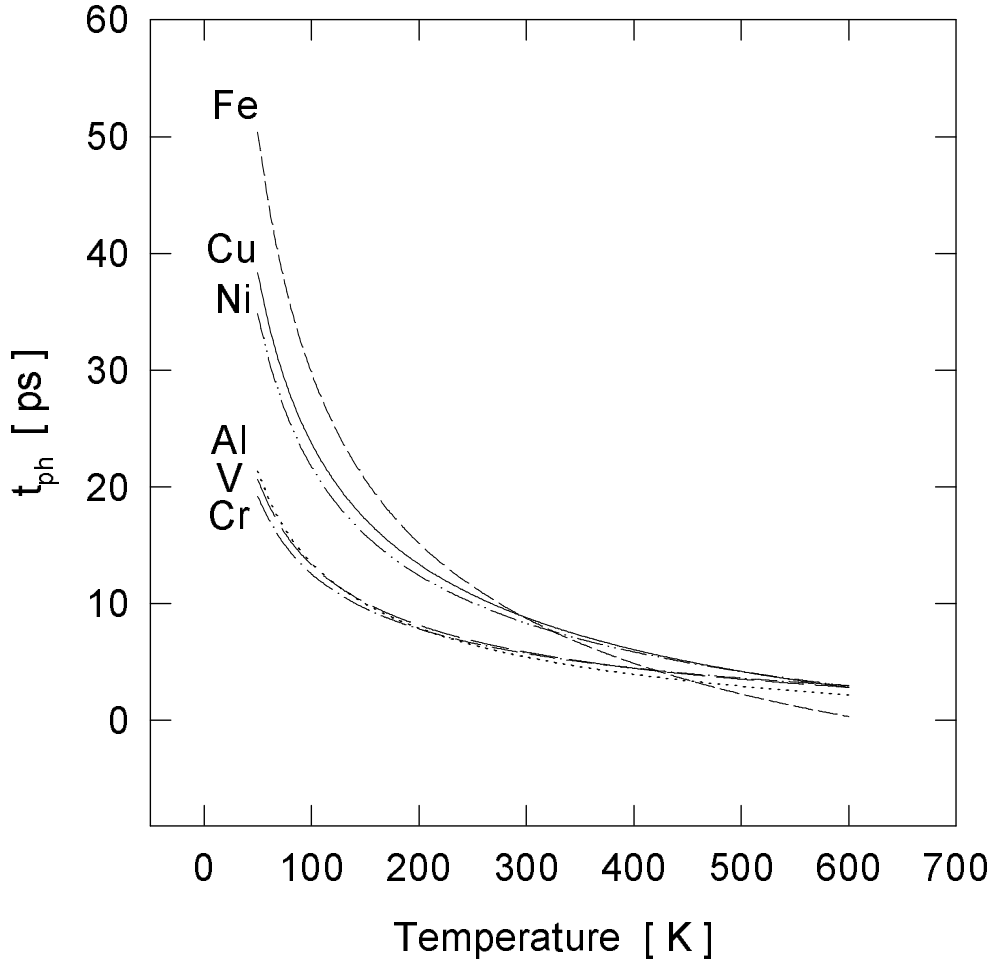
Figure 2.6   Temperature dependence of phonon thermalization time t_{ph} for some metals.

it is 3/4 for the triplet state. In vacuum, the lifetime of p-Ps in self-annihilation into two phonons is 125 ps i.e. about the same as free positron lifetime in dense metals. In the case of o-Ps self-annihilation into two phonons is forbidden by selection rules [24]. Thus in vacuum o-Ps decays via three-photon emission with the lifetime 142 ns, which is more than three orders of magnitude longer than the p-Ps lifetime. In the condense matter, however, o-Ps decays by competing mechanism which is called *pick off* annihilation. In the pick-off process the positron of o-Ps suffers 2γ-annihilation in collision with a "foreign" electron having opposite spin. Consequently, the o-Ps lifetime in condensed materials is reduced to a few nanoseconds.

2.5   Positron in thermal equilibrium

When positron has reached thermal equilibrium with the medium, its scattering is overwhelmingly dominated by phonons. This scattering is usually quasielastic and does not affect the average positron momentum distribution. Thus the momentum distribution of thermalized positron has

Table 2.3 Important quantities connected with positron movement in metals.
[a] ^{22}Na β^+- source is assumed, i.e. end-point energy $E_{max} = 0.545$ MeV.
[b] The mean free path at room temperature $T = 300$ K.
[c] The positron diffusion coefficient at room temperature. In the case of experimental values PD = positron depolarization experiment, DB = Doppler broadening measurement of the annihilation line-shape parameter S, Ps = positronium fraction measurement.
[d] The mean diffusion length at room temperature for defect-free material. As free positron lifetimes we used the bulk lifetimes calculated by GGA and the experimental ones shown in Tab. 2.4. If non-negligible defect concentration is presented L_+ will be smaller.

material	[a] α^{-1} [μm]	[b] l_+ [nm]	[c] D_+ [cm^{2}s^{-1}]	[d] L_+ [nm]
Cu	29.8	4.9	1.6	133-139
			1.7±0.5 (DB+Ps) [21]	140±20 [21]
			1.1±0.2 (Ps) [22]	110-114
Fe	34.0	11.9	3.8	200-206
			> 1 (PD) [23]	> 100
Al	99.0	4.4	1.4	146-154
			1.7±0.2 (DB+Ps) [21]	170±10 [21]
Ni	30.0	6.9	2.2	145-153
V	43.8	6.4	1.4	127-133
Cr	37.2	5.5	1.8	135-147

time-independent form which is close to Maxwell-Boltzmann distribution [3]. Average value of the square of the positron thermal velocity is

$$\langle v^2 \rangle = \frac{3k\,T}{m^*}, \tag{2.17}$$

where T is temperature of the medium. *Effective positron mass m^** consists of contribution from positron band structure and positron-electron correlation [27]. Typically in condensed matter $m^* \simeq 1.5\,m$ [2]. Furthermore root of the mean squared positron velocity v_+ is introduced as

$$v_+ \equiv \sqrt{\langle v^2 \rangle}. \tag{2.18}$$

Using of equation (2.17) and estimation of the positron effective mass quoted above yields

$$v_+ \,[\text{nm/ps}] \simeq 5.5\,\sqrt{T}. \tag{2.19}$$

In a classical picture the movement of the thermalized positron is a nearly isotropic random walk [19]. *The mean free path* of thermalized positron, i.e. mean distance between two scattering events, is

$$l_+ = v_+ \tau_{Ph}, \tag{2.20}$$

where τ_{Ph} denotes relaxation time for positron scattering off phonons. In metals τ_{Ph} is of order of ~ 10 fs [28]. Thus the positron mean free path in metals appears to be a few nanometer. Mean free paths calculated using equation (2.20) for the metals related to this work are shown in Tab. 2.3.

The evolution of the positron spatial distribution $f(\mathbf{r}, t)$ is conventionally described by *the diffusion-annihilation equation* [3]

$$\frac{\partial f(\mathbf{r}, t)}{\partial t} = D_+ \nabla^2 f(\mathbf{r}, t) - [\lambda_B + K(\mathbf{r})] f(\mathbf{r}, t) - \nabla[\mathbf{v}_d(\mathbf{r}) f(\mathbf{r}, t)] + f_i(\mathbf{r}, t), \qquad (2.21)$$

where D_+ is *the positron diffusion coefficient* and $\mathbf{v}_d$ is the positron drift velocity due to external fields. The annihilation rate of free (delocalized) positron is denoted by λ_B. Trapping rate at defects $K(\mathbf{r})$ is in general case spatial dependent. The source term is denoted by $f_i(\mathbf{r}, t)$. The diffusion equation is often solved at time-independent steady-state limit which reads as

$$D_+ \nabla^2 f(\mathbf{r}) - [\lambda_B + K(\mathbf{r})] f(\mathbf{r}) - \nabla[\mathbf{v}_d(\mathbf{r}) f(\mathbf{r})] + f_i(\mathbf{r}) = 0. \qquad (2.22)$$

The semiclassical random walk theory gives for the positron diffusion coefficient expression

$$D_+ = \frac{1}{3} v_+ l_+ = \frac{1}{3} v_+^2 \tau_{Ph}. \qquad (2.23)$$

In solids D_+ reaches the values in the range $0.1 - 3$ cm^{2}s^{-1} at room temperature. The diffusion constant may be equivalently expressed by Einstein relation

$$D_+ = \frac{kT}{m^*} \tau_{Ph}. \qquad (2.24)$$

The relaxation time τ_{Ph} for positron scattering off phonons can be calculated using *the deformation potential approximation* [29]

$$\tau_{Ph} = \sqrt{\frac{8\pi}{9}} \frac{\hbar \, s}{(m^* kT)^{3/2} \gamma^2}, \qquad (2.25)$$

where s is the sound velocity in the medium and γ the positron-phonon coupling constant. In the standard deformation potential approximation [29]

$$\gamma^2 = \frac{E_d^2}{2ds}, \qquad (2.26)$$

where d is density of the material and E_d *the deformation potential constant* which is defined as

$$E_d = V \frac{\partial E_+}{\partial V}. \qquad (2.27)$$

The symbol E_+ denotes the total energy of the crystal with the positron in its lowest state (Bloch state at $\mathbf{k} = 0$), and V is the crystal volume. In metals E_d is typically of the order of $-\frac{2}{3} E_F$, where E_F is the Fermi energy [30]. Positron diffusion constants calculated using equation (2.24) are listed in Tab. 2.3. Some experimental values of D_+ found in literature are also included for comparison. We can see that there is relatively good agreement with the experimental values. Positron scattering off phonons leads to temperature dependence of the diffusion coefficient [31]

$$D_+ \sim \frac{1}{\sqrt{T}}. \qquad (2.28)$$

The mean diffusion length L_+ of positron is defined as the mean distance from the point of thermalization which the positron reaches by diffusion movement. This quantity is related to the diffusion coefficient by the relation [3]

$$L_+ = \sqrt{D_+ \tau_f}, \qquad (2.29)$$

where τ_f is the effective lifetime of a free (delocalized) positron

$$\tau_f = \lambda_B + K(\mathbf{r}). \qquad (2.30)$$

The values of the diffusion length for some metals are listed in Tab. 2.3. Clearly L_+ determines the region in the medium which is probed by single positron during its lifetime.

The wavelength of thermalized positron

$$\lambda_+[\text{nm}] = \frac{2\pi\hbar}{m^* v_+} \simeq 5.2 \sqrt{\frac{293 \, [\text{K}]}{T \, [\text{K}]}} \tag{2.31}$$

is significantly greater than the lattice constant ($a \approx 0.1 - 0.5$ nm) in solids. Thermalized positrons in condensed matter therefore behave as waves and we speak about free or delocalized positrons. Note that wavelength of proton is more than three orders of magnitude shorter. It means that behavior of thermalized hydrogen atom and all other atoms is close to heavy classical particles. Hence positron scans in the material volume approximately $\lambda_+^2 L_+$, i.e. region contains about 10^7 atoms. From Tab. 2.3, it is clear that in metals

$$\frac{1}{\alpha} \gg L_+ > l_+ > \lambda_+. \tag{2.32}$$

It means that positron flies the largest distance (in average a hundreds of μm) in a metal during its thermalization. It ensures that PAS provides non-local information about microstructure of studied material. Thermalized positron in defect-free material scans distance of a hundreds of nm, its mean free path is a few nm and wavelength a few tenths of nm.

2.6   Positron states in solids

Ab-initio determination of positron states in solids is possible on the basis of generalization of *the density-functional theory* [32, 33, 34]. In the two-component density-functional theory the ground state energy of a system of electrons and positrons in an external potential V_{ext} is written as a function of the electron (n_-) and positron (n_+) densities

$$\begin{aligned} E[n_-, n_+] &= F[n_-] + F[n_+] \\ &+ \int [n_-(\mathbf{r}) - n_+(\mathbf{r})] \, V_{ext}(\mathbf{r}) \, d\mathbf{r} \\ &- \int \int \frac{n_-(\mathbf{r}) n_+(\mathbf{r}')}{|\mathbf{r} - \mathbf{r}'|} \, d\mathbf{r} d\mathbf{r}' + E_c^{e-p}[n_-, n_+], \end{aligned} \tag{2.33}$$

where $F[n]$ denotes the following one-component functional for electrons or positrons

$$F[n] = T[n] + \frac{1}{2} \int \int \frac{n(\mathbf{r}) n(\mathbf{r}')}{|\mathbf{r} - \mathbf{r}'|} \, d\mathbf{r} d\mathbf{r}' + E_{xc}[n]. \tag{2.34}$$

$T[n]$ is the kinetic energy of non-interacting electrons or positrons and $E_{xc}[n]$ is *the exchange-correlation energy* between indistinguishable particles. $E_c^{e-p}[n_-, n_+]$ in equation (2.33) is the *electron-positron correlation-energy* functional. The ground state electron and positron densities minimizing $E[n_-, n_+]$ can be calculated by a generalized Kohn-Sham method [35], which requires solving of the following set of one-particle Schrödinger equations for electrons and positrons

$$-\frac{1}{2} \nabla^2 \psi_i(\mathbf{r}) + \left[\frac{\delta E_{xc}[n_-]}{\delta n_-(\mathbf{r})} - \Phi(\mathbf{r}) + \frac{\delta E_c^{e-p}[n_-, n_+]}{\delta n_-(\mathbf{r})} \right] \psi_i(\mathbf{r}) = \epsilon_i \psi_i(\mathbf{r}), \tag{2.35}$$

$$-\frac{1}{2} \nabla^2 \psi_i^+(\mathbf{r}) + \left[\frac{\delta E_{xc}[n_+]}{\delta n_+(\mathbf{r})} + \Phi(\mathbf{r}) + \frac{\delta E_c^{e-p}[n_-, n_+]}{\delta n_+(\mathbf{r})} \right] \psi_i^+(\mathbf{r}) = \epsilon_i^+ \psi_i^+(\mathbf{r}), \tag{2.36}$$

where

$$\Phi(\mathbf{r}) = \int \frac{-n_-(\mathbf{r}') + n_+(\mathbf{r}') + n_0(\mathbf{r}')}{|\mathbf{r} - \mathbf{r}'|} \, d\mathbf{r}' \tag{2.37}$$

is the total Coulomb potential and $n_0(\mathbf{r})$ denotes the (positive) charge density providing the external potential V_{ext}. The electron and positron densities are calculated by summing over the occupied states

$$n_-(\mathbf{r}) = \sum_{\epsilon_i \leq E_F} |\psi_i(\mathbf{r})|^2, \qquad n_+(\mathbf{r}) = \sum_i^{N_+} |\psi_i^+(\mathbf{r})|^2, \tag{2.38}$$

where E_F is the Fermi energy and N_+ number of positrons. Usually there are not more than one positron at a given time in the sample, i.e. the number of positrons $N_+ = 1$ and

$$n_+(\mathbf{r}) = |\psi_0^+(\mathbf{r})|^2, \tag{2.39}$$

In order to solve the equations (2.35, 2.36) it is necessary to know the exchange-correlation energy $E_{xc}[n]$ and the electron-positron correlation energy functional $E_c^{e-p}[n_-, n_+]$. *The local density approximation* (LDA) is often used. The exchange-correlation energy is in LDA approximated as

$$E_{xc}[n] = \int n(\mathbf{r})\epsilon_{xc}\left(n(\mathbf{r})\right)\,d\mathbf{r}, \tag{2.40}$$

where $\epsilon_{xc}(n)$ is the exchange-correlation energy per particle in homogeneous electron gas and it is known from Monte-Carlo simulation [36, 37, 38]. The functional derivative of $E_{xc}[n]$ is called the exchange-correlation potential

$$\mu_{xc}(n) = \frac{\delta E_{xc}[n]}{\delta n(\mathbf{r})} = \frac{\partial \left[n\epsilon_{xc}(n)\right]}{\partial n}. \tag{2.41}$$

The interpolation formula giving the electron-positron correlation energy functional was found by Boroński and Nieminen [34].

The positron annihilation rate λ is proportional to the overlap of positron and electron densities. In the LDA approximation [3]

$$\lambda = \pi r_0^2 c \int n_-(\mathbf{r})n_+(\mathbf{r})g(0; n_-, n_+)\,d\mathbf{r}, \tag{2.42}$$

where $g(0; n_-, n_+)$ is the electron-positron pair correlation function evaluated at the positron in a homogeneous two-component plasma with positron density n_+ and electron density n_-. A practical interpolation formula for $g(0; n_-, n_+)$ was presented in [34]. Furthermore r_0 is the classical electron radius and c is the speed of light.

2.6.1 Delocalized positron

In the case of delocalized positron in a perfect lattice n_+ is vanishingly small at every point of the (infinite) lattice. Kohn-Sham equations (2.35, 2.36) obtain substantially simpler form

$$-\frac{1}{2}\nabla^2\psi_i(\mathbf{r}) + [\mu_{xc}\left(n_-(\mathbf{r})\right) - \Phi(\mathbf{r})]\psi_i(\mathbf{r}) = \epsilon_i\psi_i(\mathbf{r}), \tag{2.43}$$

$$-\frac{1}{2}\nabla^2\psi_i^+(\mathbf{r}) + [\Phi(\mathbf{r}) + V_{corr}\left(n_-(\mathbf{r})\right)]\psi_i^+(\mathbf{r}) = \epsilon_i\psi_i^+(\mathbf{r}). \tag{2.44}$$

The correlation potential V_{corr} is the zero-positron-density limit of the electron-positron correlation potential $\frac{\delta E_c^{e-p}[n_-, n_+]}{\delta n_-(\mathbf{r})}$ and it is equal to the correlation energy for a delocalized positron in a homogeneous electron gas. A practical form of V_{corr} is the parametrization by Boroński and Nieminen [34].

The annihilation rate of delocalized positron may be calculated from positron and electron densities according to equation (2.42)

$$\lambda = \pi r_0^2 c \int n_-(\mathbf{r})n_+(\mathbf{r})\gamma(n_-)\,d\mathbf{r}, \tag{2.45}$$

Table 2.4   The positron bulk lifetimes τ_B, the Wigner-Seitz radius R_S and the Fermi energy E_F.

material	E_F [eV]	R_s [18] $[a_0]$	τ_B [ps] LDA [39]	GGA [40]	experimental
Cu	14.96	1.83	106	118	110 [41] 112 [42] 120 [40]
Fe	11.69	2.07	101	108	106 [41] 110 [43] 112 [40]
Al	11.15	2.12	166	153	163 [41] 170 [40]
Ni	15.46	1.80	96	107	95 [41] 107 [40]
Cr	20.85	1.55	101		120 [41]
V	17.75	1.68	116	119	130 [41]

where

$$\gamma(n_-) = \lim_{n_+ \to 0} g(0; n_-, n_+). \tag{2.46}$$

Thus $\gamma(n_-)$ is zero-positron-density limit of the pair-correlation function and it is called the enhancement factor of the electron density at the positron. The interpolation formula of the enhancement factor was given also by Boroński and Nieminen [34]. Note that enhancement of the annihilation rate due to the enhancement factor is substantial [34].

Hence the electron density in the infinite lattice is not disturbed due to positron, besides the short-range pile-up (enhancement) at the positron site. Therefore the average electron density can be calculated first without any influences due to the positron. The positron state is calculated by taking the electron pile-up into account as lowering of the energy (correlation energy), which in a given point depends on the electron density at that point only (LDA). Finally the positron annihilation rate is calculated using equation (2.45).

The inverse value of the delocalized positron annihilation rate λ_B is called positron bulk lifetime τ_B

$$\tau_B = \frac{1}{\lambda_B}. \tag{2.47}$$

Dependence of the positron bulk lifetimes calculated using LDA approximation [39] on the Wigner-Seitz radius R_S (radius of hypothetic sphere contained just one conduction e^- expressed in units of the Bohr radius a_0) is shown in Fig. 2.7. The experimental values taken from [41] are also included in this figure for comparison. The interval $1.4 < R_s < 2.4$, which is most interesting for us, is zoomed in Fig. 2.8. The positron bulk lifetimes for metals of interest in this work are collected in the Tab. 2.4. The theoretical values calculated in the frame of LDA were taken from [39] while the experimental ones were taken mostly from [41]. The Fermi energy and the Wigner-Seitz radius R_s for the metals related to this work are also listed in Tab. 2.4.

The positron bulk lifetimes calculated using LDA appears to be systematically lower that the experimental ones. It is caused by the fact that LDA overestimates the electron-positron correlation energy and the enhancement factor [3]. Therefore the gradient correction for the correlation energy was introduced in so called *generalized gradient approximation* (GGA) [40].
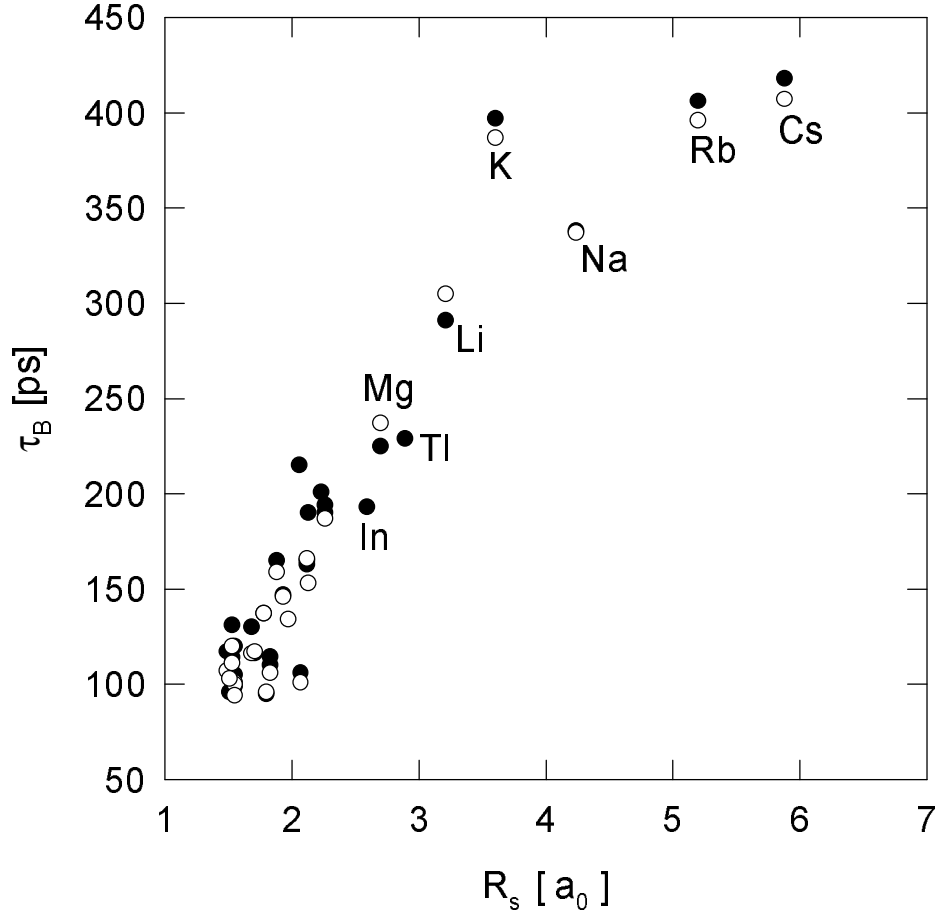
Figure 2.7 Dependence of the positron bulk lifetime on the Wigner-Seitz radius. Theoretical values (◦) were calculated using LDA in [39], experimental values (•) were taken from [41].

The gradient correction should reduce the electron density near the positron and thereby decrease the enhancement factor and increase the positron lifetime. In the GGA the correlation potential and the enhancement factor become also function of the gradient of the electron density, i.e. $V_{corr}(n_-, \nabla n_-)$, $\gamma(n_-, \nabla n_-)$. The positron bulk lifetimes calculated by GGA in [40] are shown in Tab. 2.4.

2.7 Positron trapping into defects

The potential sensed by the positron at open-volume defects (e.g. monovacancies, vacancy clusters etc.) is lowered due to reduction in the repulsion by the positive ion cores. As a result a localized positron state at the defect with a lower energy eigenvalue than a state delocalized over the lattice can exist. Transition from the delocalized state into the localized one is called *positron trapping*. The energy difference between localized and delocalized state of the positron (*positron binding energy* for the defect) is transferred to the host solid.

Transport of positron from the point of thermalization to the vicinity of a trap and transition from delocalized to trapped state is necessary for positron trapping in defect. Clearly two limit cases may occur
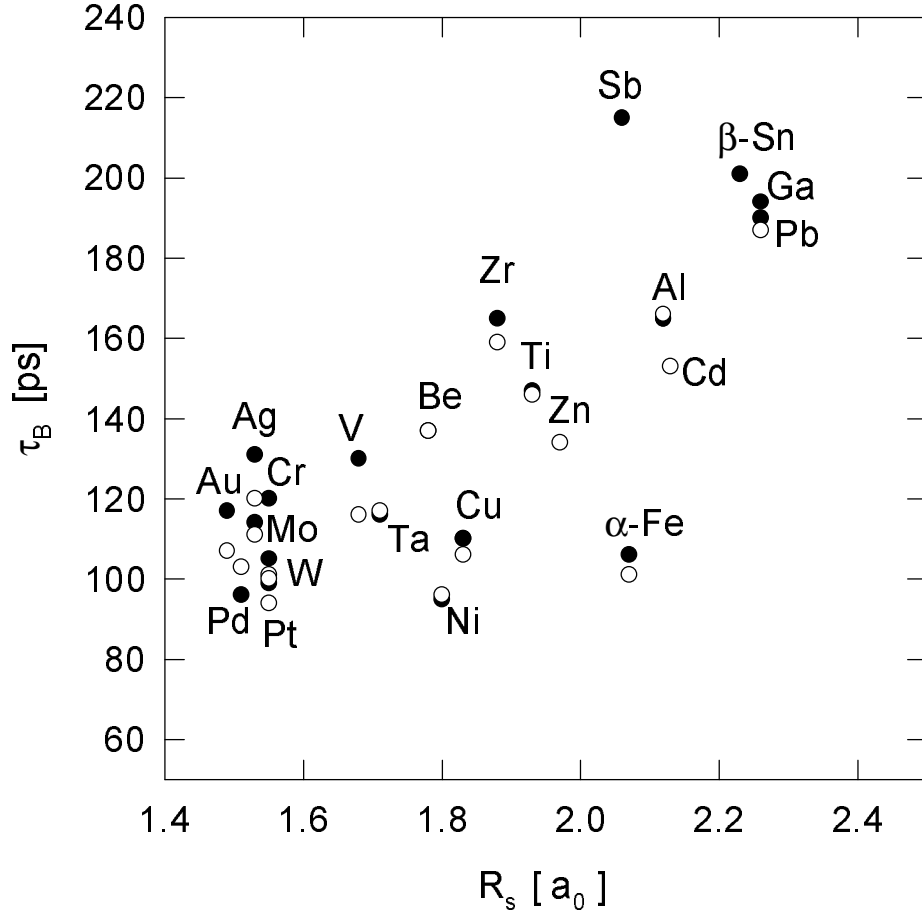
Figure 2.8 Dependence of the positron bulk lifetime on the Wigner-Seitz radius. zoomed for $1.4 < R_s < 2.4$. Theoretical values (∘) were calculated using LDA in [39], experimental values (•) were taken from [41].

1. *diffusion-limited regime,* when trapping is essentially controlled by transport factors. The transport factors (diffusion of positron to the neighbourhood of defect) are likely to be dominant when the transition rate from a free to a trapped state for a positron already present in the vicinity of a trap is so high that the stochastic positron density is depleted around the defect. Typical example is positron trapping at grain boundaries [44] or in larger precipitates [45].

2. *transition-limited regime* or *propagation regime* when positron motion may be described as a Bloch wave propagation. Positron trapping in monovacancies is an example of transition-limited regime [46].

In practical situation any intermediate case is possible.

In the case of transition-limited regime the link between positron states in the specimen and experimental positron lifetime spectrum is provided by *the simple trapping model* (STM) [47]. Let $m(t)$ denotes the probability that positron will be alive in the specimen at time t. In the case of ideal crystal, i.e. if no defect is presented in the specimen, positrons will be delocalized in the material. The time when positron thermalization is accomplished is chosen as $t = 0$. Thus

$m(t = 0) = 1$. The probability $m(t)$ decreases exponentially with time

$$m(t) = e^{-\lambda_B t},\tag{2.48}$$

where λ_B is the annihilation rate of delocalized positron.

If the specimen contains N types of defects which are capable to capture a positron then

$$m(t) = \sum_{i=0}^{N} m_i(t),\tag{2.49}$$

where $m_0(t)$ and $m_i(t)$ $(i \geq 1)$ denotes the probability that positron is alive as free or trapped at $i-$th kind of defect, respectively, at time t. The kinetic equations for the trapping process may be written as

$$\frac{dm_i(t)}{dt} = -\left(\lambda_i + \sum_{j \neq i}^{N} K_{ij}\right) m_i(t) + \sum_{j \neq i}^{N} K_{ji} m_j(t).\tag{2.50}$$

Above λ_i $(i \geq 1)$ denotes the annihilation rate of positron trapped by $i-$th type of defect. The annihilation rate of delocalized positron

$$\lambda_B \equiv \lambda_0.\tag{2.51}$$

K_{ij} is the positron transition rate from $i-$th state to $j-$th state, where delocalized positron is denoted by $i = 0$ and positron trapped by $k-$th defect by $i = k$. It should by pointed out that restriction only to the transition-limited regime causes that the transition rates have no spatial dependence.

Usually the binding energy of trapped positron to the defect is large enough (a few eV) and *detrapping* (i.e. escape from the trap) is negligible. It means that $K_{ij} = 0$ for all $i \geq 1$, $j \geq 0$. The equations (2.50) may be rewritten as

$$\begin{aligned}
\frac{dm_0(t)}{dt} &= -\left(\lambda_B + \sum_{j \neq 0}^{N} K_{0j}\right) m_0(t) \\
\frac{dm_j(t)}{dt} &= -\lambda_j m_j(t) + K_{0j} m_0(t) \qquad j = 1, 2, \ldots, N.
\end{aligned}\tag{2.52}$$

Furthermore we assume that there is no trapping of non-thermalized positrons, i.e.

$$m_0(t = 0) = 1, \qquad m_j(t = 0) = 0, \qquad j = 1, 2, \ldots, N.\tag{2.53}$$

The solution of equations (2.52) with boundary conditions (2.53) gives for the probability $m(t)$

$$m(t) = \left[1 - \sum_{j \neq 0}^{N} \frac{K_{0j}}{\lambda_B - \lambda_j + \varepsilon}\right] e^{-\lambda_f t} + \sum_{j \neq 0}^{N} \frac{K_{0j}}{\lambda_B - \lambda_j + \varepsilon} e^{-\lambda_j t},\tag{2.54}$$

where $\varepsilon = \sum_{j \neq 0}^{N} K_{0j}$ and $\lambda_f = \lambda_B + \varepsilon$ is the effective annihilation rate of free positrons.

The measured quantity in positron lifetime measurements is the time when positron annihilates. $t = 0$ corresponds to positron emission. It means that the shape of positron lifetime spectrum $\mathcal{S}$ is

$$\mathcal{S}(t) = -\frac{dm(t)}{dt}.\tag{2.55}$$

The real positron lifetime spectrum is convolution of $\mathcal{S}$ with resolution function of the spectrometer. Moreover background arises from random coincidences and the contribution of the positrons which annihilated in the source is added. From equations (2.54, 2.55) it is clear that the shape of positron lifetime spectrum predicted by STM is sum of exponential components

$$\mathcal{S}(t) = \lambda_f I_0 e^{-\lambda_f t} + \sum_{j=1}^{N} \lambda_j I_j e^{-\lambda_j t},\tag{2.56}$$

where the relative intensities of the defect components are

$$I_j = \frac{K_{0j}}{\lambda_B - \lambda_j + \varepsilon}, \qquad j = 1, 2, \ldots, N. \tag{2.57}$$

The first component $I_0 = 1 - \sum_{j=1}^{N} I_j$ belongs to free (delocalized) positrons.

The useful test of self-consistency of STM application is relation

$$\sum_{j=0}^{N} \lambda_j I_j = \lambda_B, \tag{2.58}$$

where λ_i, I_i are measured in material with defects, while λ_B is determined experimentally or theoretically for defect-free material. By self-consistency we mean the justification that the assumptions which lead to equations (2.52, 2.53), i.e. transition-limited regime, no prethermal trapping and no detrapping, are fulfilled. Non-equality in relation (2.58) may also suggest that there is more than N types of defects in the specimen.

The trapping rates K_{0j} are directly connected with the concentration c_j of $j-$th type of defect.

$$K_{0j} = \nu_j c_j. \tag{2.59}$$

The quantity ν_j is called *specific trapping rate* (or *trapping coefficient*) and it expresses the positron trapping rate for unit concentration of the $j-$th type of defect. The specific trapping rate depends on the electronic and atomic structure of the defect and therefore it is characteristic quantity for a given type of defect. In general the specific trapping rate may, however, depend also on temperature of the material because it determines the energy distribution of the thermalized positrons. Thus positron lifetime measurement is capable of giving the information about local electronic structure of the defects. Moreover identification of the defects presented in the specimen and calculation of the concentrations of different types of the defects is possible as well.

Positron diffusion to the defects does not limit the trapping rate in the transition-limited regime. Therefore the specific positron trapping rate is directly the transition rate between the delocalized and localized state and it is given by the Fermi golden rule formula [48].

In the case of diffusion-limited regime one have to solve the positron diffusion equation (2.21). The obtained shape of positron lifetime spectrum is, however, an infinite sum of exponential components even in the case of single type of defect presented in the material [49]. It was shown by Brandt and Paulin [49] that for single kind of traps the exact solution may be approximated by formally the same equations as the CTM ones (2.52, 2.53). The trapping rate K then does not have the form (2.59) but depends also on dimension and shape of a defect and on the positron diffusion constant D_+. The trapping rates for various shapes of traps (precipitates), cylindrical pores (dislocations) and spherical voids taken from [49] are shown in Tab. 2.5. It has to be pointed out that positron trapping in precipitates is possible only when the positron ground state energy in a precipitate is lower than that in matrix (see section 2.8.5). Nevertheless it was shown by Dupasquier [44] that the simple approximation used in [49] systematically underestimates intensity of the defect component.

In the intermediate case, when both the transition of positron to vicinity of a trap and transition from delocalized to trapped state influence the trapping rate significantly, one has to solve the diffusion equation (2.21).

2.8 Positron traps in metals

2.8.1 Monovacancies

The lifetimes of positrons trapped in monovacancies determined both experimentally and theoretically lie in interval $150 - 300$ ps for metals. The Positron lifetimes in monovacancies calculated by

Table 2.5 Trapping rates for positron trapping in various defects. The formulas were derived in [49] for diffusion-limited regime.

defect	trapping rate K
precipitates:	
foil(thickness R)	$\frac{\pi^2 D_+}{R^2}$
fiber (radius R)	$5.78\,\frac{D_+}{R^2}$
sphere (radius R)	$\frac{\pi^2 D_+}{R^2}$
rectangular slab (dimensions $X \times Y \times Z$)	$\pi^2 D_+(X^{-2} + Y^{-2} + Z^{-2})$
cylindrical pores (dislocations) (radius r, $\varrho = \frac{1}{\pi r^2}$ – dislocation density)	$\frac{4\pi \varrho D_+}{\ln(1/(\pi \varrho r^2))}$
spherical voids (radius r, $c = \frac{3}{4}\frac{1}{\pi r^3}$ – volume concentration of voids)	$4\pi r c D_+$

LDA [50] and the experimental ones are shown in Tab. 2.6 for the metals relevant to the present work. The positron binding energy E_B for monovacancy is typically a few eV in transition metals and it is dissipated by the electron-hole excitations [48]. Thus detrapping from monovacancies in metals does not occur. The computed E_B values for the metals of interest found in literature are collected in Tab. 2.6.

It was shown by Hodges [46] that positron trapping in vacancies is transition limited process and the specific trapping rate ν_{1V} is independent of temperature [28, 2]. The same result was obtained also experimentally [51, 52, 53]. Both the calculations based on the Fermi golden rule [48, 28] and the experiments [2, 51, 43] have revealed that $\nu_{1V} = (10^{14}-10^{15})$ s^{-1}at. in metals. For experimental determination of ν_{1V} it is necessary to measure independently absolute concentration of monovacancies in the specimen. The experiments were performed at elevated temperatures where the equilibrium concentration of monovacancies is high enough to make the contribution of trapped positrons in PL spectrum significant [54, 55]. Kluin et al. [51] have correlated positron lifetime, dilatometry and lattice parameter experiments. Another way is to perform electron irradiation at low temperature [43]. The irradiation-induced Frenkel pairs are frozen in the lattice and their concentration may be obtained by measuring the residual resistivity and dividing it by resistivity of a Frenkel pair. Soma experimental and theoretical values of ν_{1V} for the metals of interest are listed in Tab. 2.6.

The lowest vacancy concentration detected by PL spectroscopy may be estimated using 2-state STM, i.e. equations $(2.52 - 2.59)$, where $N = 1$. From eq. (2.57) one can write

$$K_{1v} \equiv K_{01} = \frac{I_2}{I_1}(\lambda_B - \lambda_2). \tag{2.60}$$

If one assume $I_2 = 5\%$ as a lower limit of relative intensity of the defect component, which can be resolved in PL spectrum, then eq. (2.60) gives $K_{1v}^{min} \approx 10^8$. Thus using eq. (2.59) one obtain the minimum detectable vacancy concentration $c_{1v}^{min} \approx 10^7$ at.$^{-1}$. On the other hand $I_1 = 5\%$ represents minimum relative intensity of the free positron component, which can be

Table 2.6 Properties of positrons trapped in metal vacancies. The lifetimes of positrons trapped in monovacancies $\tau_{1V}^{theor.}$ and the binding energies E_B were calculated using LDA approach in [50]. Some results obtained by another approximation are added for comparison. $\tau_{1V}^{exp.}$ denotes the experimental lifetime of positrons trapped in vacancies. The specific trapping rates ν_{1V} were calculated using the Fermi golden rule or determined experimentally using electron irradiation experiment (e$^-$ irr.) or dilatometry and lattice parameter measurement ($\Delta l/l - \Delta a/a$).

material	$\tau_{1V}^{theor.}$ (LDA) [50] [ps]	$\tau_{1V}^{exp.}$ [ps]	E_B [50] [eV]	ν_{1V} [10^{14} s^{-1}at.]	
Cu	188 185 [57]	180 [56] 179 [41]	1.1	1.2±0.2	($\Delta l/l - \Delta a/a$)[51]
Fe	190 176 [59]	170 [58] 175 [41]	3.0	11±2	(e$^-$ irr.) [43]
Al	253 252 [57]	245 [60] 251 [41]	2.3 1.8 [61] 3.36 [62] 1.56 [63]	2.5	(theory) [28]
Ni	184	180 [64]	2.6		
Cr	201	180 [65]	2.6		
V	181	191 [41]	2.0		

resolved in PL spectrum. Using the same procedure as above it leads to maximum detectable vacancy concentration $c_{1v}^{max} \approx 10^{-3}$ at.$^{-1}$. It means that if $c_{1v} > c_{1v}^{max}$ almost all positrons will be trapped at monovacancies (saturated trapping) and determination of vacancy concentration will be impossible.

2.8.2 Vacancy clusters

The lifetimes of positrons trapped in small vacancy clusters were calculated in [50] using LDA approach. As the lattice relaxation around the cluster has relatively small influence on positron annihilation parameters, it was not included in the calculations. The results show that the lifetime of positron trapped by divacancy does not differ a lot from that for monovacancy (increase about 10 ps for Fe and 20 ps for Al). The lifetime increases rapidly when the cluster grows into two-dimensional trivacancy and further to three-dimensional tetravacancy [50]. For large clusters the lifetime saturates around 500 ps. Dependence of positron lifetime in vacancy clusters on free volume of the cluster expressed as number of vacancies which forms the cluster is shown in Fig. 2.9. The lifetimes were taken from [50].

The specific trapping rate ν_{NV} for small ($N < 10$) spherical clusters of N vacancies may be approximated as

$$\nu_{NV} \approx N\nu_{1V}. \tag{2.61}$$

The trapping rate to larger vacancy clusters the size of which is comparable to λ_+ becomes limited also by positron transport to vicinity of the defect [46]. Thus the trapping process is shifted from the transition-limited regime into the intermediate regime. For large voids the trapping may be limited mainly by positron diffusion to the defect. As the result of it, the positron specific trapping rate ν_{NV} becomes dependent on temperature.
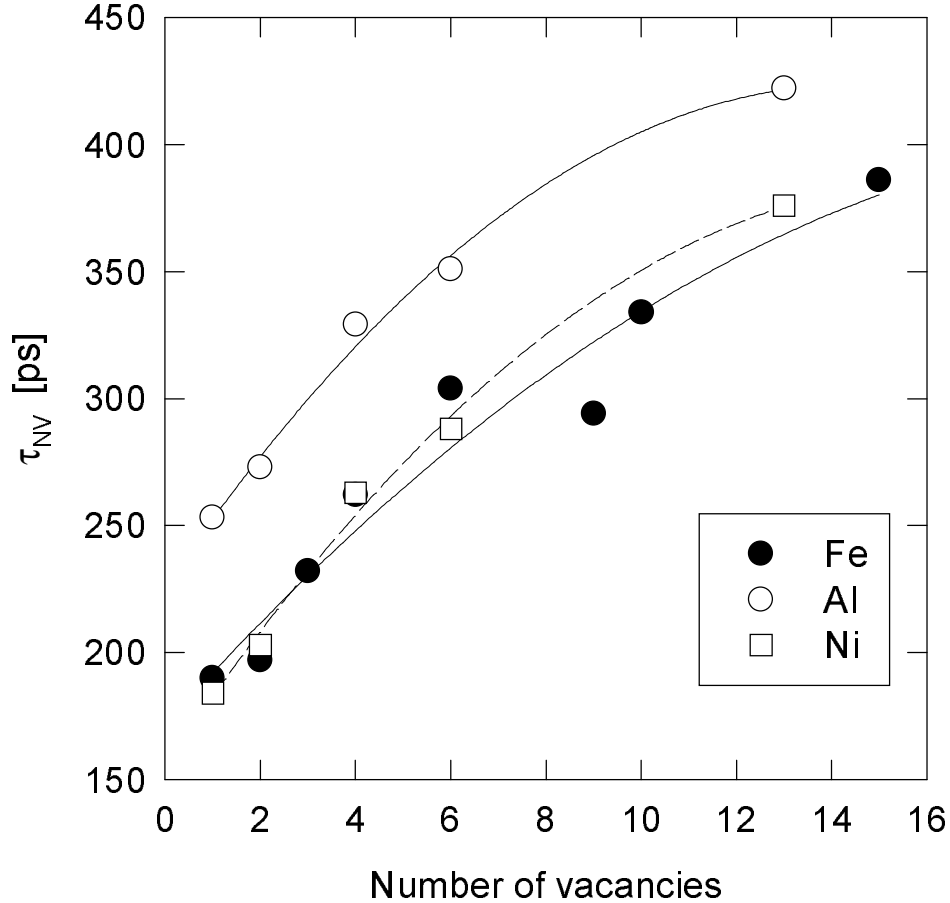
Figure 2.9 Dependence of the lifetime of positron trapped in vacancy cluster consists of N vacancies. The τ_{NV} values were calculated in LDA approximation in [50]. The solid lines are only to guide the eye. The deviations from the smooth curve reflect the discrete structures of the clusters.

2.8.3 Dislocations

Theoretical calculations have revealed that dislocation line is only shallow trap for positrons [66, 67, 57] (binding energy < 0.1 eV). On the other hand the lifetimes of trapped positrons observed in plastically deformed metals [68, 69, 70, 71, 72] are only slightly lower than the lifetimes of positrons trapped in vacancies. Smedskjaer [67] suggested that the pure dislocation line is a weak positron trap, and explained the long lifetimes seen in experiments by point-like defects (vacancies, jogs) associated with the dislocation. For example the binding energy of 0.92 eV for vacancy to the edge-dislocation line was calculated in [73] for Fe. Once a positron arrives at the core of a dislocation, it diffuses very quickly (pipe diffusion) until it finds a vacancy attached to the dislocation or a jog of the dislocation, it is trapped and annihilates there [74]. This explanation was supported also by further calculations [57, 73]. Calculated lifetimes of positrons trapped in dislocations and corresponding binding energies are listed in Tab. 2.7. The trapping rate for the final states in dislocations is limited by number of dislocations and it is possible to determine the dislocation density in the specimen from positron lifetime measurements.

The specific trapping rate ν_D for dislocations were obtained by correlation of positron life-

Table 2.7 Calculated lifetimes τ and binding energies E_B of positrons trapped in core region of dislocation line and in defects associated with dislocation. The values were taken from [73, 57].

Annihilation site	τ [ps]	E_B [eV]
Fe [73]		
edge dislocation line	117	
jog on the edge dislocation line	117	
vacancy on the edge dislocation line	140	
Cu [57]		
[1$\bar{1}$2] dislocation line	114	0.06
vacancy on the [1$\bar{1}$2] dislocation line	166	0.8
vacancy in the stacking-fault region	177	1.2
Al [57]		
[1$\bar{1}$2] dislocation line	174	0.1
vacancy on the [1$\bar{1}$2] dislocation line	225	1.0
jog of the [1$\bar{1}$2] dislocation line	224	1.3
(111) dislocation loop	191	0.4

time measurement and transmission electron microscopy (TEM) or other techniques capable of determining dislocation density (e.g. X-ray diffraction profile) [70, 75]. In metals ν_D lies in the range $10^{-5} - 10^{-4}$ m^{2}s^{-1}. Thermally activated detrapping of positrons trapped in dislocation core (initial shallow trap) may occur at elevated temperatures which makes ν_D temperature dependent [67]. The experimental lifetimes of positrons trapped in dislocations and the specific positron trapping rates for dislocations at room temperature are collected in Tab. 2.8. The different lifetimes for screw and edge dislocations in Fe single-crystal were reported in [70], see Tab 2.8. According to this work edge dislocations exhibit larger specific trapping rate ν_D and lifetime than the edge ones. Similarly as for vacancies in the previous section, it can be shown that the minimum dislocation density detectable by PL spectroscopy is $\varrho_D \sim 10^{12}$ m^{-2}. On the other hand, if $\varrho_D \sim 10^{16}$ m^{-2} almost all positrons are trapped at dislocations (saturated trapping) and only the contribution of the trapped positrons is resolved in PL spectrum.

2.8.4 Grain boundaries

Positron may be trapped by grain boundary (GB) in metals. Nevertheless trapping in GB's is likely only when mean linear dimension of grains do not exceed a few μm. It means the grain size is comparable to (or smaller than) the positron diffusion length L_+ and some fraction of positrons have a chance to reach GB by diffusion motion. Positron trapping in GB's plays therefore significant role in nanocrystalline materials (see section 5) It is clear that transport of a positron to GB limits substantially the positron trapping rate in GB's. Therefore usually the positron-diffusion equation (2.21) is used in the interpretation of positron lifetime spectra of positrons trapped in GB's (e.g. [44]).

Table 2.8 Lifetimes τ_D and specific trapping rates ν_D for positrons trapped in dislocations.

material	τ_D [ps]	ν_D $[10^{-4}\ \mathrm{m^2s^{-1}}]$
Cu	179±2 [76]	0.66±0.09 [76]
	155 [77]	
Fe screw disl.	142 [70]	0.51 [70]
Fe edge disl.	165 [70]	0.70 [70]
Fe	150 [73]	
Al	235 [75]	0.45 [75]
	215 [78]	
	228±1 [71]	
	250±30 [79]	
	220±2 [68]	

2.8.5 Precipitates

The relative values of the energy eigenvalue for the ground state of delocalized positron in different materials are different. It makes possible positron trapping in a precipitate with lower level of the positron ground state energy.

Table 2.9 The positron affinities A_+ calculated in [80] and the experimental ones taken from [81]. [a] The experimental values were deduced in [80] from the measured positronium formation potentials (see [80] and the references therein).

material	$A_+^{theor.}$ [80] [eV]	$A_+^{exp.}$ [eV]
Cu	-4.81	-4.4 [81], -4.4[a]
Fe	-3.84	
Al	-4.41	-4.3[a]
Ni	-4.46	-3.8 [81], -4.0[a]
Cr	-2.62	-2.6[a]
V	-3.44	

Common reference energy level, so called *crystal zero* can be uniquely defined for both electrons and positrons in perfect solids. Therefore the energy levels in the calculations are measured relative to this internal quantity. The electron chemical potential μ_- is defined as the distance of the Fermi level from the crystal zero (see Fig. 2.10). Similarly, the distance of the lowest positron energy level from the crystal zero defines the positron chemical potential μ_+ (see Fig. 2.10). The crystal zero is related to the Coulomb potential and it can be defined for example as the average
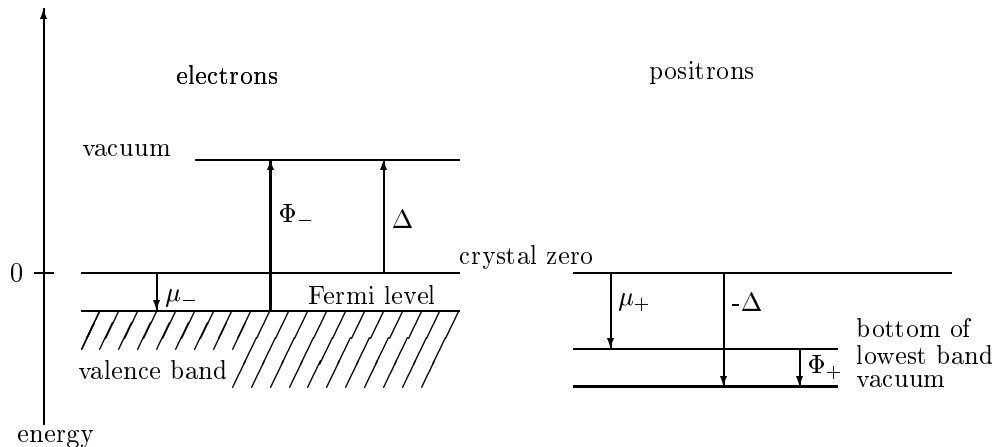
Figure 2.10 Electrons and positron potentials and energy levels near a metal surface. Δ is the dipole potential at the surface, Φ_-, Φ_+ denote the electron and positron work functions, respectively. μ_- and μ_+ are the electron and positron chemical potentials, respectively. Arrows pointing upwards and downwards denote positive and negative quantities, respectively.

electrostatic potential in the infinite lattice, or the average value of the electrostatic potential on the surface of the Wigner-Seitz cell. When the solid is considered to have a surface facing the vacuum, the distance from the electrostatic potential level, which a test charge feels in the vacuum (the vacuum level) to the crystal zero is the surface dipole potential Δ (see Fig. 2.10). An electron and a positron have the same absolute value of Δ but the signs are opposite due to opposite electron and positron charges. The distance between the absolute Fermi energy level and the vacuum level defines *electron work function* Φ_- [3]

$$\Phi_- = \Delta - \mu_-. \tag{2.62}$$

The *positron work function* Φ_+ is the difference between the lowest energy state level and the vacuum level [3]

$$\Phi_+ = -\Delta - \mu_+. \tag{2.63}$$

Both the Φ_-, Φ_+ are measurable quantities and do not depend on the position of the crystal zero.

In the case of two metals A and B in contact the Fermi levels equalize themselves over the interface. As a result an interface dipole with potential difference $\mu_-^A - \mu_-^B$ is formed (see Fig. 2.11). The difference between the lowest positron energies on the different sides of the interface is [3]

$$\Delta E_+^{A,B} = E_+^A - E_+^B = \mu_-^A - \mu_-^B + \mu_+^A - \mu_+^B. \tag{2.64}$$

It is useful to define the following quantity which is called *the positron affinity* A_+

$$A_+ = \mu_- + \mu_+. \tag{2.65}$$

The positron affinity is a bulk property of a given homogeneous material and it is not related to the interface between two materials. The more negative the positron affinity is, the deeper is the positron energy level in the solid. The difference of the lowest positron energies between two materials in contact now can be written as

$$\Delta E_+^{A,B} = A_+^A - A_+^B. \tag{2.66}$$

26

The positron affinities for some metals calculated in [80] are shown in Tab. 2.9. It is possible to obtain the positron affinity also experimentally from the positron and electron work functions

$$A_+ = \mu_- + \mu_+ = -\Phi_- - \Phi_+. \tag{2.67}$$

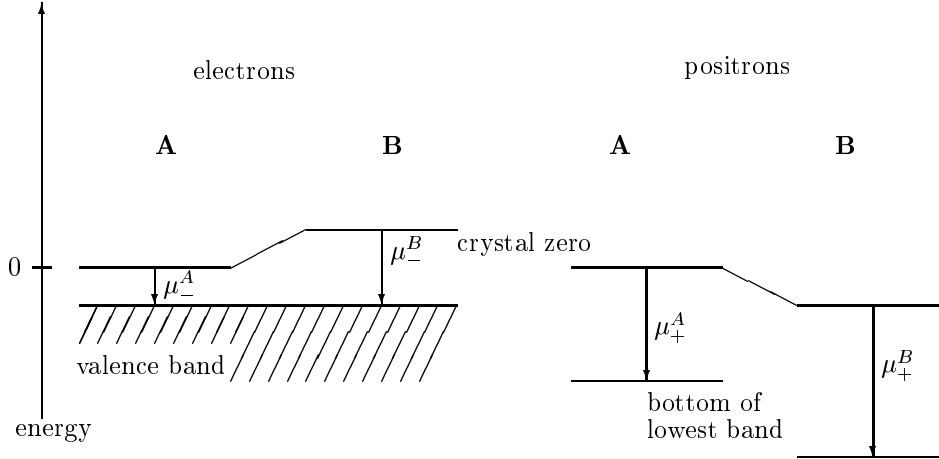The experimental values are included in Tab. 2.9 as well.

Figure 2.11 Electron and positron potentials and energy levels near a junction of two metals A, B. $\mu_-^A, \mu_+^A, \mu_-^B, \mu_+^B$ denote the electron and positron chemical potential for metal A and B, respectively.

Only if the difference between positron affinity to host matrix and to a precipitate is positive, the precipitate attracts the positron and localization or trapping in the precipitate is possible. Despite of this the size of the precipitate is required to be large enough for positron to be trapped. In the case of spherical potential, the minimum radius for a bound state is [2]

$$r_c \ [\text{nm}] = 0.31 \ / \sqrt{\Delta A \ [\text{eV}]}, \tag{2.68}$$

where ΔA is the affinity difference between the matrix and the precipitate.

It should be pointed out that positrons may be trapped also by misfit defects in matrix-precipitate interface (e.g. [45]) or by defects inside a precipitate despite of the affinity to the precipitate.

3 Measurement Techniques of Positron Annihilation Spectroscopy

Various measurement techniques are used in the field of positron annihilation (for description see [58, 2]). The two methods used in this work are described in the following sections.

3.1 Positron Lifetime Measurement

The physical principle of positron lifetime (PL) measurement is elucidated in Fig. 3.1. The actual
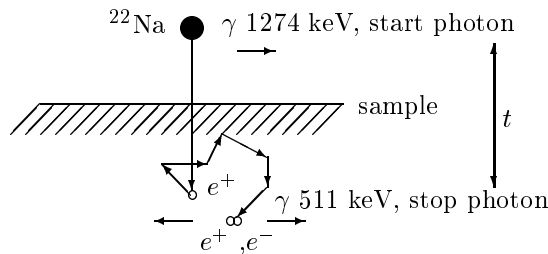

Figure 3.1   Principle of positron lifetime measurement. ^{22}Na β^+- source is considered.

lifetimes of individual positrons in sample are measured, i.e. PL spectrum represents histogram of positron lifetimes in the sample. In order to obtain lifetime of given positron, information about the time when positron emission occurs is necessary. This information (so called start signal) is carried out by photon produced in de-excitation of daughter nucleus created in β^+- decay of positron source. Therefore only β^+- sources with secondary photons emitted simultaneously with positron can be used in PL measurements (see Tab. 2.1). Usually ^{22}Na is used. This β^+- source is also considered in Fig. 3.1. The measured lifetime of given positron is then time delay t between detection of start signal and one of the annihilation photons (stop signal).

Because of constant annihilation rate λ in given positron state, the probability that positron is alive decreases exponentially with time (see section 2.7) therefore PL spectrum is usually a superposition of exponential components. The lifetime τ of positrons in given state is defined as inverse of the corresponding annihilation rate λ of this state, i.e. $\tau \equiv 1/\lambda$.

The PL spectrometer is shown schematically in Fig. 3.2. The start and stop photons are detected by start and stop detector, respectively. The detector consists of fast scintillator (S) coupled to fast photomultiplier (PMT). Usually fast plastic scintillators (e.g. NE111, PilotU) [82, 83, 84] or BaF$_2$ crystals are used [85]. Fast signals from PMTs (rise time a few ps) fed constant-fraction-discriminators (CFD) to produce fast logical time signals. These are led to a time-to-amplitude converter (TAC), the output of which is proportional to the time interval t between start and stop signals. The amplitude of the signal from TAC is then digitized by analog-to-digital converter (ADC) and it is in stored computer. This setup described in Fig. 3.2 is called *fast-fast* (FF) coincidence system. The CFD units can usually work also in differential mode, which provides also coarse energy selection of input pulses in the FF spectrometers. However, some distortions of PL spectrum may be present due to imperfect energy selection of input pulses.
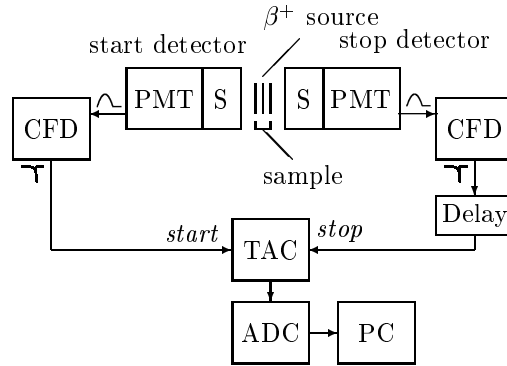
Figure 3.2 Schematic description of the fast-fast PL spectrometer.
S − scintillator, PMT − fast photomultiplier, CFD − constant-fraction-discriminator, TAC − time-to-amplitude converter, ADC − analog-to-digital converter, PC − personal computer.

The distortions are connected especially with undesired detection of photons scattered between detectors (for details see appendix A, section 2.2.) and lead to spurious generally non-exponential structures in PL spectrum. For these reasons *fast-slow* (FS) coincidence system is used when high precision of positron lifetimes and relative intensities of spectral components is required. The FS spectrometer is schematically shown in Fig. 3.3. It consists of fast circuit which is the same as in the FF spectrometer. Contrary to the FF arrangement, slow circuit is added. The slow circuit works with slow signals (pulse width hundreds of ns). The slow signal from PMT is firstly amplified and shaped in spectroscopy amplifier (SA) and subsequently led into single-channel analyzer (SCA) which provide precise energy selection. For ^{22}Na source the energy window of the SCA for the slow start and stop signal is adjusted at energy 1274 keV and 511 keV, respectively. The output of TAC is then gated by coincidence unit (Coinc) in the slow branch. It means that the output pulse from TAC is accepted only if amplitude of start and stop signals lie in the range selected by the windows of the SCAs in the slow circuit.

Most important parameters of PL spectrometer are *timing resolution* and *count rate*, i.e. number of coincidences per unit time. The timing resolution of PL spectrometer is expressed as FWHM of response function of spectrometer to prompt coincidence of start and stop signal. Note that timing resolution depends on energy of start and stop photon. Measured PL spectrum is convolution of ideal spectrum with resolution function of spectrometer, therefore the timing resolution for β^+- source used is obtained from deconvolution of the spectrum. As ^{22}Na is usually used, the timing resolutions of PL spectrometers are mostly expressed for ^{22}Na. The timing resolutions of most of PL spectrometers in the world lie between 200 and 300 ps.

3.2   Doppler Broadening Spectroscopy

Kinetic energy of thermalized positron in the laboratory frame is negligible compared to that of surrounding electrons. Therefore momentum **p** of the annihilating electron-positron pair is determined by momentum of electron. The kinetic energy of annihilating pair is typically a few eV. The energy of annihilating photons in center-of-mass frame of the annihilation pair is $mc^2 = 511$ keV, where mc^2 denotes the rest energy of electron, and the photons are moving into opposite directions. In the laboratory frame the annihilation photons, however, deviate from anticollinearity due to nonzero momentum of annihilating pair. The vector diagram of momentum conservation in the 2γ − annihilation process is shown in Fig. 3.4. Longitudinal and transverse
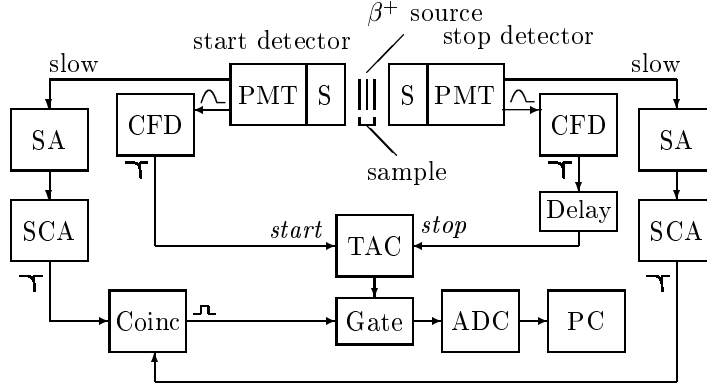
Figure 3.3 Schematic description of the fast-slow PL spectrometer.
S − scintillator, PMT − fast photomultiplier, CFD − constant-fraction-discriminator, TAC − time-to-amplitude converter, ADC − analog-to-digital converter, SA − spectroscopy amplifier, SCA − single-channel analyzer, Coinc − coincidence unit, PC − personal computer.

component of momentum $\mathbf{p}$ are denoted as p_L and p_T, respectively. The motion of the annihilating pair also causes a Doppler shift in the energy of annihilation photons measured in the laboratory system. The frequency shift $\Delta\nu/\nu \approx v_L/c$, where the longitudinal center-of-mass velocity v_L of the pair equals $p_L/2m$. The Doppler energy shift $\Delta E/E = \Delta\nu/\nu$, therefore

$$\Delta E = \frac{v_L}{c}E = c\frac{p_L}{2}. \tag{3.1}$$

Thus the Doppler energy shift is proportional to longitudinal component of momentum of annihilation pair and it therefore reflects the momentum distribution of electrons in matter. The magnitude of the Doppler energy shift can be estimated from the Heissenberg uncertainty relation

$$\Delta p\Delta x \geq \hbar , \tag{3.2}$$

where the uncertainty of coordination is of order of atomic size $\Delta x \approx 0.1$ nm. On the basis of the uncertainty relation and eq. (3.1) the Doppler shift of energy $\Delta E \approx 1$ keV is expected.

The Doppler shift of results in broadening of peak 511 keV in energy spectrum of annihilation γ rays. The line shape of this peak gives information about distribution of longitudinal component of momentum of annihilating pair. The system for measuring of line shape of annihilation peak is shown schematically in Fig. 3.5. High-resolution solid-state detector (usually high-purity germanium (HPGe) detector) is used for detection of annihilation γ ray. The signal from the detector is led through preamplifier (PA) into spectroscopy amplifier (SA) where it is amplified and shaped. The output signal from SA is digitized by analog-to-digital converter (ADC) and stored in computer (PC). Energy resolution of HPGe detectors lie around 1 keV at energy 511 keV. Note that even relatively small drift of the annihilation peak position during measurement can severely destroy information obtained from the spectrum. Therefore, stabilization of the spectrum is necessary. In our case the Doppler-broadening (DB) measurement consists of a number of separate steps. One step usually takes a half of hour. Partial spectrum obtained in given step is firstly shifted by similar computer procedure as that for PL spectra in order to compensate possible time drift of the peak. Total spectrum is then sum of shifted partial spectra from all the steps. Detailed description of DB spectrometer used in the present work is given in appendixes G and H.

Typical annihilation peak for metallic samples is shown schematically in Fig. 3.6 and it consists of central parabolic part and broader gaussian tails [47]. The central parabolic part represents
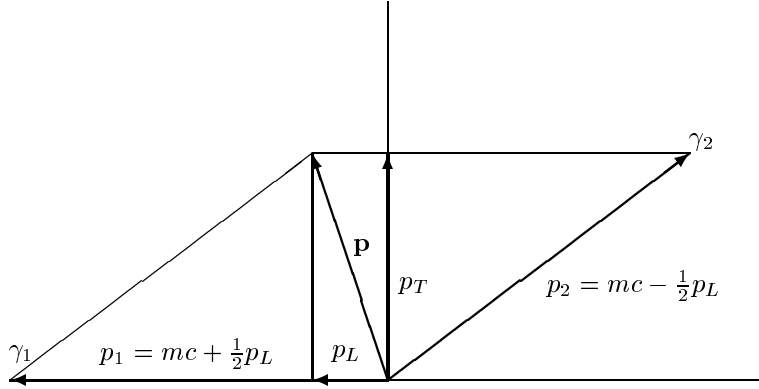
Figure 3.4 The vector diagram of the monentum conservation in 2γ annihilation process. The momentum of the annihilation pair is denoted by $\mathbf{p}$, p_l and p_T refer to longitudinal and transverse components, respectively.
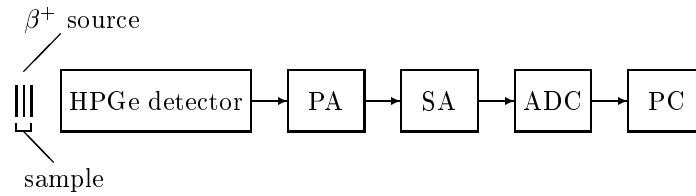

Figure 3.5 The schematic description of Doppler broadening spectrometer. PA – preamplifier, SA – spectroscopy amplifier, ADC – analog-to-digital converter, PC – personal computer.

contribution of positrons annihilating with conduction electrons. As momentum of core electrons is higher than that of conduction electrons, positron annihilations with core electrons contribute to the gaussian tails of the annihilation peak. A positron trapped in a defect sees reduced electron density. Normally density of core electrons is reduced significantly greater then that of conduction ones. It result in remarkable narrowing of annihilation peak with increasing concentration of positron traps.

The shape of the annihilation peak is described by so called S and W parameters. The S parameter is defined as relative area of the central part of the peak. On the other hand, W parameter represents relative area of gaussian tails of the peak, see Fig. 3.6. Clearly, the S parameter is a measure of positrons, which annihilate with the conduction electrons, while the W parameter represents a measure of positrons annihilating with the core electrons. Increasing number of defects in the material causes usually increase of the S parameter and decrease of the W parameter. Note that there is no general rule where exactly to place the boarders of areas used for calculation of S and W parameters. Usually the boarders are chosen in order to obtained maximal sensitivity of the parameters (it is usually for $S \approx 0.5$ [2, 86]) to the studied changes in the material and it differs from sample to sample.

Important task in analyse of DB spectra represents subtraction of background, which has to be made prior to calculation of the line shape parameters. The spectral background in the region of the peak consists of three components: (i) the pulses related to radiation from other sources (i.e.
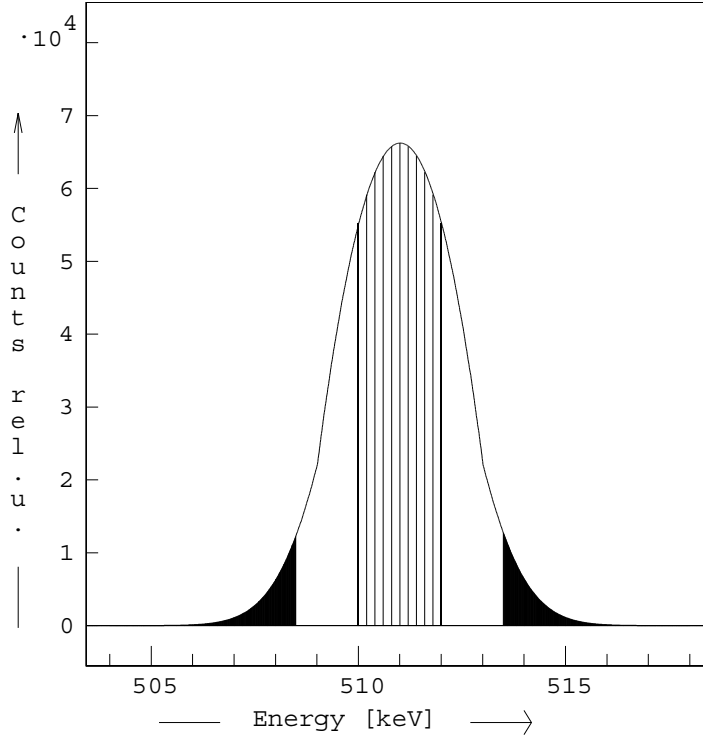
·10^4

7

6

5

4

3

2

1

0

Counts rel. u.

505   510   515

Energy [keV] ⟶

Figure 3.6 Schematic plot of the annihilation peak. Filled areas illustrate typical regions used for calculation of W parameter. Hatched area represents the region used for determination of S parameter.

the background radiation), (ii) the pulses from higher energy γ-rays (if any) from the positron source, for example 1274 keV γ-rays for the ^{22}Na source, and (iii) the pulses from annihilation γ-rays, but for which enough energy is lost from sensitive volume of the detector to put the count in the spectral distribution below the peak. A number of step-like functions, which approximate the spectral background, was suggested, see [87] and references therein. Comparison performed in [87] has revealed that these function are quite similar.

3.3   Methodological Development Performed in The Present Work

PL spectrometer with excellent timing resolution of 150 ps achieved at relatively high coincidence counting rate of 80 coinc./s was employed in the present work. Detailed description of the PL spectrometer is given in appendix A. The superior timing resolution of the PL spectrometer is crucial for proper detection of free positron component in experimental spectra. In metallic materials with relatively high density of defects, the free positron component is usually weak and exhibits lifetime well below 100 ps. Proper determination of lifetime and relative intensity of the free positron component is necessary for application of the trapping models. Hence, success of investigations in the present work could be achieved to large extent due to high resolution of the PL spectrometer.

It was found that long-term continuous exploitation of the PL spectrometer causes deterioration of its timing properties. Processes responsible for this undesired deterioration as well as procedures for its remedy were investigated in the present work. Results of these investigations are explained in appendix A. It was found that worsening of the timing resolution is caused by decreasing gain of fast photomultipliers (PMT). The deterioration of PMT's gain during long-term exploitation occurs due to damage of dynode surfaces caused by incident photoelectrons. The rate of the deterioration depends on voltage distribution along the dynode chain. The surface damage seems to be irreversible, however, remedy of deteriorated PMT's gain can be achieved by increasing of interdynode voltages, as was successfully applied on our PL spectrometer, see appendix A. The investigations performed in the present work have clearly shown that important parameter of each developed voltage divider is not only initial timing resolution obtained with it, but also long-term stability of this timing resolution. Four voltage dividers were tested in the present work, see appendix A, and optimal divider with sufficient timing resolution as well as its long-term stability was chosen. If gain of a PMT is insufficient to excite a CFD, it is possible to use fast preamplifier in order to increase amplitude of the fast signal. Use of fast preamplifier may improve signal-to-noise ratio and its positive impact on timing resolution was checked in the present work, see appendix A.

A modification of conventional fast-slow configuration of PL spectrometer was developed in the present work. Detailed description this modified PL spectrometer and results of its tests are given in appendix B. The modification consists in summing of energy signals in the slow circuit. The sum of start and stop energy signals is amplified and shaped in spectroscopy amplifier (SA) and lead to timing single channel analyzer (TSCA) with energy window adjusted to energy sum of the annihilation and the start γ-ray, i.e. 512 keV + 1274 keV (for ^{22}Na). The TAC signal form the fast branch is accepted only when the sum of the energy signals falls to the energy window of TSCA. The main advantage of the modified arrangement is improved throughput of the slow branch. As a result the coincidence count rate is enhanced almost by factor of two, keeping the excellent timing resolution unchanged, see appendix B.

Irradiated RPV steels contains significant amount of ^{60}Co activity. The ^{60}Co nucleus decays by almost simultaneous emission of two γ-rays with energies 1173 keV and 1332 keV. It is well-known that the two prompt photons emitted by ^{60}Co causes substantial distortion of measured PL spectra [88], which does not allow PL measurements of irradiated RPV steels using conventional PL spectrometers. Therefore, three-detector PL spectrometer was developed and tested in the present work. Detailed description of the three-detector PL spectrometer, its tests as well as Monte Carlo simulations of influence of ^{60}Co prompt contribution to fitted positron lifetimes and intensities are given in appendix C. The three-detector PL spectrometer accepts only 3-γ coincidences connected with positron annihilation (i.e. the start γ and the two anticollinear annihilation γ rays). In this way the undesired 2-γ prompt coincidences from ^{60}Co are suppressed.

The setup of the spectrometer differs from the previous one described in Ref. [88]. In particular, both the timing and the energy information of detected γ-rays is used for accumulation of PL spectra free from parasite contribution of the ^{60}Co decay. In addition to the start and the stop timing detectors (perpendicularly to each other), third detector was employed. This detector is placed in face-to-face geometry with the stop detector and detection of the second annihilation γ-ray in this detector, i.e. triple coincidence, is required, see appendix C. As the timing information is carried by the start and the stop detectors and the third detector serves as a gate checking the triple coincidence, requirements to timing resolution of the third detector are not high. Therefore, it is designed to provide precise energy selection, i.e. complementary information to that obtained the other two detectors, in expanse to timing information, for details see appendix C.

The three-detector PL spectrometer developed in the present work provides decrease of ratio of ^{60}Co to ^{22}Na by a factor of 200, see appendix C, which is two times higher than the value provided by spectrometer described in [88]. Moreover, timing resolution of our spectrometer was 220 ps which is remarkably better then 300 ps reached in [88]. Note that recently the timing resolution of our PL spectrometer of 177 ps was reached due to use of photomultiplier with better timing properties for detection of the stop γ-rays.

The investigation of irradiated RPV steels performed in the present work represents the first

exploitation of the three-detector PL spectrometer in study of these materials.

A new technique for precise absolute differential time calibration of TAC-ADC tandem was realized and tested in the present work. Description of the new calibration technique and its realization and testing are given in appendix D. The calibration procedure enables to determine width of each time channel independently, thus, possible non-linearities of TAC or ADC scale can be revealed. Moreover, the calibration procedure is very flexible and can be performed using the modular electronic conventionally used in timing measurements. The procedure was used for time calibration of the PL spectrometer employed in the present work, see appendix D. Width of each time channel was determined with precision of a few femtosecond. Monte Carlo simulations performed in the present work, see appendix D, have shown that the calibration technique gives correct results in practically all realistic conditions.

Appendix A

The paper was published in *Nuclear Instruments and Methods A* **443**, 557 (2000).

Appendix B

The paper was published in *Acta Physica Polonica A* **95**, 487 (1999).

Appendix C

The paper was published in *Nuclear Instruments and Methods A* **450**, 325 (2000).

Appendix D

The paper was submitted to *Nuclear Instruments and Methods A.*

4 Investigation of Reactor Pressure Vessel Steels

4.1 Introduction

Low alloy ferritic steels are high strength materials commonly used in construction of nuclear reactor pressure vessels (RPV). Typical vessel conditions during operation are a temperature around 300 °C and a pressure inside the vessel of 15 MPa. Mechanical properties of the material of RPV represent, therefore, important aspect for safety of nuclear power plants. Favourable mechanical properties of RPV steels, especially tensile properties and fracture toughness, are achieved by a suitable quenching and tempering treatment of the steels of proper chemical composition. Chemical composition of some commercial RPV steels is shown in Tab 4.1.

Table 4.1   The chemical composition (in weight %) of some commercial RPV steels. Base metal is denoted as BM, while weld metal as WM. [a] As: 0.008 wt.% , Co: 0.009 wt.% , [b] Solute Al: 0.012 wt.%

Material	15Kh2MFA[a] Cr-Mo-V BM	Sv-10KhMFT Cr-Mo-V WM	15Kh2NMFA Cr-Ni-Mo-V BM	A533-B[b] BM	A508 BM
C	0.16	0.37	0.16	0.19	0.19
Si	0.17	0.59	0.26	0.25	0.24
Mn	0.46	1.1	0.59	1.40	1.40
S	0.016	0.017	0.012	0.004	0.007
P	0.014	0.012	0.005	0.019	0.008
Cr	2.90	1.37	2.22	0.12	0.09
Ni	0.07	–	1.27	0.84	0.75
Mo	0.66	0.50	0.63	0.50	0.49
V	0.31	0.20	0.09	0.003	–
Cu	0.07	0.06	0.03	0.14	0.04

Material of RPV is subjected to irradiation of energetic neutrons ($E > 0.5$ MeV) during operation of a reactor. The neutron irradiation results in substantial changes of microstructure of RPV steels. These microstructural changes cause remarkable deterioration of mechanical properties of material known as *neutron irradiation-induced embrittlement* of RPV steels. The embrittlement of RPV steels limits significantly lifetime of nuclear reactors. For mainly economical reasons it is, however, necessary to keep nuclear power plant station at least working to a projected lifetime of about 30 years. The operation of reactor must be fully safe during whole this period. For these reasons surveillance specimens are used during operation of a reactor. These specimens are made from the same materials as RPV and they are placed in the outer shell of reactor. It means that the surveillance specimens are subjected to almost the same irradiation conditions as the material of RPV and they serve as indicators of an extent of neutron embrittlement of the material of RPV.

The embrittlement of RPV steel is more pronounced problem in Eastern (Russian) types of nuclear reactors (VVER-440, VVER-1000) than in other types of reactors. It is due to narrower gap between the outside surface of the core barrel and the inside surface of RPV than in Western RPVs. The relatively small diameter ($\Phi_{in} = 3542$ mm in case of VVER-440/V-230 type) facilitates

transport and installation of the RPV. On the other hand, the neutron fluxes and consequently neutron fluency on the RPV wall is higher on VVER-440 type reactors than in other equivalent types in general.

The neutron embrittlement of RPV steels may only be removed by thermal annealing of the material. The search for an effective temperature-time regime of the thermal annealing is, therefore, highly necessary. Clearly without some knowledge about mechanism of the neutron irradiation-induced microstructural changes of RPV steels this searching is not very effective. Despite a number of techniques used for characterization of microstructure of irradiated RPV steels, the processes which lead to the neutron embrittlement remain still unclear [89, 5, 90]. Hence, additional microstructure studies of RPV steels which would bring new information about these processes are strongly needed.

Microstructural changes of RPV steels induced by neutron irradiation involves a number of processes. Clearly vacancies and interstitials are created by neutron irradiation. It is known that the defects produced by neutron irradiation are not homogeneously distributed but the damage consists of displacement cascades within which the irradiation-induced defects concentration is locally very high [91]. Complicated processes including migration of the irradiation-induced defects and their interactions with each other (recombination of vacancies and interstitials, clustering of vacancies or interstitials, creation of dislocation loops) and also with defects present already in the non-irradiated material (recovery of vacancies and interstitials and/or clusters in sinks, capture of vacancies by precipitates, creation of complex clusters containing point defects and atoms of alloy elements) take place during neutron irradiation. Moreover, the irradiation-induced precipitates probably play an important role in the neutron embrittlement of RPV steels [45]. Note that some precipitates existing in the material prior to irradiation may be also dissolved by neutron irradiation. Clearly, the irradiation-induced microstructural changes strongly depend not only on the irradiation conditions (neutron flux, fluence, irradiation temperature), but also on the chemical composition of the material and the defect structure present prior to irradiation. Particularly, it should be pointed out that completely different results were obtained on RPV steels irradiated at temperature below 160 °C and the same materials irradiated at temperature ~ 270 °C (i.e. close to the operating temperature of VVER reactors) [45, 92].

Properties of the RPV steels and influence of thermal treatment on them are routinely investigated by macroscopic methods such as Charpy V-notch and tensile tests [93]. A number of semi-empirical laws, based on the macroscopic data, have been established but unfortunately, these laws are never completely consistent with all data and do not yield to the wanted accuracy [94]. Various microscopic techniques like TEM [95, 96], field ion microscopy (FIM) [97, 98, 99], small angle neutron scattering (SANS) [100], energy-compensated optical position-sensitive atom probe (ECOPoSAP) [90], Mössbuer spectroscopy (MS) [101], etc., were used to clarify the phenomena involved in neutron embrittlement of RPV steels. Interpretation of the results obtained by various techniques is, however, very difficult due to large number of constituents in the chemical composition of the RPV steels as well as complex defect structure present already in the non-irradiated material.

Positron annihilation spectroscopy (PAS) gives valuable information about defects in RPV steels due to its high sensitivity to open volumes with lower electron density [2]. Particularly vacancy-sized defects of sizes below ≈ 5 nm, which cannot be observed by TEM, may be easily identified by positron-lifetime (PL) measurement. As these types of defects are certainly created during irradiation, PAS may bring valuable information about irradiated-induced changes in RPV steels. Several PL and DB studies of RPV steels have been performed so far [92, 102, 45, 103, 104, 105, 106, 107, 101]. It turned out that positron parameters especially S-parameter are strongly correlated with the irradiation induced variations of hardness, i.e. with changes of mechanical properties [103, 102].

In general, irradiation-induced microcavities and small vacancy clusters were found by PL measurement in all types of RPV steels irradiated at temperatures below ~ 150 °C [92, 102, 45, 107]. The size of irradiation-induced microcavities in RPV steels is substantially lower than the size of those which were found in PL investigation of neutron-irradiated α-Fe [105]. Microcavities consisting of 6-9 vacancies were found in PL study of A533-B RPV steel irradiated at temperature

150 °C to fluence 3.5×10^{22} m^{-2} [92]. Microcavities consisting of ~ 6 vacancies were created by irradiation of ASTM A508 RPV steel at room temperature up to fluence 10^{20} m^{-2} [107]. Investigation of VVER-440 type Cr-Mo-V RPV steel irradiated at temperature 160 °C to fluence 4×10^{23} m^{-2} by means of PL spectroscopy performed in ref. [45] revealed presence of microcavities containing about 15 vacancies. It was not possible to separate the component belonging to small vacancy clusters in PL spectra of irradiated RPV steels [92, 45]. However, the presence of irradiation induced small vacancy clusters was unambiguously indicated by increasing lifetime of the component which came from positrons trapped at dislocations in unirradiated steels [92, 45]. Clearly, in the case of irradiated steels this component represents superposition of contribution of positrons trapped at dislocations and those trapped in irradiation-induced small vacancy clusters. Both the size and concentration of the irradiation-induced microcavities and vacancy clusters increase with increasing neutron fluence [105].

On the other hand, less clear situation was found in RPV steels irradiated at temperatures close to the operation temperature of reactors (i.e. $\sim 270 - 300$ °C). Only small vacancy clusters but no microcavities were found in A533-B RPV steel irradiated at 290 °C to fluence 2×10^{23} m^{-2} [92]. The presence of the small vacancy clusters was again indicated by increase of lifetime of the component belonging in the case of unirradiated steels to positron trapped at dislocations. Similarly no microcavities were found in RPV steel irradiated at 290 °C to fluence 5×10^{20} m^{-2} [103]. Only mean positron lifetime was measured on set of Cr-Mo-V RPV steels irradiated at temperature 265-270 °C [45] to fluence from 2.3×10^{22} m^{-2} to 3.3×10^{23} m^{-2}. The mean positron lifetime of irradiated samples was by about 6 % higher than that of unirradiated ones for majority of specimens, but the mean positron lifetime of the two irradiated samples was bellow that of unirradiated ones. This surprising effect was interpreted as a consequence of positron annihilations in irradiation-induced precipitates. Nevertheless, it is not clear why the two samples exhibited the mean positron lifetime bellow that of the non-irradiated steel and the mean positron lifetime of the other irradiated samples lay above that of non-irradiated steel. Note that only small increase or even decrease of the mean positron lifetime of irradiated Cr-Mo-V steels compared to non-irradiated ones clearly suggest that only few (if any) microcavities are present in the irradiated samples.

4.2   Investigation of RPV Steels in the Present Work

Base metal (BM) and weld metal (WM) of VVER-440 type Cr-Mo-V RPV steel, BM of VVER-1000 type Cr-Ni-Mo-V RPV steel and A533-B RPV steel were studied in the present work. In addition the two model alloys with the same composition as the Cr-Ni-Mo-V steel but with enhanced concentration of Cu and P, respectively, were investigated. The chemical composition and denotation of the samples is given in appendix H.

Detailed knowledge about defect structure of non-irradiated RPV steels is quite necessary in order to distinguish the irradiation-induced defects from those already present in the non-irradiated steels. Note that the initial defect structure in the non-irradiated RPV steel samples studied by PL spectroscopy was found to produce measurable effects of the same order of magnitude as the defects produced during the neutron irradiation [92]. The results of PL investigation of non-irradiated RPV steels performed in the present work are given and discussed in appendix E. The samples exhibited strongly non-uniform spatial distribution of dislocations where the non-distorted regions almost without dislocations are separated by distorted ones with high dislocation density. Therefore simple trapping model (STM) [2] cannot be used in interpretation of measured PL spectra (for more detailed discussion see appendix E). For these reasons, the modified trapping model (MTM) has been developed in the present work with purpose to explain behaviour of positrons in such materials. Description of the MTM is given in appendix F. The MTM provides not only self-consistent interpretation of measured PL spectra of RPV steels but generally it is also suitable for self-consistent interpretation of PL spectra of all metals with polygonized or cellular dislocation substructure. Therefore, the MTM was used in the present work in interpretation of PL spectra of pure aluminium plastically deformed at liquid nitrogen temperature, which represents a materials

with well known microstructure. The physical quantities calculated from PL spectra using the MTM were compared with those obtained by the other methods (TEM, electrical resistivity) and good agreement was found. The comparison serves as a test of reliability of the MTM and it is given in appendix F.

As a next step of the present work neutron irradiation-induced changes of microstructure of the RPV steels were studied. Irradiation conditions of various RPV steel samples studied in the present work are listed in appendix H. All samples were irradiated at temperature 280 °C . Irradiated samples contained substantial amount of ^{60}Co activity. This isotope emits almost simultaneously two photons with energy 1173 keV and 1332 keV, respectively. Energetic spectrum of Cr-Mo-V steel irradiated at temperature 270 °C, flux $\phi = 3.87 \times 10^{16}$ m^{-2}s^{-1} to fluence $\Phi = 5.26 \times 10^{24}$ m^{-2}. (sample B6, see appendix H) is shown in Fig. 4.1 as a typical example. This spectrum was
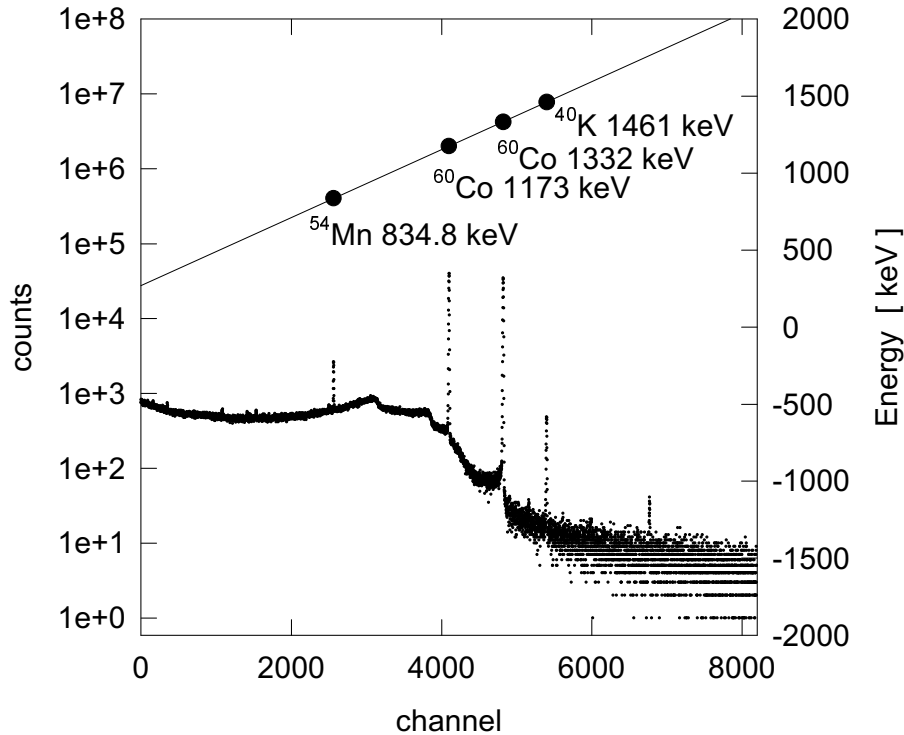

Figure 4.1 Energy spectrum of Cr-Mo-V RPV steel irradiated at temperature 270 °C , flux $\phi = 3.87 \times 10^{16}$ m^{-2}s^{-1} to fluence $\Phi = 5.26 \times 10^{24}$ m^{-2}. The spectrum was measured by high purity germanium detector.

measured with high purity germanium detector ORTEC with energy resolution 1.9 keV (FWHM) and peak-to-Compton ratio 68:1 for E$_\gamma = 1.33$ MeV energy. It is well-known that the two prompt photons emitted by ^{60}Co cause substantial distortion of measured PL spectrum [88]. Therefore, triple-coincidence PL spectrometer was developed in the present work which accepts only 3-γ coincidences belonging to ^{22}Na. The setup of the spectrometer differs from the previous one described in Ref. [88]. The spectrometer developed in the present work provides decrease of ratio of ^{60}Co to ^{22}Na by a factor of 200, which is two times higher than the value provided by spectrometer described in [88]. Timing resolution of our spectrometer was 220 ps which is remarkably better

then 300 ps reached in [88]. Note that recently the timing resolution of our spectrometer of 177 ps was reached due to use of photomultiplier with better timing properties for detection of the stop γ-rays. Complete description of the triple-coincidence spectrometer developed in the present work is given in appendix C.

The investigated specimens of RPV steels were irradiated under various conditions (fluence, flux), see appendix H. The main topics, which should be solved in the present investigation, were

(i) Comparison of microstructure of irradiated RPV steels with that of non-irradiated ones and determination of neutron irradiation-induced microstructure changes.

(ii) Detailed characterization of irradiation-induced defects and dependence of their density, size and arrangement on fluence and flux of irradiation.

(iii) Determination of influence of different flux on irradiation induced defects.

(iv) Comparison of radiation-induced changes in various RPV materials.

(v) Investigation of changes of microstructure in thermally aged RPV steels. Study of microstructural evolution of irradiated RPV steel subjected to subsequent heat treatment.

The investigations were performed by means of PL spectroscopy and DB measurements correlated with TEM. The TEM measurements were performed by Dr. J. Kočík and Dr. E. Keilová. The use of two independent techniques is necessary due to complex microstructure of the studied specimens. Results of the studies of the non-irradiated RPV steels performed in the present work are given in appendix E. Results of the investigations of irradiated RPV steels performed in the present work are given and discussed in appendixes G and H.

4.3   Summary

The main results and conclusions obtained in investigations of RPV steels performed in the present work may be summarized into the following items

(i) Study of non-irradiated specimens have shown that positrons are trapped mainly at dislocations in all RPV steels studied. Lifetime of the trapped positrons is ≈ 150 ps. In the case of VVER-type steels, a small fraction of positrons may be trapped at the vanadium-matrix interface.

(ii) Spatial distribution of dislocation is strongly non-homogeneous. Regions with low number of dislocations (cells) are separated by distorted layers with high dislocation density (cell walls). The inhomogeneous arrangement of dislocations does not allow use of the STM. Therefore, the MTM, which enables proper determination of dislocation density in the specimens, was developed in the present work. Using the MTM the specific trapping rate for α-Fe dislocation was determined to be 0.36×10^{-4} m^{2}s^{-1}.

(iii) The western-type RPV steel A533-B contains higher number of screw dislocations compared to edge ones than the VVER-type steels.

(iv) Small vacancy clusters with size comparable to 5 vacancies and fine radiation-induced precipitates are introduced into RPV steels due to irradiation. Larger radiation-induced vacancy clusters may collapse into dislocation loops.

(v) Concentration of the radiation-induced vacancy clusters slightly increases with increasing fluence. No change of size of the vacancy clusters with neutron fluence was found. Number of the fine radiation-induced precipitates increases with fluence. The fine precipitates are formed preferentially in vicinity of dislocations.

(vi) Dislocation density remains practically unchanged in the irradiated RPV steels.

(vii) Radiation-induced changes of microstructure are determined mainly by total neutron fluence and seems to be independent on flux.

(viii) Complete disappearance of radiation-induced defects visible by TEM (fine precipitates) was observed in irradiated RPV steels subjected to subsequent annealing at 475 °C for 165 h. On the other hand, the PL component, which comes from positrons trapped in the radiation-induced vacancy clusters (lifetime 250 ps) exhibits remarkable increase in the subsequently annealed RPV steels. It means that the small vacancy clusters, which are invisible by TEM, are still present in the annealed specimens despite of disappearance of the radiation-induced small precipitates. This effect was proved also by DB measurement. In order to understand behavior of the radiation-induced small vacancy clusters with increasing temperature, it is necessary to perform additional PL measurements of isochronally annealed irradiated specimens. Such studies are currently in progress. Intensity of the dislocation component (lifetime 150 ps) decreases in the annealed specimen as a result of polygonization observed also by TEM.

(ix) Thermal ageing of RPV steels at 295 °C for 5 or 10 years at position with negligible neutron flux does not lead to significant changes of microstructure, except of some polygonization of dislocation substructure.

Appendix E

The paper was published in *physica status solidi (a)* **178**, 651 (2000).

Appendix F

The paper was published in *physica status solidi (a)* **180**, 439 (2000).

Appendix G

The paper was published in *Effects of Radiation on Materials, 19th International Symposium, ASTM STP 1366,* Ed. M.L. Hamilton, A.S. Kumar, S.T. Rosinski, M.L. Grossbeck, American Society for Testing and Materials, 1999.

Appendix H

The paper was accepted for publication in *Journal of Nuclear Materials.*

5 Ultra-fine grained Materials

5.1 Introduction

Nanocrystalline (NC) materials are polycrystals with the mean grain size below 10 nm [6]. Sub-microcrystalline polycrystals with the mean grain size of about 100 nm are often called ultra-fine grained (UFG) materials [7]. In recent years the NC as well as the UFG materials have attracted much interest of researchers in the field of material science. It is connected with new, unusual properties caused by significant volume fraction of crystallite interfaces in these non-traditional materials.

5.1.1 Atomic Arrangement

A schematic cross-section through a NC material is shown in Fig. 5.1.   As far as the atomic
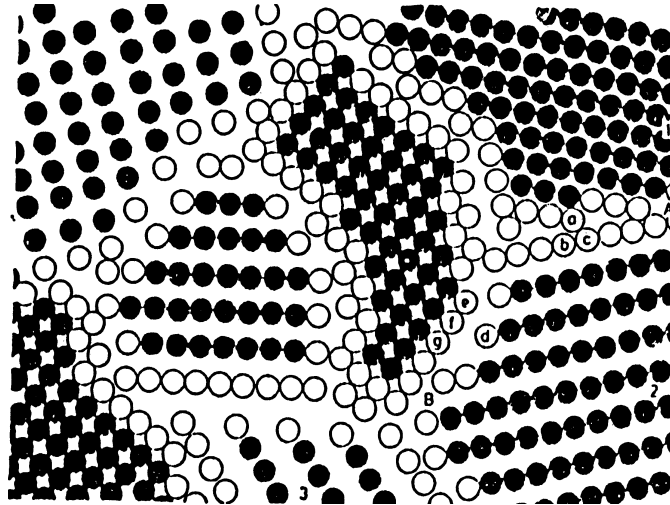

Figure 5.1 Schematic representation of NC material distinguishing the atoms associated with the individual crystals (full circles) and those situated in crystallite interfaces (open circles) [6]. The boundary atoms are shown in regular lattice positions but in reality will relax to form different atomics arrangement.

structure is concerned, two kinds of atoms may be distinguished:

   (i) "crystal atoms" (full circles), the nearest-neighbour configurations of which correspond to the lattice configuration;

   (ii) "boundary atoms" (open circles) characterized by the nearest-neighbour configurations which are different from the lattice configuration.

Clearly, the "crystalline atoms" are situated inside grains, while the "boundary atoms" in the crystalline interfaces. Hence, in terms of nearest-neighbour configuration, a NC material consists of a crystalline component (formed by all the "crystalline atoms") and a boundary component (formed by all the "boundary atoms"). The essential difference of the NC materials from the coarse-grained ones is that the boundary component is significant and cannot be neglected. The

atomic structure of all the crystal is identical, e.g. if the NC material is copper, all crystals have a face-centred cubic (fcc) lattice. On the other hand, the atomic structures of the boundaries are different because their atomic arrangement depends, among other parameters, on the orientation relationship between the crystals. As the orientation relationship between various crystallites is different, also the atomic arrangement differs from boundary to boundary. If the crystallites forming the NC material are oriented at random, the same applies to all boundaries. As NC materials contain typically about 10^{19} boundaries per cubic centimeter, the interfacial component represents the sum over 10^{19} atomic arrangements, all of which are different. If the interatomic spacings in all of these 10^{19} structures are uncorrelated in the sense that certain interatomic spacings do not occur preferentially, the interfacial component is expected to exhibit no preferred interatomic spacing apart from excluding interatomic penetration. In other words, the interfacial component represents a structure, which exhibits no short-range order. Note that it does not imply that grain boundaries are disordered. In fact, every boundary is assumed to have a two-dimensionally ordered structure, the periodicity and interatomic spacing of which are different from boundary to boundary.

Thus, the boundary component represents a new kind of structure, which differs from the long-range order, typical for crystals, as well as from the short-range order, characteristic for glasses. The physical reasons for this new kind of structure of a solid material are the crystallographic constraints imposed on the atoms in the cores of the boundaries by the adjacent crystal lattices of different orientations. In grain boundaries, the atoms can only relax into structures compatible with the adjacent crystal lattices. In glasses and crystals, no constraints of this type exist.

The atomic structure of the boundaries in NC materials was experimentally studied by X-ray diffraction [108]. To test the atomic arrangement in the boundaries, the interference functions were computed by assuming the boundary regions between crystals to be short-range ordered or to consist of randomly displaced atoms. The experimentally observed interference function can only be matched by the computations if the interfacial component of a NC materials is assumed to have no short-range order. A number of indirect evidences that the boundary component exhibits no short-range order were obtained also by other techniques, for review see [6].

5.1.2 Preparation Techniques

NC materials

In principle, any method suitable for preparing a polycrystalline material with crystal size of a few nanometer and a random texture may be utilized to generate NC materials.

The experimental arrangement used most frequently so far is so called gas condensation method (GCM) [109, 110] and its principle is shown in Fig. 5.2. The material is evaporated into an inert gas atmosphere (usually helium or argon, pressure about 1 kPa). As a result of interatomic collisions with the helium or argon atoms, the evaporated atoms lose kinetic energy and condense in the form of small crystals which accumulate on a vertical cold finger in the form of a loose powder, the crystal size of which is of a few nanometer. After restoring high vacuum (less then 10^{-6} Pa) the powder is stripped off from the cold finger and funneled into a piston and anvil device where it is compacted (pressure up to 2 GPa) into a nanocrystalline material. Naturally, sputtering, electron gun or laser evaporation may be applied instead of thermal evaporation.

NC materials with the mean grain size of a few nanometer can be provided by the GCM. The as-prepared samples are usually disc shaped with diameter below 10 mm and thickness 0.1-0.3 mm [6]. Density of the as-prepared NC samples varies between 70 % and 90 % of the crystalline density (depending on the material and the compactization procedure). The lower density of NC materials is due to residual porosity inside them. During the production, gaseous impurities in the preparation chamber are often adsorbed on the powder grain surfaces and therefore subsequently incorporated into the NC material [111]. Oxygen and water vapour are the dominant gas impurities in NC materials prepared by GCM. Total concentration of the gas impurities varies from 1 at.% to 10 at.%.
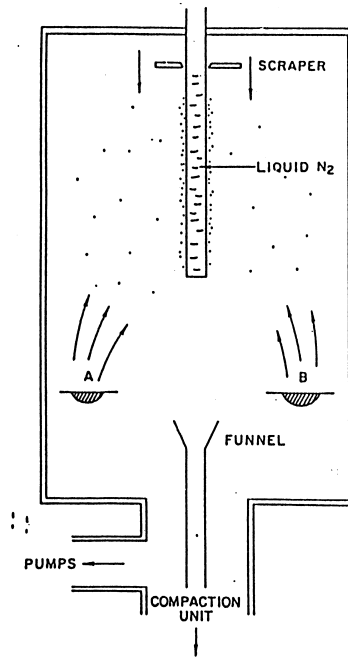
Figure 5.2 Schematic description of a gas condensation chamber for the synthesis of NC materials [6]. The material evaporated from sources A and/or B condenses in the gas and is transported via convection to the liquid nitrogen-filled rotating cold finger. The powder of small crystals accumulating at the cold finger is subsequently scraped from the cold finger and compacted in situ.

UFG Materials

The NC materials produced by the GCM exhibit small grain size, on the other hand, disadvantage of this technique consists in fact that nanocrystals prepared by the GCM contain gas impurities and residual porosity [6, 111]. Recently it has been shown that very fine crystalline structures with the mean grain size from 50 to 200 nm can be achieved by severe torsion plastic deformation (SPD), with low straining rate (10^{-4} s^{-1}), performed at room temperature with simultaneous application of high pressure (3-6 GPa) [7, 8]. The principle of the method is described in Fig. 5.3. The SPD technique leads to specimens with larger grain size, however, it has a number of advantages. Contrary to the GCM, (i) no residual porosity was found in the samples produced by SPD, (ii) high purity UFG materials can be prepared and (iii) one can produce massive samples (sheets, rods).

Note that the UFG materials may be produced also by equal channel pressing (ECAP) [8, 112, 113]. During ECAP the specimens are subjected to shear deformation by pressing through two channels of equal cross-sections intersecting at an angle ϕ (often $\phi = \pi/2$). The principle of ECAP technique is illustrated in Fig. 5.4. In this procedure, a pure homogeneous shear is localized in the plane of intersection of the two channels and the as-deformed dimensions are identical to the initial ones so that repetitive pressing can be continued up to the required level of plastic straining. The ECAP technique provides UFG materials with grain size approximately 200 nm, i.e. higher then SPD method.
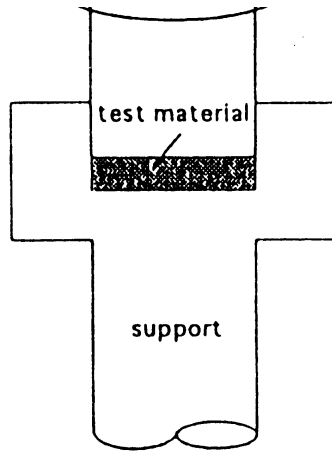
178

Figure 5.3 Schematic illustration of severe plastic torsion deformation technique [8]

5.1.3   Microstructure of UFG Materials

Although the preparation technique (SPD) of UFG materials differs essentially from the way of producing NC ones, microstructure of both the materials exhibits a number of similar features. Bright-field TEM image of UFG Ni, taken from Ref. [114], is shown in Fig. 5.5.   It represents typical example of microstructure of UFG materials. As one can see in the figure regions almost free of dislocations (grain interiors) are separated by distorted regions with high dislocation density. Schematic description of the structure of UFG materials is given in Fig. 5.6.   Similarly to the NC materials also the UFG ones can be divided in two regions [7]:

 (i) Non-distorted regions (grain interiors) with low dislocation density (about 10^{12} m^{-2}), atomic arrangement inside the non-distorted regions remains the same as in conventional coarse-grained materials.

 (ii) Distorted region situated along grain boundaries with high dislocation density (over 10^{15} m^{-2}) and high elastic strains of about 3-5 %[7]. Atomic arrangement inside the distorted regions differs substantially from that in conventional coarse-grained materials. Thickness of the distorted regions is approximately 10 nm [7].

5.1.4   Physical Properties

Both NC and UFG materials exhibit a number of extraordinary physical properties, which are connected with significant volume fraction of the "boundary atoms" , i.e. atoms situated inside the interfaces between grains.

   The UFG and NC materials exhibit advantageous mechanical properties compared to conventional coarse-grained materials, in particular high strengthened state and high strain rate superplasticity [8, 112, 115]. It is illustrated in Fig. 5.7, where the flow stress-strain curve is plotted for UFG Cu (grain size of 210 nm) prepared by ECAP [115].   The strain-stress curve for the UFG Cu (1) is compared with that for conventional coarse-grained Cu (2), see Fig. 5.7. It is seen that the flow stress dependence on compression strain of UFG Cu has a different shape from that of conventional copper material. The UFG Cu exhibits significantly higher yield stress then the conventional Cu. For the UFG Cu remarkable strain hardening effect takes place within a narrow strain range at the initial stage of deformation and it is followed by a long stage deformation almost with no hardening, see Fig. 5.7. On the other hand, the conventional Cu exhibits hardening
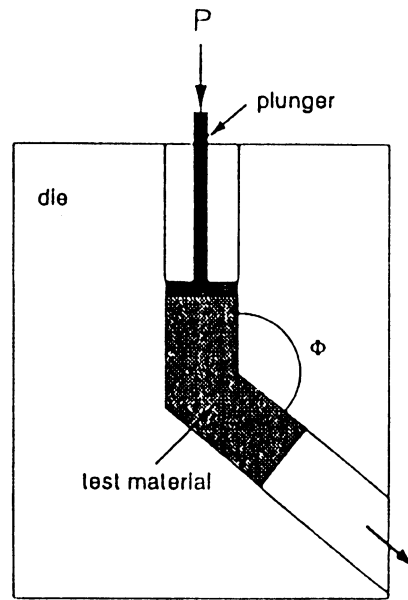
179

Figure 5.4 Schematic description of equal-channel pressing technique [8].

during whole plastic deformation. At the same time the ductility of UFG Cu is high. Specimens did not fracture even after the maximum strain of 83 % applied in the experiments [115].

It was observed that conventionally brittle ceramics become ductile and give rise to large (e.g. 100 %) plastic deformations at low temperature (e.g. 293 K) if the ceramic materials were generated in the NC form [116]. The ductility seems to originate from the diffusive flow of atoms along the inter-crystalline interfaces. NC iron-whiskers (crystal size 5-30 nm) produced by chemical vapour deposition technique [117] showed extraordinary strength up to 8 GPa [118].

NC and UFG materials are characterized also by enhanced diffusivity. For example, measurements [119] of the self-diffusivity D (^{67}Cu tracer) in NC Cu (crystal size 8 nm, temperature range 293-393 K) revealed an enhancement of D by a factor of about 10^{19} in comparison with lattice diffusion. This remarkable enhancement may be understood in terms of the high boundary density which provides a connective network of short-circuit diffusion paths.

Enhanced solid solubility was reported for NC materials. The miscibility of a solute A is controlled by the chemical potential μ_A of A in a given solvent B. Clearly, if the atomic structure of B is changed, the chemical potential and hence the solubility of A in B may be enhanced or reduced. As a consequence the solute solubility of NC materials is expected to be different from that in single crystals or in glasses of the same chemical composition. Indeed, the increase of the solubility of Bi in Cu from less than 10^{-4} at.% (lattice solubility) to about 4 at.% (solubility in NC Cu) was found [120].

Measurements of the average coefficient α of thermal expansion for NC Cu (grain size 8 nm) revealed approximately two-times higher value than in coarse-grained Cu [6]. Similar enhancement of α was observed also for NC Pd and TiO$_2$. The crystalline component contributes insignificantly to the enhancement of α. It leads to the thermal expansion coefficient of the boundary 5-6 times higher than that for single crystal [121]. Thus, by varying volume fraction of the grain boundaries (grain size) the thermal expansion of NC materials can be tuned to any predetermined value between the expansion of the crystal lattice and the boundary.

The NC and UFG materials exhibit changes in Curie temperature and saturation magnetization compared to conventional coarse-grained materials [122, 123, 120]. For example, measurements
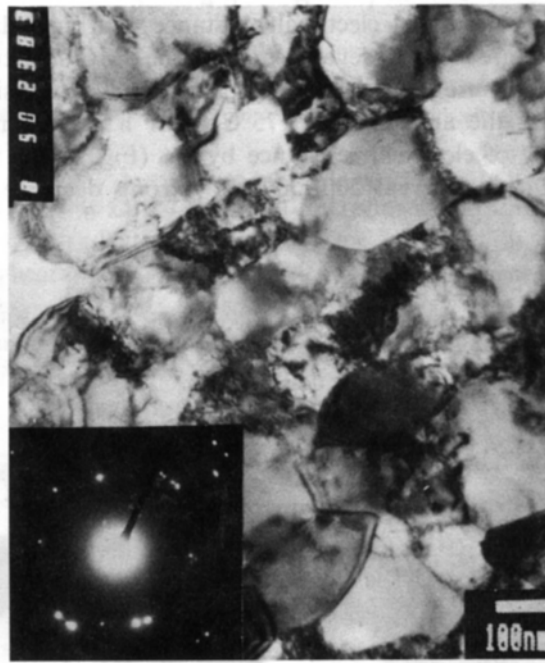
Figure 5.5   Bright field TEM image of UFG Ni prepared by SPD [114]

of the saturation magnetization M_s of NC Fe (grain size 6 nm) revealed a reduction of M_s from 220 e.m.u.g^{-1} (coarse-grained α-Fe) to about 130 e.m.u.g^{-1} [120].

Preparation of multi-phase NC and UFG materials is very promising way in looking for new materials with tunned physical properties. Preparation of multi-component NC and UFG materials results in a mixture of crystals of different chemical compositions. The great advantage of these "NC alloys" or "UFG alloys" is that they can be generated irrespective of the miscibility of the components, the type of chemical bonding of the various phases, the molecular weight, etc. Obviously such "NC or UFG alloys" deviate from an ideal solid solution. However, especially for the "NC alloys" the deviation is relatively small because about 50 % of the atoms (molecules) of any crystallite are situated in the interfaces, where different types of atoms are mixed on an atomic scale.

5.1.5   PL Spectroscopy on NC and UFG Materials

A number of techniques including X-ray diffraction (XRD) with comparative model calculations of the interference function [108], high-resolution electron microscopy [124], transmission electron microscopy (TEM) [114, 125], electrical resistometry [114], scanning differential calorimetry (DSC) and microhardness measurements [114], as well as Mössbauer spectroscopy [126] have been used for investigation of NC and UFG materials so far. Nevertheless, the knowledge about microstructure of NC and UFG materials still remains incomplete. In particular, there is lack of detailed information about defects in these materials. Especially, information regarding kinds of defects present in the boundary component (interfaces between grains) is desired. As relatively broad distribution of the nearest-neighbor atomic distances is expected in the interfaces between crystals and was also confirmed by XRD measurements [108], an interesting question is whether also some size distribution for defects can be found in the interfaces. Another open question is whether all defects are situated in the boundary component only or if some defects are present also inside the grains. Positron-lifetime (PL) spectroscopy is powerful method for studying lattice defects in
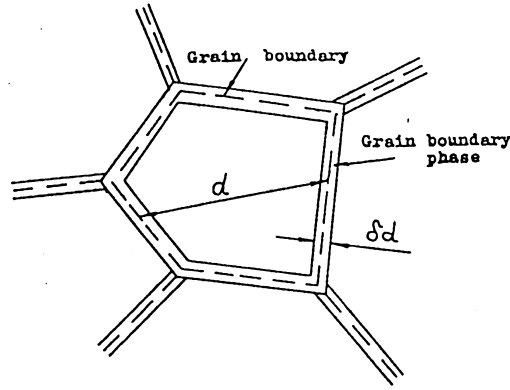
Figure 5.6 Schematic illustration of the structure of the UFG materials [7]. The symbol d denotes the grain size (obtained by TEM), while δd is the physical thickness of the distorted regions.

solids [2]. It provides valuable information not only about type of open-volume defects present in specimen, but also their sizes and concentrations. Moreover, PL spectroscopy represents non-local and non-destructive experimental technique and no special procedure for preparation of specimens is necessary. Hence, PL spectroscopy is an ideal tool for investigations of defects in NC and UFG materials.

A number of PL investigations [9, 10, 127, 128, 129] of NC materials prepared by GCM have been performed so far. The results obtained by different authors on various NC materials exhibit some similar features, which can be summarized as follows:

1. Two main components with lifetime 150-190 ps and 300-400 ps, respectively, were found in PL spectra. The first component can be ascribed to vacancy-sized volumes in the interfaces. The second one corresponds to larger defects with size from 5 to 15 vacancies. These larger defects are called microvoids (some authors use also term nanovoids) and it is assumed that they are situated at triple junctions (triple points) of interfaces.

2. It is not clear whether there is some size distribution for both types of the defects. In all cases experimental PL spectra of NC materials were well-fitted by finite number of discrete exponential components. No attempt of continuous decomposition of PL spectra to obtain shape of size distributions for the defects has been reported so far for NC materials.

3. An additional long-lived component with lifetime of a few nanoseconds and relative intensity usually below 10 % was found in PL spectra of NC materials. The long lifetime clearly indicates that this component comes from ortho positronium (o-Ps) pick-off annihilation. It means that o-Ps is formed in NC materials. It is assumed that o-Ps formation occurs at the internal surfaces of large pores (missing grains) present in NC materials prepared by GCM. It was shown that both the lifetime and the relative intensity of this long-lived component depend on pressure of compactization [10]. Note that NC materials represent the only case, where o-Ps formation occurs in bulk metallic material.

4. Although authors usually explain the two main components as positron trapping at defects in the interfaces, it remains unclear whether there are some defects present inside the grains. One can be only sure that there are defects present at the interfaces. However, it does not imply that the grains are completely defect-free as there is possibility that some defects
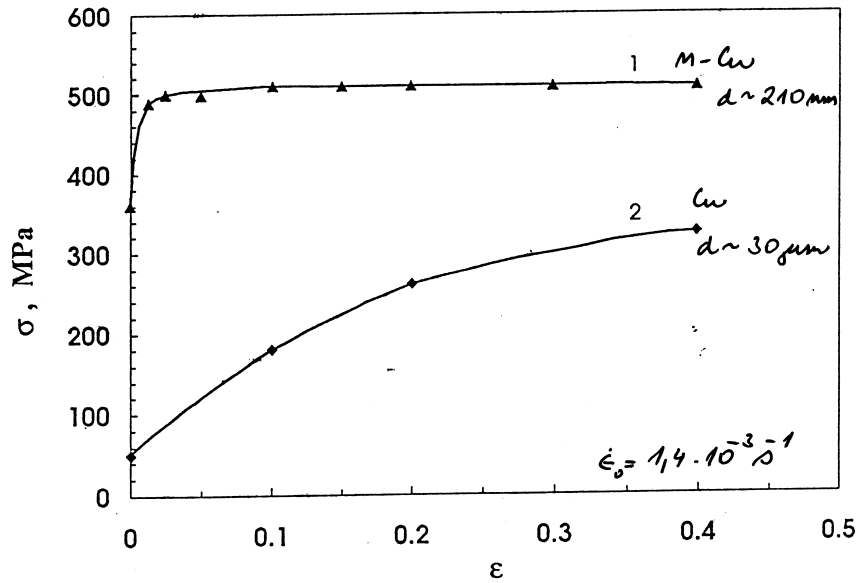
Figure 5.7 The true stress-strain curves for UFG Cu with the mean grain size of 210 nm (1) and coarse grained Cu with the mean grain size 30 μm (2). Compression testing was performed at room temperature with rate $\dot{\varepsilon} = 1.4 \times 10^{-3}$ s^{-1} [115].

inside grains may contribute to some of the two main components mentioned in the first item.

The results obtained on various NC materials using PL spectroscopy by different authors are compared in Tab. 5.1. Each materials in the table is characterized by chemical composition, grain size and in the case of NC materials prepared by GCM also by compactization pressure. The timing resolution (FWHM of resolution function for ^{22}Na positron source) is given in the fifth column of Tab. 5.1. Lifetimes and relative intensities of exponential components resolved in PL spectrum are listed in the next columns in Tab. 5.1.

There is only one PL study of UFG materials reported in literature [131], in which UFG Cu and Ni prepared by SPD were studied. The specimens prepared by SPD were, however, subjected to annealing at 175 °C for 30 min prior to PL measurement. Thus, the obtained results do not correspond directly to as-prepared state of these UFG materials. Two components with lifetime 160-170 ps and 300-330 ps were found in PL spectra of UFG Cu and Ni in [131] and these results are also included in Tab. 5.1. One can see that PL spectra of the UFG specimens are very similar to those of the NC materials, except of the absence of the long-lived o-Ps component. The latter fact is not surprising as there are no pores in UFG materials prepared by SPD contrary to NC ones provided by GCM, see section 5.1.2.

The ratio I_2/I_1 of relative intensities of positrons trapped in larger defects (microvoids) to that of positrons trapped in vacancy-like defects for UFG materials is substantially smaller than that for NC ones, see Tab. 5.1. Obviously it is a consequence of larger grain size in UFG materials. The second component with lifetime $\tau_2 \approx 300 - 400$ ps was attributed to microvoids at triple junctions, i.e. the intersections of the interfaces.

183

Table 5.1 Comparison of results obtained by PL spectroscopy on NC and UFG materials by different authors. Mean grain size, determined usually by XRD for NC and by TEM for UFG materials, is denoted by symbol d. In the case of NC materials prepared by GCM the compactization pressure p and the impurity concentration c_{imp} are given in the table. Timing resolution of PL spectrometer employed in each investigation is denoted as FWHM. The first component with lifetime τ_1 and relative intensity I_1 represents contribution of positrons trapped in vacancy-like defects, the second component (τ_2, I_2) comes from positrons trapped in microvoids. The long-lived component with lifetime τ_3 and relative intensity I_3 can be attributed to pick-off annihilation of o-Ps.
[a] Two long-lived o-Ps components were found in PL spectrum,
n.r. = not reported.

Material/ preparation technique	d [nm]	p [GPa]	c_{imp} [at.%]	FWHM [ps]	τ_1 [ps]	I_1 [%]	τ_2 [ps]	I_2 [%]	τ_3 [ns]	I_3 [%]	ref.
NC Cu/GCM	5-10	0.06	< 2	200-300	152±8	23±3	347±3	76±4	1.8±0.1	1.5±0.4	[10]
NC Cu/GCM	5-10	0.18	< 2	200-300	187±11	71±4	354±16	28±4	1.5±0.1	1.5±0.1	[10]
NC Cu/GCM	5-10	5.0	< 2	200-300	165±3	36±4	322±4	64±5	2.6±0.2	0.2±0.1	[10]
NC Pd/GCM	5-10	0.18	< 2	200-300	142±3	41±4	321±6	57±6	0.7±0.1	2.6±0.7	[10]
NC Fe/GCM	5-10	4.5	< 2	200-300	185±5	37±4	337±5	59±6	4.1±0.4	8.5±0.5	[10]
NC Cu/GCM	11-16	n.r.	10	200	150±5	15±4	300±15	84±5	1 − 2	0.7±0.3	[127]
NC Cu/GCM	22-26	n.r.	< 1.5	200	175±5	72±4	350±5	28±3	−	−	[127]
NC Fe/GCM	6	0.01	< 2	190-310	173±5	15±4	370±20	55±5	1.0±0.1 3.4 ± 0.2^{a}	17±4	[9]
NC Fe/GCM	6	0.06	< 2	190-310	187±4	47±5	360±20	47±5	1.3±0.4 4.0 ± 0.6^{a}	7±1	[9]
NC Fe/GCM	6	4.5	< 2	190-310	187±16	36±4	337±10	56±5	4.1±0.9	9±1	[9]
NC Fe/GCM	11-15	2.0	n.r.	225	193±3	48±1	417±9	45±1	0.99±0.04	7±1	[128]
NC Ni$_3$Fe/GCM	1-14	2.0	n.r.	225	181±1	43	427±2	55	2.20±0.05	2	[130]
UFG Cu/SPD	100-200		−	230	171±2	83±2	297±9	17±2	−	−	[131]
UFG Ni/SPD	100-200		−	230	161±1	88±1	330±9	12±1	−	−	[131]

As a very rough approximation we can assume that UFG material is composed with cubes of side d, where d represents grain size. Then length of the triple junctions is $12d$, while total surface of grain boundaries is $6d^2$. In NC materials the vacancy like defects are expected to be situated inside grain boundaries, while microvoids at the triple junctions. Typical grain size for NC and UFG materials is 10 nm and 100 nm, respectively. Typical ratio of relative intensity of positrons trapped in microvoids to that of positrons trapped in dislocations $I_2/I_1 \approx 1 - 2$ was found for NC materials. In the case of UFG materials, grain size d increases by a factor of 10. It means that the total length of the triple junctions increases by factor 10, while total surface of grain boundaries by factor 100. Thus the ratio I_2/I_1 should decrease by factor 10. The PL results for UFG Cu and Ni [131] shown in Tab. 5.1 exhibit the ratio I_2/I_1 from 0.1 to 0.2 in good agreement with the simple estimation given above. Hence, in principle microvoids in UFG materials may be situated also in triple points, similarly to NC ones. However, from the present data it is not possible to make decision where the microvoids are situated. As it will be shown in discussion of the results in the present work, see appendix J, microvoids in UFG materials are most probably situated inside

the grains.

Despite of the obvious similarity of PL results obtained for UFG and NC materials prepared by SPD and GCM, respectively, one has to take care in interpretation of these results in terms of defects present in these materials. Straightforward application of the interpretation made for NC materials prepared by GCM to UFG ones prepared by SPD is not justified and may be also incorrect due to following reasons:

1. Dislocations are unstable in NC materials prepared by GCM due to very small grain sizes (a few nanometer). On the other hand, large number of dislocations is expected to be present in UFG materials prepared by SPD. It was experimentally proved by TEM observations [7, 114, 125] as well as XRD study [132]. The studies revealed that dislocations are distributed strongly inhomogeneously; grain interiors almost free of dislocations are separated by distorted regions with high dislocation density. Thus contrary to NC prepared by GCM, substantial contribution of positrons trapped at dislocations is expected. It is well-known [67] that dislocation line itself represents only shallow positron trap. A positron trapped at a dislocation diffuses quickly and is finally trapped in a vacancy bound to the dislocation or in a jog of the dislocation, see section 2.8.3. Thus, final positron traps are vacancy-like defects like vacancy bound to dislocation or jog. As a consequence lifetime of positrons trapped at dislocations is only slightly lower than that for positrons trapped in vacancy, see section 2.8.3. It means that for UFG materials the first component with lifetime 160-170 ps, see Tab. 5.1 may represent contribution of positrons trapped at dislocations.

2. Defect density inside grains seems to be low for UFG materials prepared by SPD [7, 114]. At the same time the linear size of these grains is about 100 nm for UFG materials, i.e. about one order of magnitude greater than in NC ones, and it becomes comparable with the mean positron diffusion length, which is about 100-200 nm for well annealed metals. In connection with this a question arise whether some fraction of positrons annihilate in the grains from free, delocalized state. The work [131] cannot get correct answer to this question, because of bad resolution of PL spectrometer used, which makes determination of short free-positron component (lifetime below 100 ps) impossible. Recent investigations of Fe prepared by GCM performed by Segers et al. [128] revealed presence of the free-positron component in specimen with grain size 90-100 nm. It indicates that free-positron component might be found also in UFG materials prepared by SPD. In order to detect the free-positron component, if any, further investigations of UFG materials using high-resolution PL spectrometer is required.

   Note that if some defects with sufficient concentration are situated inside grains in UFG materials, then saturation trapping of positrons at defects inside grains and defects in distorted regions along grain boundaries may occur.

5.1.6 Thermal Stability of NC and UFG Materials

It is very important to have detailed information about thermal stability of NC and UFG materials. It means information regarding evolution of microstructure of as-prepared material with increasing temperature. Investigation of thermal stability is valuable from physical point of view as one obtains information about recovery of highly non-equilibrium microstructure. Moreover, such information is worthy also for future technical application of NC and UFG materials. The advantageous mechanical and other physical properties are connected with the NC or UFG structure, therefore, it is necessary to specify at what range of temperatures a material exhibits these properties.

PL spectroscopy can provide useful information about thermal evolution of microstructure with increasing temperature, as it detects changes of defect concentrations as well as changes of their size or spatial distributions. Several PL studies of thermal stability of NC materials prepared by GCM have been performed so far [10, 9, 127]. Würschum et al. [10] have studied thermal stability of NC Cu (grain size 5-10 nm) prepared by GCM. Obtained dependence of lifetimes of individual spectral components and their relative intensities on annealing temperature is shown in
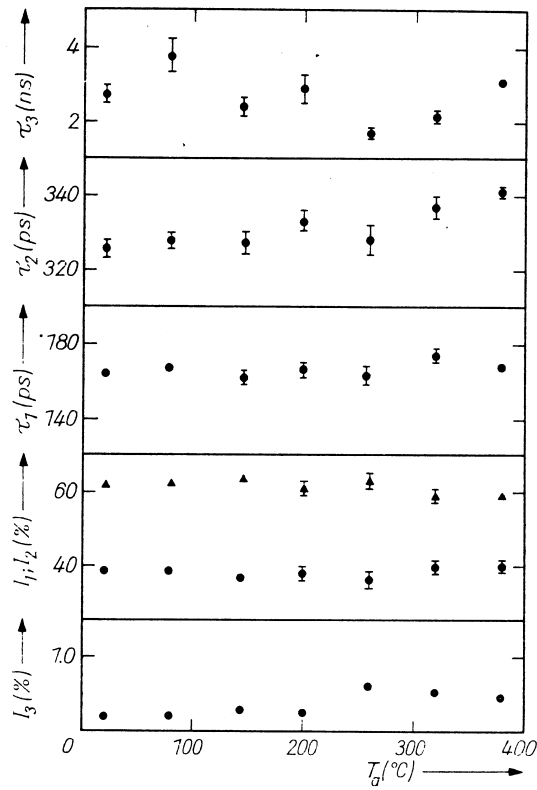
Figure 5.8 Lifetime components τ_i and relative intensities I_i (circles $- I_1, I_3$, triangles $- I_2$) measured on NC Cu with grain size 5–10 nm. The specimen was isochronally annealed at the temperature T_a and PL measurements were performed at room temperature [10].

Fig. 5.8. One can see in Fig. 5.8 that no significant changes occur up to 400 °C. It indicates that both the vacancy-sized defects (first component with lifetime τ_1) and the component belonging to microvoids (second component with lifetime τ_2) represent substantial structure component of microstructure of NC materials [9].

Thermal stability of NC materials is substantially influenced by gas impurities concentrations. It was proved by Eldrup et al. [127], who have studied thermal stability of NC Cu (grain size 10-25 nm) by means of PL spectroscopy. The specimens with total gas impurity concentration of about 10 at.% were compared with specimens of higher purity (gas impurity concentration below 1.5 at.%). Temperature dependence of positron lifetimes of spectral components and their relative intensities for the specimen with higher content of impurities is shown in Fig. 5.9. The long-lived o-Ps component is not included in Fig. 5.9. It is clear from Fig. 5.9 that the positron parameters remain unchanged up to 600 °C. At higher annealing temperatures additional component coming from delocalized positrons arises (lifetime τ_1). Relative intensity I_1 of this component increases with increasing annealing temperature, see Fig. 5.9. On the other hand, relative intensity I_3 of the component attributed to microvoids decreases, it is accompanied by increase of lifetime τ_3 of this component.

Isochronal annealing of the NC Cu specimens with improved purity (gas impurity concentration < 1.5 at.%) have resulted in substantially different results shown in Fig. 5.10. Change of positron parameters was found already at 200 °C, see Fig. 5.10. Moreover, the relative intensity I_3 of the microvoids contribution increases above 200 °C, while its lifetime τ_3 decreases, see Fig. 5.10. Hence, the component with lifetime τ_3, which comes from the microvoids exhibits for the specimen
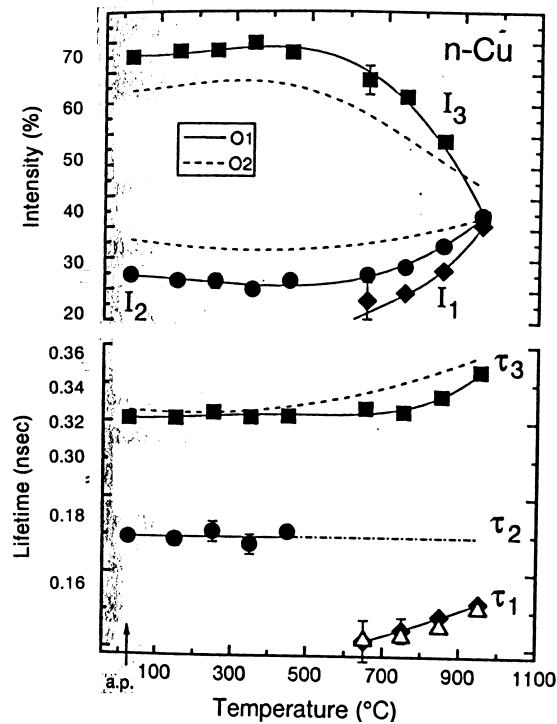
186

Figure 5.9 Temperature dependence of positron lifetime parameters for NC Cu specimens with grain size 11-16 nm and gas impurity concentration of about 10 at.% [127]. The specimens were prepared by GCM. The lifetime τ_2 was fixed at 147 ps above 650 °C (dash-dotted line). The open triangles are trapping model calculations of τ_1.

with higher purity even opposite behavior than for the previous one with higher impurity content. Dependence of grain size on annealing temperature, determined in Ref. [127], for the specimen with higher purity is plotted in Fig. 5.11. Clearly, grain growth takes place above 200 °C. Increase of the intensity I_3 and thereby increase of the ratio I_3/I_2 is, therefore, surprising as one would expect opposite behavior due to increasing grain size. The increase of relative intensity I_3 of the component coming from microvoids was not satisfactorily explained yet.

No PL study of thermal stability of UFG materials prepared by SPD has been performed so far. The SPD techniques produce UFG materials, which are free of gas impurities. Thus, contrary to NC materials prepared by GCM, thermal stability of UFG ones prepared by SPD is not influenced by gas impurity concentration. Also this fact makes the comparison of thermal evolution of defect components in UFG and NC materials highly interesting.

Investigation of thermal stability of UFG Cu and Ni (grain size about 100 nm) was performed by Islamgaliev et al. [114] using TEM, XRD, DSC, electrical resistivity and microharness measurement. It was found that heat release, relaxation of elastic strains and recovery of electrical resistance precede to grain growth and are caused mainly by relaxation of dislocations in grain boundaries. Thus, some rearrangement of defects inside the distorted regions along grain boundaries probably occurs. Another investigation of UFG Cu (grain size 100 nm) was performed by Amikharnov et al. [125] by means of TEM. Reduction in azimuthal spreading of spots observed on electron diffraction patterns was found prior to the onset of grain growth. It testifies to a partial relaxation of the non-equilibrium defect structure of samples. Observed decrease in the amount of bend contours and more homogeneous diffraction contrast inside the grains [125] represent an
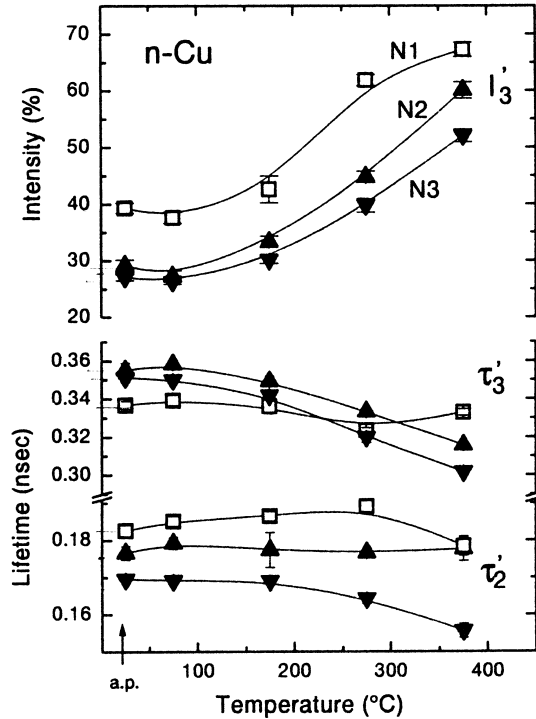
Figure 5.10 Temperature dependence of positron lifetime parameters for NC Cu specimens with grain size 22 nm (N1), 26 nm (N2) and 60 nm (N3) prepared by GCM [127]. Gas impurity concentration was about 1.5 at.%.

additional evidence for this relaxation. After heating to 220 °C an abnormal grain growth, leading to a binomial grain size distribution, was noticed [125]. Grains of about 1.5 μm size are formed within UFG deformed matrix. Another specific feature of the structure of the sample heated to 220 °C was appearance of annealing twins in the grains, which have undergone grain growth process. During further heating to 270 and 300 °C the increase in both the mean grain size of coarse grains and their total volume fraction was observed [125].

5.2 The Aim of The Present Work

Microstructure and thermal stability UFG Cu and Ni prepared by SPD were studied in the present work. The UFG materials were chosen for the following reasons:

1. Contrary to NC materials, relatively little is known about defects in UFG materials prepared by SPD. On the other hand, microstructure of the UFG materials was studied by TEM [7, 114, 125] and XRD [132]. Results obtained by these methods represents valuable background knowledge for interpretation of PL results. Correlation of PL spectroscopy, TEM and XRD measurements allows for correct interpretation of lifetime components distinguished in PL spectra.

2. It is possible that fraction of positrons which annihilate from free state is non-negligible for UFG materials. In such a case lifetime and relative intensity of the components coming from free positrons can be properly determined only using PL spectrometer with high enough timing resolution (well below 200 ps). Thus, benefit of high timing resolution (150 ps FWHM) of
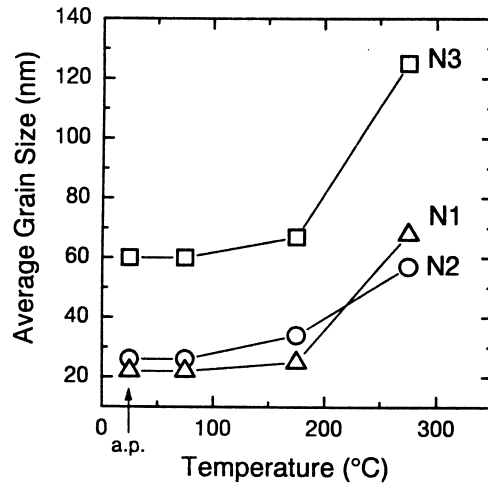
188

Figure 5.11 The mean grain size as a function of annealing temperature for the NC Cu specimens prepared by GCM [127]. Initial grain sizes were 22 nm, 26 nm and 60 nm for N1, N2 and N3 specimens, respectively. Gas impurity concentration was about 1.5 at.%.

our PL spectrometer is fully exploited. Moreover, when free-positron component is present in PL spectrum, then it is possible to determine defect densities using a model of positron trapping, see section 2.7. Defect densities obtained by PL spectroscopy can be compared with those determined by other independent methods (TEM, XRD). The comparison then serves as strong indication of reliability of trapping model used in evaluation of the defect densities. When the proper model of positron trapping in UFG materials is developed, then the determined densities of defects represent valuable independent characteristics of UFG materials.

3. Contrary to NC materials, UFG specimens contain no gas impurities nor residual porosity. Thus, thermal stability of UFG materials is not influenced by gas impurity concentration and residual porosity, which have significant impact to thermal stability of NC materials prepared by GCM [127].

Two types of UFG Cu specimens prepared under different conditions and one UFG Ni specimen were studied in the present work. The investigated materials and parameters of their preparation are listed in Tab. 5.2.

The specimens were prepared by R.K. Islamgaliev in the Institute of Physics of Advanced Materials, Ufa, Russia. Firstly microstructure of as-prepared specimens were studied by means of PL spectroscopy and TEM. Main attention was focused on determination of defects types present in specimen as well as their densities and spatial distributions. In order to do that a model of positron trapping in UFG materials, which takes into account strongly non-uniform spatial defect distribution in UFG materials, was developed. Subsequently, the specimens were subjected to isochronal annealing and evolution of microstructure with increasing temperature was investigated. The purposes of the present work on the UFG specimens can be summarized into following items:

1. It is expected that correlation of PL spectroscopy and TEM bring detailed information about microstructure of the UFG specimens. In particular, each exponential component in

Table 5.2 The UFG specimens prepared by SPD studied in the present work. The specimens were prepared by R.K. Islamgaliev in the Institute of Physics of Advanced Materials, Ufa, Russia. The symbol e denotes total logarithmic deformation in torsion $e = \ln \phi\, r/l$, where ϕ, r and l designate the torsional angle in radians as well as the radius and the thickness of the specimen. High pressure applied on specimens simultaneously with the torsion deformation is denoted as p. The mean grain size d, determined by TEM as well as the coherent domain size a obtained by XRD are also included in the table. The year of preparation of the specimens is given in the last column of the table.

denotation	material	e [%]	p [GPa]	d [nm]	a [nm]	purity [%]	size [mm]	year of preparation
UFG-Cu1	Cu	≈ 7	6	100	50	99.99	ø 11×0.2	1994
UFG-Cu2	Cu	≈ 7	3	150	70	99.99	ø 15×0.3	1999
UFG-Ni	Ni	≈ 7	6	100	70	99.98	ø 11×0.2	1996

PL spectrum coming from trapped positrons will be properly attributed to corresponding type of defects.

2. Concentration of each type of defect will be calculated from the experimental PL spectra.

3. Present knowledge about microstructure of UFG materials indicates that assumptions of single trapping model (STM) may not be satisfied in these materials. Therefore, validity of STM on the UFG specimens will be tested. In the case that STM cannot be applied for the UFG materials, a new model which describes properly behavior of positrons in the UFG specimens will be developed.

4. Evolution of microstructure of the UFG specimens with increasing temperature will be studied by PL spectroscopy correlated with TEM. In particular, information about evolution of defect densities will be obtained.

5. Microstructure and its thermal evolution for the two UFG Cu specimens prepared with various pressures applied during torsion deformation will be compared.

6. As-prepared state as well as its thermal evolution for UFG Cu and Ni will be compared.

7. Types of defects in UFG materials will be compared with those in NC ones.

5.3 The Results Obtained in The Present Work

Investigation of thermal stability of the UFG-Cu1 specimen, see Tab. 5.2, is described in the appendix I. Strongly non-uniform spatial defect distribution in the UFG Cu specimen does not allow for application of the simple trapping model (STM), see Appendix I. Therefore, modified trapping model (MTM) developed in the present work, see also section 4.2 and appendix F, was used for interpretation of experimental PL spectra. Application of the MTM to interpretation of PL spectra for the UFG-Cu1 specimen is described in the appendix I.

Microstructure and its thermal evolution for UFG-Cu2 specimen, i.e. the specimen prepared with about two times lower hydrostatic pressure applied during torsion deformation than UFG-Cu1, see Tab. 5.2, were studied as the next part of my work. The investigation of UFG-Cu2 specimen is described in the appendix J. Similarly to the UFG-Cu1 specimen STM cannot be used for interpretation of PL results obtained on UFG-Cu2 specimen due to inhomogeneous spatial

defect distribution, see appendix J. Therefore, a model for proper description of positron behavior in UFG materials was developed in the present work. This model represents an improvement with respect to MTM. Contrary to MTM, not only inhomogeneous spatial defect distribution in specimen together with non negligible volume fraction of distorted regions with high defect density, but also depletion of stochastic positron density near distorted regions, inside which positrons are trapped, were taken into account. Time dependent positron density in specimen is obtained directly by solving the diffusion equation for delocalized positrons. Therefore, the model is called diffusion trapping model (DTM). Full description of the DTM and its application to UFG-Cu2 specimen is given in the appendix J.

5.4 Comparison of UFG-Cu1 and UFG-Cu2 Specimens

The specimen UFG-Cu1 studied in appendix I is compared with UFG-Cu2 specimen investigated in appendix J. The specimens differ by hydrostatic pressure applied during preparation. Two times lower pressure was used in preparation of UFG-Cu2 specimen than UFG-Cu1 one, see Tab. 5.2. The lower pressure resulted in larger mean grain size in the specimen UFG-Cu2 (150 nm) than in the UFG-Cu1 (100 nm), see Tab. 5.2. In addition, the UFG-Cu1 specimen was prepared 5 years before the UFG-Cu2, see Tab. 5.2. It means that contrary to the UFG-Cu2, the UFG-Cu1 specimen was prior to measurement aged for about 5 years at room temperature.

Dependence of the positron mean lifetime $\bar{\tau}$ on annealing temperature is shown in Fig. 5.12. One can see in Fig. 5.12 that $\bar{\tau}$ for the UFG-Cu1 specimen remains roughly constant up to
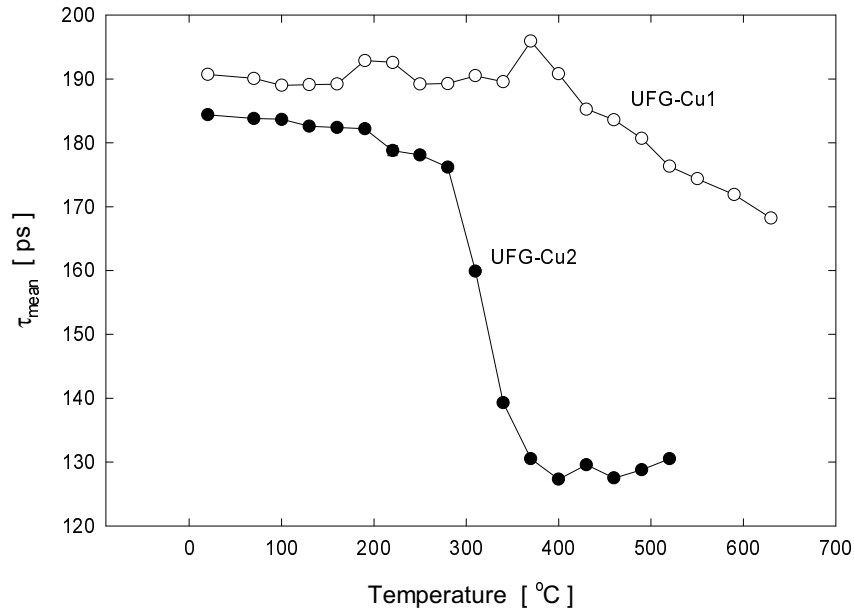

Figure 5.12 Temperature dependence of the mean lifetime for UFG-Cu1 and UFG-Cu2 specimens.

~ 370 °C and then gradually decreases. On the other hand, slight decrease of $\bar{\tau}$ starts already at 220 °C for the UFG-Cu2 and it is followed by abrupt decrease of $\bar{\tau}$ between 300 and 400 °C, see Fig. 5.12.

PL spectra for the UFG-Cu1 specimen are well fitted by three exponential components with lifetimes τ_1, τ_2 and τ_3. The shortest component with lifetime τ_1 represents contribution of free

positrons. The second component with lifetime τ_2 comes from positrons trapped at dislocation inside the distorted regions and the last component with lifetime τ_3 can be attributed to positrons trapped in microvoids, see appendix I. In the case of the UFG-Cu2 specimen all positrons annihilate from trapped state at dislocation and in microvoids up to 190 °C, see appendix J, i.e. PL spectra are well fitted by two exponential components with lifetimes τ_2 and τ_3. Above 190 °C free positron component with lifetime τ_1 appears in PL spectra, see appendix J.

Temperature dependencies of lifetimes τ_2 and τ_3 of trapped positrons for UFG-Cu1 and UFG-Cu2 specimens are shown in Fig. 5.13. Clearly, the lifetime τ_2 is the same for both the specimens.
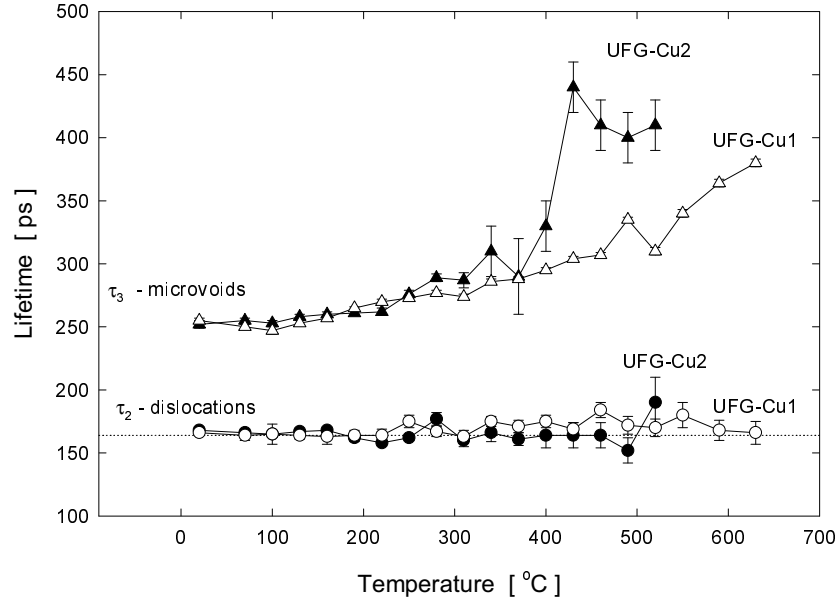

Figure 5.13 Lifetimes of positrons trapped at defects as a function of annealing temperature for UFG-Cu1 and UFG-Cu2 specimens.

The lifetime τ_2 does not exhibit any change except of fluctuation around the mean value of 164 ps (indicated by dotted line), see appendix I, J. The lifetime τ_3 of positrons trapped in microvoids exhibits moderated increase with increasing temperature up to 400 °C, see Fig. 5.13. Above 400 °C τ_3 exhibits rapid increase for both the specimens up to about 400 ps. In the case of UFG-Cu2 the increase of τ_3 occurs abruptly in relatively narrow temperature interval 400 − 450 °C, and then τ_3 remains constant, see Fig. 5.12. On the other hand, τ_3 increases gradually towards 400 °C in the case of UFG-Cu1, see Fig. 5.12.

Dependencies of relative intensities I_2 and I_3 of the components belonging to positrons trapped at dislocations and in microvoids, respectively, on annealing temperature are plotted in Fig. 5.14. One can see in the figure that relative intensity I_2 of dislocation component is about 15 % lower for as-prepared UFG-Cu1 than for UFG-Cu2. At the same time relative intensity I_3 of positrons trapped in microvoids is about 15% higher for as-prepared UFG-Cu1 than for UFG-Cu2. It may indicate higher number of microvoids in UFG-Cu1 specimen then UFG-Cu2, which is probably due to two-times higher hydrostatic pressure used in preparation of UFG-Cu1 specimens, see Tab. 5.2. However, as it will be shown further (Fig. 5.24) concentration of microvoids calculated using DTM is not lower in UFG-Cu2 specimen. Thus, the difference between relative intensities I_2, I_3 mentioned above is most probably due to lower dislocation density in as-prepared UFG-Cu1. Moreover, weak free positron component is present in UFG-Cu1, while all positrons annihilated
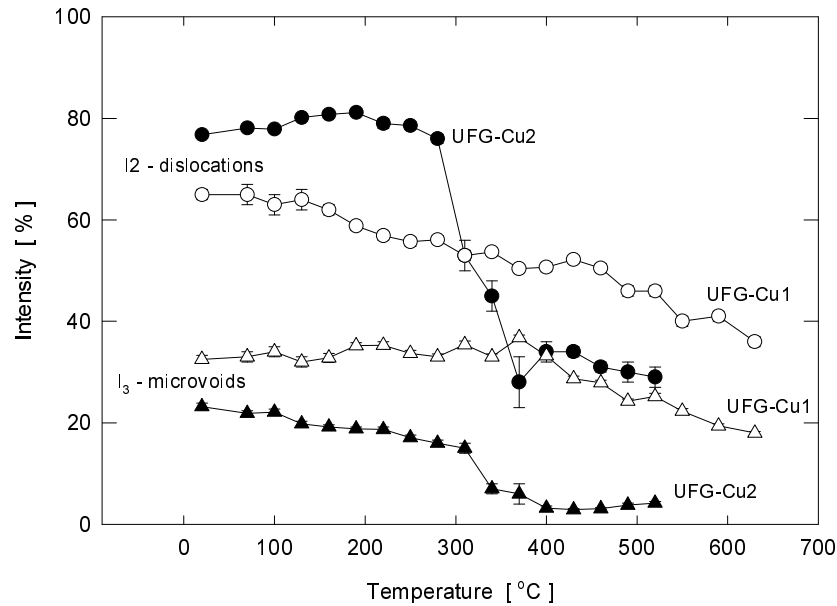
Figure 5.14 Temperature dependence of the relative intensities of positrons trapped at defects for UFG-Cu1 and UFG-Cu2 specimens.

from trapped state in UFG-Cu2. It may be a consequence of some partial recovery of UFG-Cu1 specimen due to ageing at room temperature. As one can see in Tab. 5.2 the time interval from preparation of the specimens to PL measurements is 5 years for UFG-Cu1 (measurement was performed in 1999) and only 1 year for UFG-Cu2 specimen (measurement was performed in 2000). Long time aging of UFG specimens even at room temperature may cause some changes of as-prepared microstructure towards more stable configuration [133]. For example some isolated defect-free grains may appear in the aged specimens. It would lead to presence of free positron component in PL spectra due to positrons, which annihilate inside the isolated defect-free grains. Clearly, additional investigations are needed in order to clarify influence of thermal aging to microstructure of UFG specimens.

In the case of UFG-Cu2, the relative intensity I_2 remains approximately constant up to 300 °C, then it exhibits abrupt decrease almost by 60 % between 300 and 400 °C, see Fig. 5.14. Finally, I_2 remains again approximately constant above 400 °C, see Fig. 5.14. On the other hand, I_2 starts to decrease at 190 °C and continuously gradually decreases in whole measured temperature range, i.e. up to 630 °C for UFG-Cu1. Final value of I_2 for UFG-Cu1 annealed at 630 °C is 36±1 %, which is close to the plateau of I_2 at about 30 % for UFG-Cu2.

In the case of UFG-Cu2, the relative intensity I_3 of positrons trapped in microvoids decreases gradually in temperature range between 100 and 300 °C. The decrease is followed by radical drop between 300 and 400 °C. Above 400 °C I_3 remains approximately constant. In the case of UFG-Cu1, the relative intensity I_3 remains unchanged up to about 350 °C and exhibits even slight increase. Above 350 °C I_3 radically decreases.

The DTM described in details in appendix J was applied to the studied specimens. Application of DTM on UFG-Cu2 specimens is described in appendix J. The results obtained using DTM on UFG-Cu1 specimens and their comparison with those for UFG-Cu2 will be given in the following text.

Temperature dependence of the volume fraction η of distorted regions is shown in Fig. 5.15.

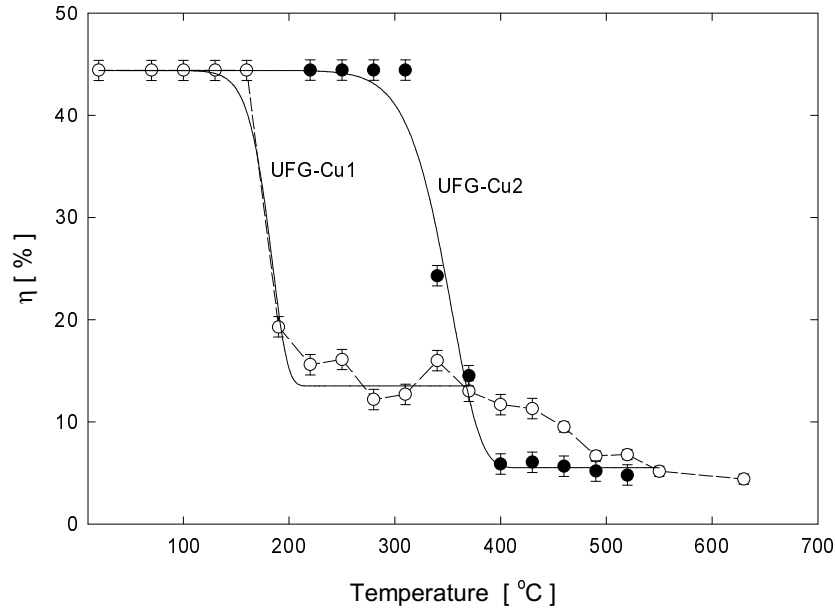One can see in the figure that initial value of η is the same for both the specimens. However, it

Figure 5.15 Temperature dependence of the volume fraction η of the distorted regions obtained using the DTM for UFG-Cu1 and UFG-Cu2 specimens. The solid lines represent fit of the temperature dependence of η by procedure described in appendix J, which allows for determination of the activation energy of the primary recrystallization.

should be pointed out that in the case of UFG-Cu2 specimen, it is possible to determine η only for annealing temperatures of 220 °C and higher, when contribution of free positrons is present in PL spectra. It is not clear, whether the volume fraction η remains constant also below 220 °C (shown by dotted line in Fig. 5.15) or becomes higher. The volume fraction η rapidly decreases from 160 to 220 °C in the case of UFG-Cu1 specimen. After this radical drop η gradually decreases with substantially smaller slope up to 550 °C. On the other hand, η remains constant up to 310 °C for UFG-Cu2 and then abruptly decreases by about 40 % between 310 and 400 °C. At higher annealing temperatures above 400 °C, η remains constant, see Fig. 5.15. Note that effective heating was 1 °C / min and was identical for both the specimens, see appendix I, J. Obviously the shape of temperature dependence of η is similar for both the specimens. Nevertheless, there is a temperature shift of radical drop of η towards lower annealing temperatures for UFG-Cu1. It means that there is radical diminution of the distorted regions between 160 and 220 °C in the case of UFG-Cu1. It is most probably that in similar way as in UFG-Cu2 at higher temperatures, see appendix J, deformed matrix is transformed into defect-free recrystallized grains. However, contrary to UFG-Cu2, the abrupt decrease of η stops at about 20 % and is followed by moderate gradual decrease of η. It seems to indicate that only some part of the UFG-Cu1 specimen was transformed into the defect-free recrystallized grains. Thus, at 200 °C probably the recrystallized grains and practically unchanged deformed matrix coexist in the UFG-Cu1 specimens. Another possibility is that linear size of the recrystallized grains in UFG-Cu1 specimen is substantially lower compared to UFG-Cu2, i.e. there is significant contribution from positrons trapped at grain boundaries. Moreover, as one can see in Fig. 5.14, there is no decrease of the relative intensity I_3 up to 370 °C in UFG-Cu1. Hence, in the case of UFG-Cu1, only dislocation density decreases during the abrupt drop of η mentioned above, while number of microvoids does not change. We

194

have found, see appendix J, that in the case of UFG-Cu2 specimens, only very large microvoids can survive in recrystallized grains and the concentration of microvoids in the recrystallized grains is substantially smaller than that inside the deformed matrix. On the other hand, in the case of UFG-Cu1, the microvoids remains also in recrystallized grains formed below 370 °C practically with unchanged concentration. Substantial decrease of the concentration of microvoids does not occur before about 370 °C, see Fig. 5.14. Indeed, TEM measurements of UFG-Cu1 annealed at 630 °C have revealed a number of microvoids present in recrystallized grains, see Fig. 5.16. Some rare microvoids were found also in recrystallized grains in UFG-Cu2 specimen, see Fig. 9 in
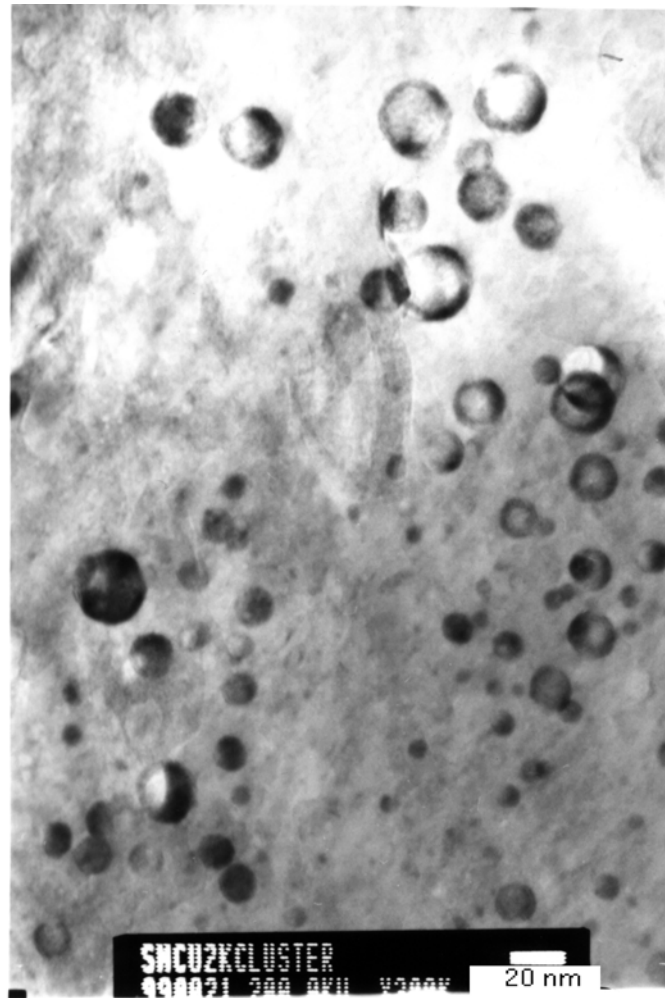

Figure 5.16 Bright field TEM image of UFG-Cu1 specimen annealed at 630 °C. The microvoids are visible inside the recrystallized grain.

appendix J and discussion therein.

Temperature dependence of the mean linear size of non-distorted regions $2R$ obtained using DTM is shown in Fig. 5.17. As it was already discussed in appendix J $2R$ is closely related to dislocation density and corresponds roughly to the mean coherent size determined by XRD. It is known that the mean grain size determined by TEM is somehow higher than $2R$. For example $2R$ obtained from PL spectroscopy as well as the mean coherent size obtained by XRD are two-times smaller than the mean grain size determined by TEM for as-prepared state of UFG Cu
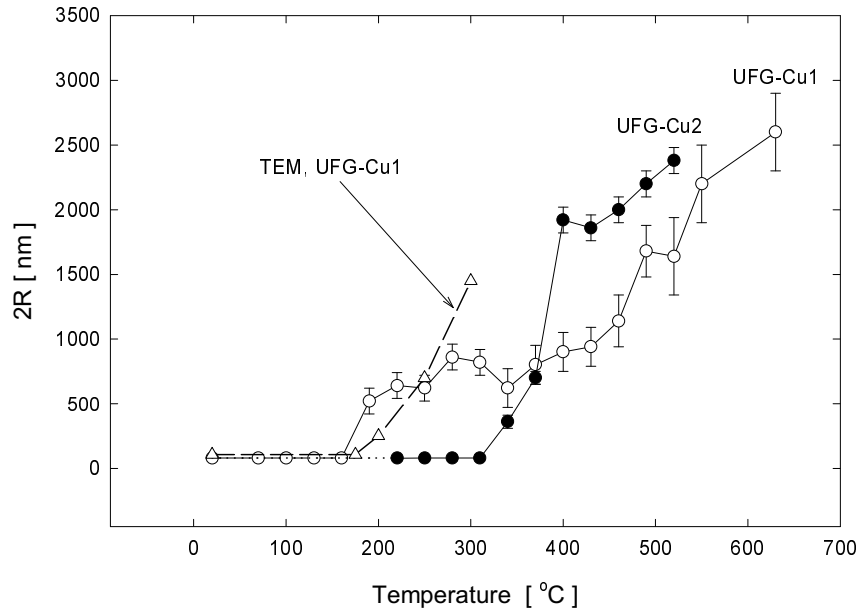
Figure 5.17 Temperature dependence of the mean linear size $2R$ of the non-distorted regions obtained using the DTM for UFG-Cu1 and UFG-Cu2 specimens. The mean grain size determined by TEM on the UFG-Cu1 specimen is shown in the figure by triangles connected by the dashed line.

specimens, see Tab. 5.2. This difference is caused by non identical definition of the mean size of coherent domain (the mean linear size of the non distorted regions $2R$), obtained by XRD and PL spectroscopy, and the mean grain size, determined by TEM. The former is directly connected with radical change of dislocation density (two orders of magnitude) inside the non distorted regions (coherent domains) and the distorted ones, while the latter reflects rather various contrast in TEM image inside grains and grain boundaries. More detailed explanation of the difference can be found in appendix J. Schematic two-dimensional description of as-prepared state of UFG metal is shown in Fig. 5.18 with explanation of the above mentioned quantities. Clearly, the difference between $2R$ and grain size obtained by TEM decreases with annealing temperature and, therefore, it makes sense to strictly distinguish between the mean coherent size (or the mean size of the non distorted regions $2R$) and the mean grain size determined by TEM only for as-prepared state and very low annealing temperatures.

We recall that in the case of UFG-Cu2, R can be determined only for annealing temperature higher than 200 °C, when free positrons component is present in PL spectra. Initial linear size of non-distorted regions of about 80 nm was determined for both the specimens, see Fig. 5.17. Similarly to η, an increase of R occurs at lower temperatures for UFG-Cu1 than UFG-Cu2. In the case of UFG-Cu1, $2R$ increases from 80 to about 500 nm in temperature interval from 160 to 220 °C, see Fig. 5.17. After this increase $2R$ remains virtually constant and from 370 °C it starts to increase remarkably again. Finally at 630 °C, the mean linear size $2R$ becomes 2.5 μm, see Fig. 5.17. On the other hand, the increase of $2R$, i.e. grain growth, is shifted to higher annealing temperatures for UFG-Cu2. In this specimen $2R$ remains constant (at 80 nm) up to 310 °C and then abruptly increases during primary recrystallization to about 2 μm at 400 °C, see Fig. 5.17. At higher temperatures R still gradually increases with the same slope as for UFG-Cu1. Thus, behavior of R indicates that recrystallized grains appear in UFG-Cu1 during temperature interval 190-220 °C, which is reflected also by decrease of η discussed above. Either linear size of the re-
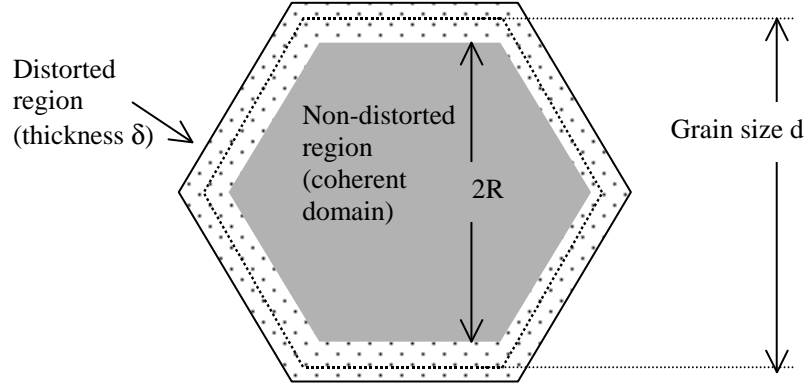
Figure 5.18 Schematic description of a grain of UFG material. The linear size of the non-distorted region $2R$, the grain size d and the thickness of the distorted region δ are indicated.

crystallized grains is only about 500 nm or recrystallized grains coexist with unchanged deformed matrix in UFG-Cu1 at 220 °C. Further increase of grain size occurs from 370 °C and is accomplished also by remarkable decrease of concentration of microvoids, see Fig. 5.17. On the other hand, noticeable increase of R takes place only during primary recrystallization at temperature interval 300-400 °C in UFG-Cu2, see Fig. 5.17. The mean grain size in both the recrystallized specimens still increases at high annealing temperatures (above 450 °C), see Fig. 5.17.

The mean grain size determined by TEM for UFG-Cu1 [114] is also included in Fig. 5.17 as a function of annealing temperature. Relatively good agreement of the mean grain size obtained by TEM and $2R$, see Fig. 5.17, strongly supports the interpretation given above and serves also as valuable independent evidence for validity of DTM for the studied specimens.

It is possible to determine activation energy Q of the primary recrystallization from temperature dependence of η, see Fig. 5.14. We used the same procedure as explained in appendix J. The temperature dependencies of η, obtained by fitting the eq. (39) in the appendix J to experimental data for UFG-Cu1 and UFG-Cu2 specimens, are plotted by the smooth solid lines in Fig. 5.14. One can see from Fig. 5.14 that the theoretical fitted curves exhibit relatively good agreement with the experimental points. The activation energies determined from the fits are $Q = 91 \pm 10 \; \mathrm{kJ\,mol^{-1}}$ and $Q = 96 \pm 10 \; \mathrm{kJ\,mol^{-1}}$ for UFG-Cu1 and UFG-Cu2, respectively. Thus, the activation energy of the process responsible for decrease of η between 190 and 250 °C in UFG-Cu1 agrees well with that for decrease of η between 300 and 400 °C in UFG-Cu2, see Fig. 5.14. It is well known from literature that the activation energy $Q = 110 \; \mathrm{kJ\,mol^{-1}}$ corresponds to movement of equilibrium GBs in Cu [134]. Thus, it is most probable that primary recrystallization takes place between 190 and 220 °C in UFG-Cu1 and between 300 and 400 °C in UFG-Cu2. In the case of UFG-Cu1 the recrystallization is not complete and/or linear size of recrystallized grains is about 0.5 μm, i.e. remarkably smaller than in UFG-Cu2 (~ 2 μm), see Fig. 5.17.

Temperature dependence of the positron trapping rate to dislocations K_D, see appendix J for detailed discussion, obtained using DTM is shown in Fig. 5.19. One can see in Fig. 5.19 that K_D abruptly increases in temperature interval 160–220 °C and 370–400 °C for UFG-Cu1 and UFG-Cu2, respectively. As was discussed in appendix J this radical increase of the trapping rate K_D is direct indication of change in type of the trapping centers. Substantially higher value of K_D corresponds most probably to positron trapping in equilibrium high-angle grain boundaries among
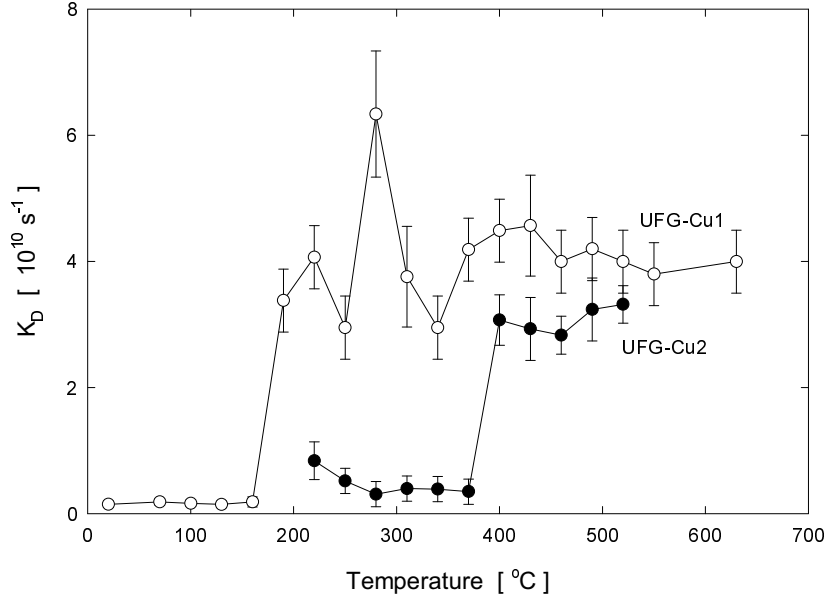
Figure 5.19 Temperature dependence of the trapping rate to dislocations, K_D, obtained from the DTM for UFG-Cu1 and UFG-Cu2 specimens. After the primary recrystallization positrons are trapped at equilibrium GBs, which is reflected by abrupt increase of K_D.

recrystallized grains, see discussion in appendix J. Hence, in agreement with the interpretation given above, the sharp increase of K_D corresponds to primary recrystallization.

The trapping rate K_D is directly connected with dislocation density inside the distorted regions, see appendix I, J. Thus, it is possible to determine the mean dislocation density in the specimens, see eq. (38) in appendix J. The mean dislocation density ϱ_D calculated using the procedure described in appendix J is shown in Fig. 5.20 as a function of annealing temperature for UFG-Cu1 and UFG-Cu2. Note that ϱ_D can be calculated only when free positron component is present in PL spectra, i.e. for UFG-Cu2 above 200 °C. Moreover, after primary recrystallization the component with lifetime τ_2 comes not only from positrons trapped at dislocations but contains also significant contribution of positrons trapped at grain boundaries. It is clearly visible as sharp increase of K_D. At high annealing temperatures dislocation density tends to $\sim 10^{12}$ m^{-2}, which is lower sensitivity limit of PL spectroscopy [135], and thereby contribution of positrons trapped at grain boundaries dominates. For the above reasons it is possible to determine ϱ_D only in UFG specimen prior to primary recrystallization, it means below 200 °C and 400 °C for UFG-Cu1 and UFG-Cu2, respectively.

One can see in Fig. 5.20 that the mean dislocation density in as-prepared UFG-Cu1 is $\varrho_D \approx 10^{14}$ m^{-2}. It is in good agreement with ϱ_D determined using TEM and XRD in as-prepared UFG-Cu1 [114]. Estimation of ϱ_D for as-prepared UFG-Cu2 given in appendix J as well as TEM investigations of this specimen lead to the same value. Pronounced decrease of ϱ_D during the grain growth in UFG-Cu2 is clearly visible in Fig. 5.20.

Application of MTM on UFG-Cu1 specimen described in appendix I gave for as-prepared state and low annealing temperatures (below 200 °C, i.e. primary recrystallization) also the mean dislocation density $\varrho_D \approx 10^{14}$ m^{-2}. It implies that MTM is very simple but reasonable approximation of positron behavior in UFG materials. At higher annealing temperatures (above 220 °C) positrons trapped at grain boundaries significantly contributes to the second component
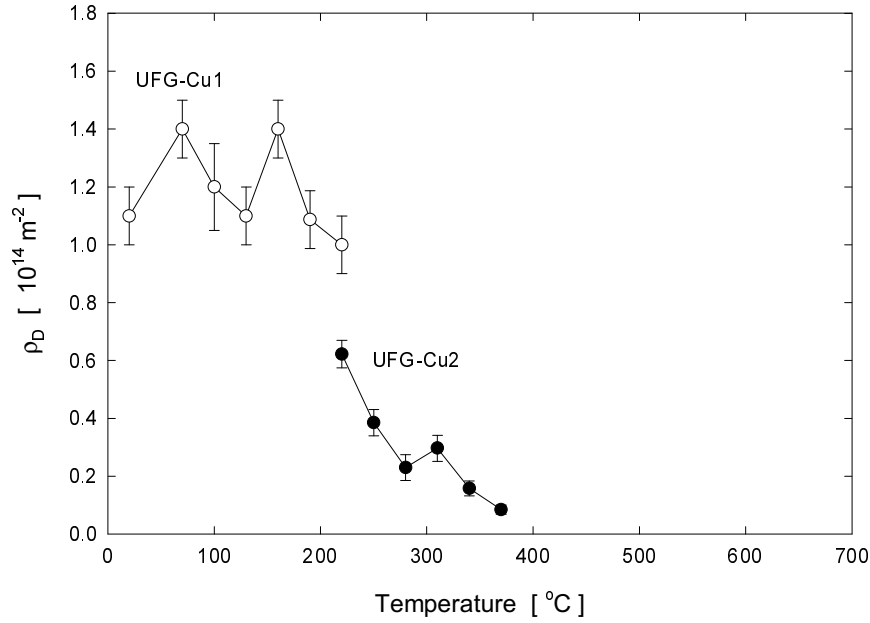
Figure 5.20 The mean dislocation density ϱ_D determined using the DTM as a function of annealing temperature for UFG-Cu1 and UFG-Cu2. The dislocation density can be determined only in non-recrystallized specimen and in the temperature range when free positron component is present in PL spectra, see text.

with lifetime τ_2 and therefore ϱ_D determined by MTM (see appendix I) is higher than actual mean dislocation density in specimen.

The positron trapping rate K_v to microvoids obtained using DTM is plotted in Fig. 5.21 as a function of annealing temperature. As there is increase of the lifetime τ_3 with annealing temperature, see Fig. 5.13, the specific positron trapping rate to microvoids also grows with increasing annealing temperature. Theoretical calculations of positron lifetime as a function of number n of vacancies from which the cluster consists were performed in appendix J. Using the results of these calculations it is possible to determine free volume of microvoids (in units of monovacancy free volume) and thereby also linear size (diameter) of microvoids as a function of annealing temperature, see appendix J, Fig. 12. The dependence of free volume n of microvoids on annealing temperature for UFG-Cu1 and UFG-Cu2 is shown in Fig. 5.22. As was already mentioned in appendix J it is reasonable to assume that there is some size distribution of microvoids in UFG Cu specimens. The free volume n obtained from the measured lifetime τ_3 corresponds to the center-of-mass of this distribution. One can see in Fig. 5.22 that there is gradual growth of n towards higher values. The only difference between UFG-Cu1 and UFG-Cu2 is abrupt increase of n between 370 and 430 °C for UFG-Cu2, see Fig. 5.22. The increase of n with annealing temperature reflects the fact that larger microvoids are more stable, i.e. the smallest microvoids are annealed out firstly. The abrupt increase of n occurs in UFG-Cu2 during final stage of primary recrystallization, see Fig. 5.22. It means that only the largest microvoids can survive in recrystallized material.

Using the trapping rate K_v and the results of theoretical calculations make possible to determine the mean concentration of microvoids c_v as it is explained in appendix J. Temperature dependence of c_v for UFG-Cu1 and UFG-Cu2 is shown in Fig. 5.23. The concentration of microvoids in UFG-Cu2 can be determined only above 200 °C when free positron component appeared in PL spectra. As one can see in Fig. 5.23, initial concentration c_v as well as final concentration
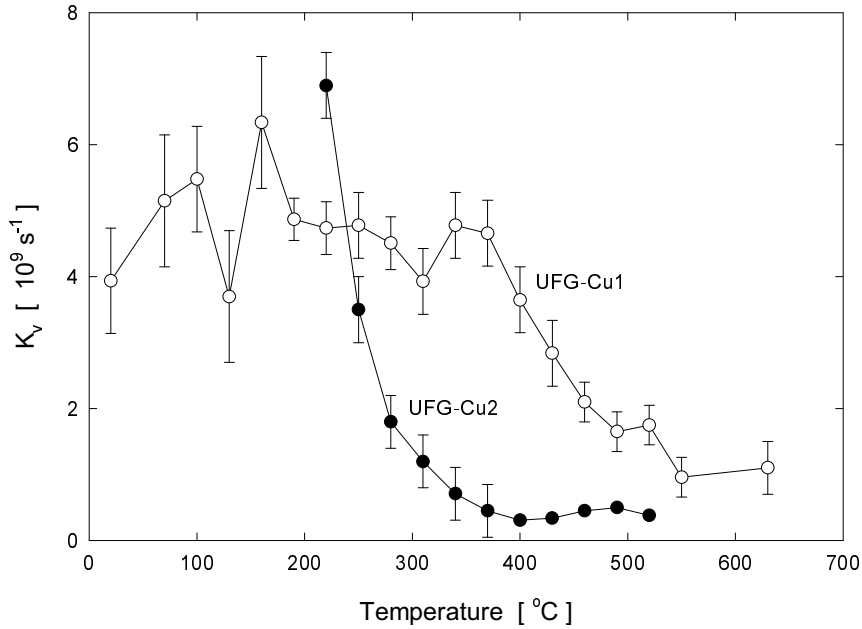
Figure 5.21   The positron trapping rate for the microvoids, K_v, determined for UFG-Cu1 and UFG-Cu2 from the DTM plotted as a function of annealing temperature.

(in specimens annealed at temperature above 500 °C) are similar for UFG-Cu1 and UFG-Cu2. However, the decrease of c_v is shifted to substantially higher temperatures for UFG-Cu1 compared to UFG-Cu2. In the case of UFG-Cu2, c_v decreases mainly during the abnormal grain growth (200-300 °C), see Fig. 5.23, it is followed by only moderate decrease, which takes place during primary recrystallization (300-400 °C). On the other hand, recrystallization in UFG-Cu1 specimen (190-220 °C) does not lead to noticeable decrease of c_v, see Fig. 5.23. The main decrease of c_v in UFG-Cu1 occurs between 400 and 500 °C, i.e. at significantly higher annealing temperatures than in UFG-Cu2.

It is interesting to compare the concentration of microvoids c_v in UFG-Cu1 determined by DTM (Fig. 5.23) with that determined using MTM (appendix I, Fig. 2b). The mean concentrations of microvoids c_v obtained on UFG-Cu1 using both the models are plotted in Fig. 5.24.   One can see in the figure that c_v determined by both the models exhibits similar trend with annealing temperature, however absolute values of c_v obtained by MTM are somehow higher than those determined by DTM. The reasonable agreement of DTM and MTM results for c_v gives a strong evidence that MTM represents very simple but realistic approach for positron behavior in UFG materials.

We conclude that there is remarkable difference between UFG-Cu1 and UFG-Cu2 specimens. The difference is caused by both or one of the two following factors: (i) UFG-Cu1 specimen was prepared with two times higher hydrostatic pressure than UFG-Cu2, which results in smaller grain size in UFG-Cu1 (ii) contrary to UFG-Cu2, UFG-Cu1 specimen was aged for about 5 years at room temperature before PL measurement. Isolated recrystallized grains are most probably present already in as-prepared UFG-Cu1 specimen (likely due to prior ageing at room temperature), while the abnormal grain growth takes place from 190 to 300 °C in UFG-Cu2. Similarly primary recrystallization, which occurs between 190 and 220 °C in UFG-Cu1, is shifted to remarkably higher temperatures (300–400 °C) in UFG-Cu2. The main decrease of the concentration of microvoids was found in temperature range from 400 to 500 °C in UFG-Cu1, when further growth of recrys-
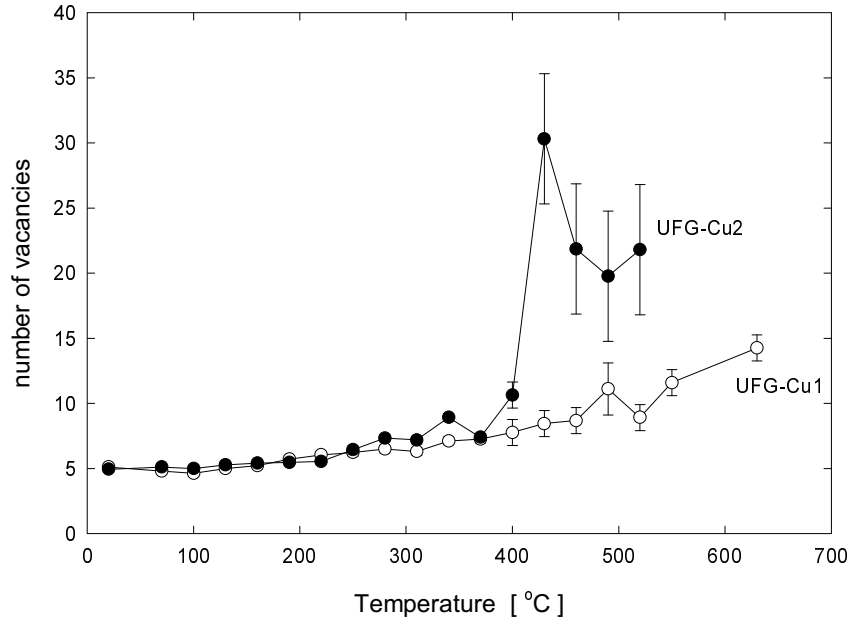
Figure 5.22 Free volume of microvoids determined using the theoretical calculations performed in appendix J as a function of annealing temperature. The free volume is expressed in the units of Cu monovacancy free volume.

tallized grain takes place. In the case of UFG-Cu2, main decrease of microvoids concentration occurs from 220 to 300 °C, i.e. during the abnormal grain growth.

5.5 Investigation of UFG Ni

Investigation of thermal stability of UFG Ni is described in Appendix K. Microstructure of the UFG-Ni specimen, see Tab. 5.2, and its evolution with increasing annealing temperature were studied by means of PL spectroscopy in the present work. Interpretation of the experimental data obtained by PL measurements was made using the DTM developed in Appendix J. The results obtained by PL spectroscopy were directly correlated with those determined by TEM, electrical resistometry, XRD, DSC and microhardness measurements [114] on the same specimens.

The present investigations have revealed out that similarly to UFG Cu, positrons are trapped at dislocations situated inside the distorted regions along grains and in microvoids inside the grains. Recovery of the UFG structure is realized by similar processes as in the case of UFG Cu. It means the abnormal grain growth, which is followed at higher temperatures by the primary recrystallization and further growth of the recrystallized grains. On the other hand, some remarkable differences from UFG Cu were found. Namely: a) the mean size of microvoids decreases during the primary recrystallization, which is the opposite behavior than in UFG Cu, b) additional microvoids and probably also dislocations are introduced into the UFG Ni annealed above the Curie temperature (358 °C) due to the magnetostriction phenomenon. Detailed explanation of the processes, which take place during isochronal annealing of UFG Ni specimens, is given in the appendix K.

Comparison of the results obtained on UFG Cu and UFG Ni specimens indicates strongly that temperature stability of UFG structure substantially depends on initial grain size and, thereby, on conditions of specimens preparation, see Tab. 5.2. The primary recrystallization is shifted to
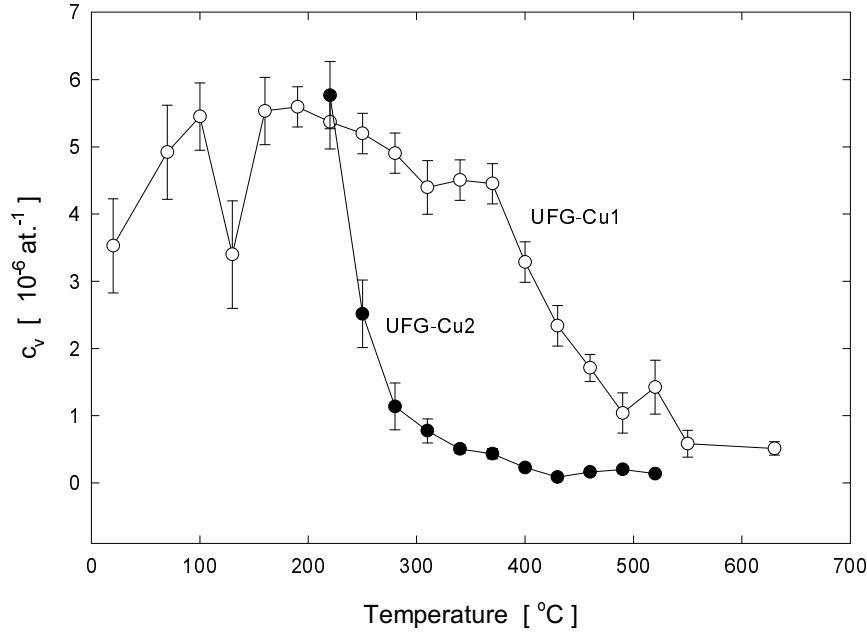
Figure 5.23 Temperature dependence of the mean concentration of microvoids c_v determined for UFG-Cu1 and UFG-Cu2 using the DTM.

remarkably lower temperatures in UFG-Cu1 and UFG-Ni specimens, i.e. specimens with smaller initial grain size, see Tab. 5.2.

5.6 Comparison of Defects in UFG and NC Materials

NC materials are conventionally prepared by GCM and similar techniques. On the other hand, UFG materials studied in the present work were prepared by severe plastic deformation (SPD). The principal difference between the techniques of preparation leads also to difference between defects present in the NC and the UFG materials. It is clear from Tab. 5.1 and results obtained in the present work that two main kinds of defects can be found in both materials. Namely, (i) defects with free volume similar to the monovacancy free volume and (ii) larger defects with free volume corresponding to that of a few monovacancies.

Regarding the first type of defects, our investigations, see appendixes I and J, have revealed high number of dislocations situated along grain boundaries in the UFG materials prepared by SPD. Positrons are trapped at vacancies associated with dislocation line or in jog of dislocation, see section 2.8.3 and their lifetime is only slightly shorter than that for a monovacancy. Thus, dislocations (and point defects bound to them) represent the defects of type (i) with free volume comparable to monovacancy in the UFG materials prepared by SPD. On the other hand, it is known that dislocations are unstable in NC materials due to very small grain sizes of a few nanometer. Therefore, majority of authors suggest that in the case of NC materials positrons are trapped at vacancy-like defects ("missing atom") situated inside the interfaces between grains.

In this paragraph, we will consider the second type of defects, type (ii), i.e. defects with free volume comparable with that of a few monovacancies. Looking in Tab. 5.1, one can see
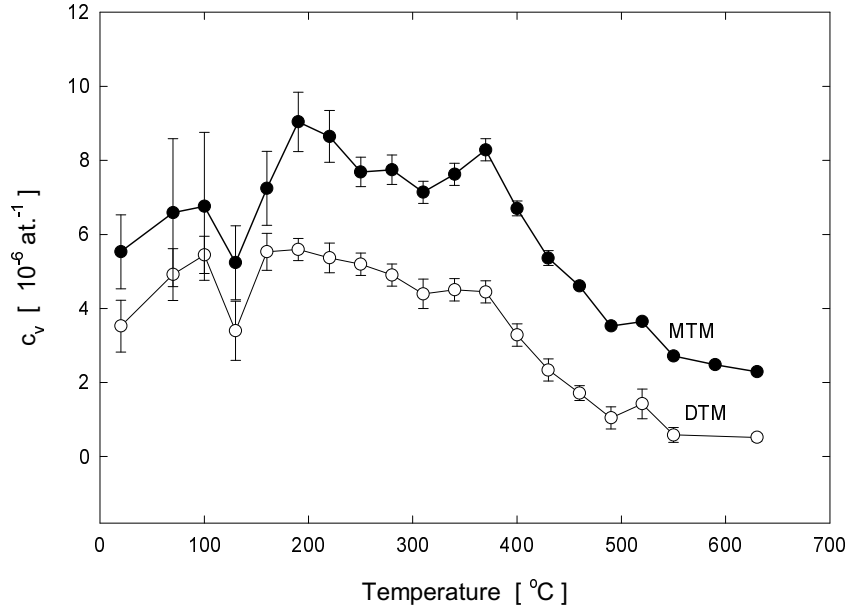
202

Figure 5.24 Comparison temperature dependence of the mean concentration of the microvoids obtained using the MTM with that determined by the DTM.

that lifetime of positrons trapped in this kind of defects is somehow higher for the NC materials compared to the UFG ones. In the case of the NC materials it is assumed that these defects are situated at triple junctions (triple points) of the interfaces. On the other hand, in the case of the UFG materials studied in the present work these defects were identified as microvoids distributed homogeneously throughout grains, see appendix J.

One can make following simple estimation. Let us consider typical NC and UFG copper and assume for a moment that the defects (ii) are situated in triple points in both the materials. We approximate a grain by a cube with side a, then there is one triple point per grain. Thus atomic concentration of the triple points c_t can be expressed

$$c_t = \frac{1}{a^3 n_{Cu}}, \tag{5.1}$$

where n_{Cu} is atom density, i.e. number of atoms in unit of volume. Firstly we make this estimation for typical NC material with grain size $a = 10$ nm. In such a case we obtained $c_t = 1.2 \times 10^{-5}$ at.$^{-1}$. Further we assume that one defect of type (ii) is situated at each triple point. Free volume of these defect corresponds to that of five vacancies. Under these assumption, we can calculate the positron trapping K for these defects.

$$K = c_t n \nu_{1v}, \tag{5.2}$$

where $n = 5$ and ν_{1v} denotes the specific positron trapping rate for monovacancy. For typical NC copper, we obtained $K = 7 \times 10^9$ s^{-1}. This trapping rate is comparable with the copper bulk annihilation rate $\lambda_B = 8.8 \times 10^9$ s^{-1}. Secondly we make the same estimation for typical UFG copper with grain size $a = 100$ nm. For such material we obtained $K = 7 \times 10^6$ s^{-1}, which is three order of magnitude lower than the bulk annihilation rate. Thus, contrary to NC materials, concentration of defects situated in the triple points is too low to represent noticeable contribution in PL spectra for UFG materials. Hence, this simple estimation supports our interpretation regarding microvoids in UFG materials, see appendix J.

We conclude that despite the similar PL spectra, defects in NC and UFG materials differ substantially.

5.7 Summary

Investigations of microstructure of UFG Cu and Ni prepared by SPD and its thermal evolution were performed in the present work. The specimens were studied by means of PL spectroscopy correlated with TEM and XRD measurements. Main results obtained in the present work can be briefly summarized into following items:

(i) The UFG specimens exhibit fragmented structure with non-distorted regions (grain interiors) separated by distorted layers along GBs. The non-distorted regions are almost free of dislocations ($\varrho_D \approx 10^{12}$ m^{-2}). On the other hand, dislocation density inside the distorted regions is high ($\varrho_D \geq 10^{15}$ m^{-2}).

(ii) Positrons are trapped at dislocations inside the distorted regions, which represent main positron traps, and in the microvoids distributed homogeneously throughout the grains.

(iii) Size of the microvoids is comparable to five vacancies in as-prepared UFG Cu specimens. In the case of as-prepared UFG Ni specimen, the size of the microvoids is comparable to ten vacancies.

(iv) Recovery of UFG structure involves similar processes in all UFG specimens studied. The recovery starts from the abnormal grain growth, where isolated recrystallized grains are formed in the deformed matrix. At higher annealing temperatures it is followed by the primary recrystallization and further growth of the recrystallized grains.

(v) The mean dislocation density in recrystallized specimens lies bellow 10^{13} m^{-2}, which is close to the lower sensitivity limit of PL spectroscopy. However, positrons are trapped in vacancy-like defects at equilibrium GBs, which contribute to PL spectra by a component with lifetime very similar to that of positrons trapped at dislocations. Change of the type of traps during the primary recrystallization is reflected by abrupt increase of the corresponding trapping rate.

(vi) Initial grain size in the as-prepared specimens, which depends on the hydrostatic pressure applied during preparation procedure, affects substantially thermal stability of the UFG materials. In the UFG specimens with smaller initial grain size the primary recrystallization is shifted to remarkably lower annealing temperatures.

(vii) The diffusion trapping model (DTM), which explicitly takes into account specific structure of UFG materials, was developed in the present work and successfully applied to interpretation of experimental PL data obtained on the UFG Cu and Ni. The DTM allows for calculation of important physical characteristics, e.g. size of the non-distorted regions, volume fraction of distorted regions, dislocation density, concentration of the microvoids and activation energy of the primary recrystallization, of the studied specimens from experimental PL data.

(viii) Using the DTM we have found that main increase of grain size accompanied by disappearance of the distorted regions occurs during the primary recrystallization. In the case of UFG Cu specimens, the activation energies of the primary recrystallization calculated using the DTM agree well with that for migration of equilibrium grain boundaries in coarse grained copper.

(ix) The mean size of the microvoids increases with temperature in both the UFG Cu materials studied in the present work. On the other hand, opposite behavior, i.e. decrease of the mean size of the microvoids during the primary recrystallization, was found in UFG Ni.

(x) Additional microvoids and probably also dislocations are introduced into UFG Ni specimen after annealing above the Curie temperature (358 °C) due to the magnetostriction phenomena.

The present work proved PL spectroscopy as a powerful tool for investigation of thermal stability of UFG materials. Application of the DTM on PL data and correlation of obtained results with those determined by other techniques, particularly TEM and XRD, allows for detailed description of processes, which take place during thermal recovery of UFG materials.

An interesting topic to which further investigation should be focused is influence of ceramic nanoparticles incorporated into a UFG material on its thermal stability. It is expected that the ceramic nanoparticles can serve as barriers for grain growth. Therefore, the primary recrystallization in UFG specimens with the ceramic nanoparticles may be shifted to higher temperatures. The advantageous mechanical and physical properties of the UFG materials is connected with the UFG structure. Therefore, extended stability of the UFG structure to higher annealing temperatures is very attractive for further exploitation of UFG materials in industry. In order to understand influence of the ceramic nanoparticles to recovery of the UFG structure, detailed investigations of microstructural thermal evolution on atomic scale are necessary. The experimental techniques and theoretical apparatus developed in the present work can be advantageously exploited in these investigations.

Appendix I

The paper was published in *Acta Physica Polonica A* **95**, 445 (1999).

Appendix J

The paper was submitted to *Physical Review B*.

Appendix K

The paper was submitted to *Material Science and Engineering A*.

6 Positron Annihilation Spectroscopy and Teaching of Physics

As was discussed in details in chapters 2, 3, positron annihilation spectroscopy proved itself as a powerful tool for investigations of solids [2, 58]. In particular, PAS is ideal method for study of lattice defects due to high sensitivity of positrons to open volume defects as vacancies, vacancy clusters, voids, dislocations, grain boundaries etc. PAS allows for identification of individual types of defects in material as well as determination of their density. Size of point open volume defects lies usually well below 10 nm, which makes them practically invisible by direct conventional techniques of solid state physics as e.g. transmission electron microscopy (TEM). Schematic diagram of applicability of PAS and other techniques as a function of defect size and density versus depth in material is shown in Fig. 6.1. Hence, PAS provides unique information regarding concentration,
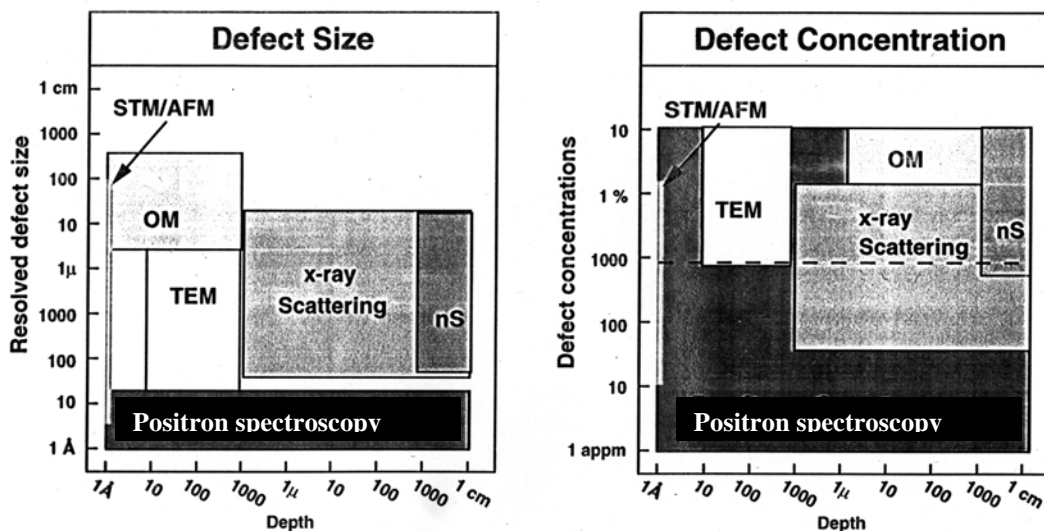

Figure 6.1 Schematic description of range of applicability of PAS [136]. The abbreviation OM means optical microscopy, nS is neutron scattering and STM/AFM denotes scanning tunneling microscopy/atom-probe field-ion microscopy.

arrangement, mutual interaction and local electronic structure of these defects in various materials. Contrary to experimental techniques capable of visualization of microstructure as TEM, high-resolution TEM, field-ion microscopy (FIM) and atom-probe FIM, which give information about local arrangement at one point of specimen, PAS provides microstructure information integrated through macroscopic volume of the specimen. Thus, PAS represents a non-local experimental technique sensitive to lattice defects at atomic scale. Moreover, contrary to the techniques listed above, PAS is non-destructive technique, which requires no special preparation procedure for the specimens studied. Presently well established theory of positron annihilation is available. Especially in the case of metallic materials it is possible to perform ab initio calculations of positron parameters for various defects and atomic arrangements [39, 3]. It allows for direct correlation of

experimental results with theoretical models of corresponding materials.

The PAS technique was firstly applied to investigation of condensed matter in 1950. The advantageous features described above lead to stormy expansion of PAS and its exploitation in investigation of variety of materials. The development of PAS involves substantial improving of timing resolution of positron-lifetime (PL) spectrometers from initial 300 ps to timing resolution about 150 ps (FWHM for ^{22}Na) available on the best PL spectrometers in the present state-of-art, see appendix A. The significant improvement of timing resolution enhances the power of PL spectroscopy as allows for resolving of higher number of components in PL spectra with substantially better precision and, thereby, study of more complex materials. The increase of the timing resolution was achieved by use of fast BaF_2 [85, 137] or plastic scintillators [138, 84] and introduction of dynode timing for fast photomultipliers [139, 140]. Use of nuclear modular electronics (NIM) and introduction of the constant fraction timing [141] has also significant positive impact on development of PL spectroscopy. Similarly use of high-purity germanium detectors has substantially improved the energy resolution of detectors used in Doppler-broadening measurements [2]. Simultaneously with improvement of experimental techniques, development of decomposition procedure for PL spectra [142, 143] and models for interpretation of the obtained parameters [47, 2] have took place. Moreover, theory of positron annihilation based on local density approximation was developed [39, 3]. Presently, a number of theoretical positron calculation was performed and calculated parameters agree well with the experiment especially in the case of metals [3, 39, 50].

In the present time PAS is routinely used for investigations of metallic materials. PAS was successfully applied to study of a large number of phenomena in metals including investigation of equilibrium and non-equilibrium defects, phase transitions, thermal recovery of defect structure, radiation damage, precipitation effects, chemical corrosion etc. Important advantage of PAS is its ability to study evolution of microstructure on one specimen subjected for example to isochronal or isothermal annealing, ageing, deformation, radiation etc. Moreover wide range of effects including heat treatment, deformation, etc, can be studied directly by in situ PAS measurements. Among number of important successes one should mention determination of the formation and migration energy of equilibrium point defects [47] as well as explanation of processes which take place during the stage III in recovery of non-equilibrium structure of deformed irradiated or quenched metals [43]. Beside metals, extensive exploitation of PAS in study of semiconductors and polymers has occurred for the last decade. One should also mention monoenergetical positron beams [144], which allow for investigations of thin films and surfaces, as number of these devices in world continuously increases.

The large expansion of PAS in the field of solid-state physics and materials science is accompanied by removal of some difficulties connected with this technique. For example, the PL spectrometer was hand made in the past, i.e. some experiences with nuclear γ-ray timing measurements were necessary. In the present time PL spectrometers with timing resolution bellow 200 ps, which represents a "middle-class" of these instruments, are commercially available [145]. Clearly, it leads to further expansion of this technique. Unfortunately, the knowledge about PAS among the solid-state physicists and material scientists is still relatively poor. However, one should expect that this community will be always more frequently confronted with PAS investigations. As interpretation of PAS results is not easy and requires some familiarity at least with the principles of the method, it is desirable to improve knowledge about PAS among physicists. An ideal way how to achieve it is to introduce PAS among the conventional experimental techniques, which are taught in lectures on solid-state physics. It is reasonable to exploit the PAS spectrometers, especially the PL spectrometer with superior timing parameters, available at the PAS laboratory of Department of Low-Temperature Physics in Charles University to provide students with practical experiences with PAS.

This purpose was realized by insertion of PAS measurement to laboratory works for students of physics. In the frame of the laboratory work the students have studied defects in selected metallic materials by means of PL spectroscopy. The students have obtained some practical experiences with PL measurements and decomposition of experimental PL spectra. Finally, they have used the simple trapping model (STM) for interpretation of the results. In order to provide students with basic introduction to PL spectroscopy including the description of this technique, its

physical principles, experimental setup, decomposition of spectra and interpretation of PL results using STM was written in the present work. This paper includes also an illustrative example of application of PL spectroscopy to plastically deformed copper. The paper was written in Czech language and was published in the journal "Pokroky matematiky, fyziky a astronomie" . This journal is devoted to simple and intelligible explanation of interesting topics of physics and mathematics and is available for wide range of readers including physicists, teachers of physics at high, secondary and basic schools, students as well as other people, which are interested in science. Thus, it is believed that this paper, which represents first publication of this kind regarding popularization of PL spectroscopy written in Czech language, serves not only as introduction for students interested in laboratory work with our spectrometer, but may also improve common knowledge about PL spectroscopy among relatively wide group of people. The introductory paper is included in the present work in Appendix L.

On the base of positive experiences with student's laboratory works on PL spectrometer in our laboratory, we have decided to enhance the role of PAS in teaching of physics and education of young physicists. This project involves development of freely accessible interactive teaching program (virtual spectrometer and modeling program), enables a user to simulate real measurement and find out majority of practical aspects and the experiment as well as further elaboration and interpretation of obtained results. Note that contrary to the real measurement, which takes usually a few days and is relatively expensive, the results of virtual experiment are obtained almost immediately and practically free of charge. Further topic of the project is modernization and enhancement of the laboratory work in our spectrometers. After training in virtual experiments, the students will be allowed to become familiar with real high-quality spectrometers and also with new attractive materials, which are currently studied in our laboratory. The ultra-fine grained metals prepared by severe plastic deformation, which have been investigated in the present work, see chapter 5, are a good example. The project will be realized in the year 2001 due to financial support of the Ministry of Education of Czech Republic. It is expected that the methodological work made in the present work, i.e. development of user-friendly software for accumulation and visualization of PAS spectra on personal computer as well as utilities for elaboration of the spectra, will be exploited in this project. Moreover, the experimental and theoretical results obtained in the present work, especially on deformed and UFG materials, are suitable for exploitation in the project. Hence, the present work enables improvement of student's laboratory works as well as education of students and young scientists in the field of positron annihilation.

Appendix L

The paper was published in *Pokroky matematiky, fyziky a astronomie* **44**, 201 (1999).

7 Final Conclusions

The scientific work made in the present thesis may be divided into three parts:

(a) methodological work, see chapter 3

(b) investigation of reactor pressure vessel (RPV) steels and ultra-fine grained metals, see chapters 4,5

(c) positron annihilation spectroscopy (PAS) in teaching of physics, see chapter 6

The present thesis is based on the results explained in the papers published or submitted to publication in the international physics journals. The papers are included in the present thesis as appendixes A thru L.

7.1 Methodological Work

- The deterioration of timing characteristics of high-resolution positron-lifetime spectrometer was studied in the present work. The mechanism of this deterioration was explained and procedures for its remedy were developed and successfully applied to our PL spectrometer, see appendix A.

- Alternative configuration of PL spectrometer using energy summing in the slow branch was proposed and successfully exploited in our spectrometer, see appendix B. Using this configuration significantly higher coincidence count rate is achieved with no deterioration of the excellent timing properties.

- A new technique for time calibration of PL spectrometer, which is generally applicable to all timing measurements, was developed and tested in the present work, see appendix D. The new technique enables precise integral as well as differential time calibration. In addition, it may be easily performed with modular nuclear electronics conventionally used in timing measurements, no additional specialized devices are necessary.

- The three-detector PL spectrometer was proposed and build in the present work, see appendix C. This spectrometer uses triple coincidence of γ-rays, which makes possible to separate the ^{22}Na annihilation events from ^{60}Co prompt coincidences. The three-detector spectrometer combines energetic and timing selection of γ-rays and suppress substantially the ^{60}Co prompt contribution on PL spectra. It makes possible PL investigation of RPV steels irradiated by fast neutrons to relatively high fluence of 10^{25} m^{-2} (10 years of irradiation at ordinary operating conditions of nuclear power plant).

7.2 Investigations of RPV Steels and UFG Materials

- Various types of RPV steels, which are used in reactor vessels of nuclear power plants were studied in the present work. Firstly, detailed microstructure characterization of non-irradiated specimens was made. Then specimens irradiated by fast neutrons at various conditions (fluence and flux) were investigated. The obtained results are given in chapter 4 and appendixes E, G and H. A short summary of these results can be found in section 4.3

- Microstructure of UFG Cu and Ni prepared by severe plastic deformation (SPD) was studied in details in the present work. Subsequently the specimens were subjected to isochronal annealing and thermal evolution of microstructure was investigated. The results are described

274

in chapter 5 and appendixes I, J and K. A short summary of the main results obtained on these materials can be found in section 5.7

- The common feature of both the RPV steels and UFG materials is presence of strongly non-homogeneously distributed dislocations, which represents the main positrons traps. In both kinds of materials regions with low dislocation density are separated by distorted regions with high number of dislocations. Mainly due to this fact it is not possible to use the simple trapping model (STM). Therefore new model for interpretation of PL spectra was developed in the present work. The modified trapping model (MTM), which is described in details in appendix F and was successfully applied to RPV steels, see chapter 4, as well as UFG Cu, see appendix I, represents reasonable but relatively rough approximation of the material. Improvement of this model leads to diffusion trapping model (DTM), which was also developed in the present work and is described in appendix J. Successful application of DTM on UFG Cu and Ni is given in appendixes J and K, respectively.

- Another common feature of microstructure of irradiated RPV steels and UFG materials is presence of microvoids (vacancy clusters), which represent another trapping sites for positrons. The microvoids are induced into RPV steels by neutron irradiation, while in the case of UFG materials they are created by severe plastic deformation. It should be pointed out that investigations of the microvoids have clearly shown the benefit of PAS in such studies. PAS enables to determine the mean size of the microvoids as well as their concentration. On the other hand, the microvoids cannot be detected by XRD, because of their small size they are invisible by TEM and are hardy detectable also by other techniques due to their low concentration.

- It has to be pointed out that the investigations or RPV steels and UFG materials performed in the present work were possible only due to the excellent timing resolution of the PL spectrometer and due to development of the three-detector PL spectrometer for investigation of irradiated RPV steels. The superior timing resolution is crucial for proper determination of the short free positron component (lifetime well below 100 ps), which usually has small intensity. Proper lifetime and intensity of the free positron component is necessary for application of the trapping models.

- In the case of irradiated RPV steels it is absolutely necessary to remove the ^{60}Co prompt contribution, otherwise it completely distorts the experimental PL spectra as was shown by our simulations. Thus, PL investigations of RPV steels irradiated to high fluencies is impossible without the three-detector spectrometer. The results obtained in the present work represent first successful application of the three-detector PL spectrometer on study of irradiated RPV steels.

- The investigations performed in the present work have shown that PAS is suitable for study of RPV steels and UFG materials. Moreover, the theoretical models developed in the present work can be exploited in further investigations of these as well as similar materials.

7.3   Teaching of Physics

- A short paper, which explains principles of PL spectroscopy and its exploitation in physics of metallic materials was written in the present work, see appendix L. This paper is the first description of PL spectroscopy in Czech language, which is dedicated to students as well as to relatively wide range of people, which are interested in solid-state physics.

- The methodological work made in the present thesis will be exploited in the project "Exploitation of Positron Spectroscopy in Education of Students and Young Scientists" supported by The Ministry of Education of Czech Republic, which is running in the year 2001. Moreover, it is expected that the experimental and theoretical results, especially regarding

the deformed and UFG materials and the models for interpretation of PL data for these materials, obtained in the present work will be advantageously used in the project, see chapter 6.

Bibliography

[1] P. Hautojärvi, in: *Positrons in Solids, Topics in Current Physics vol.,* 12, Ed. P. Hautojärvi, Springer-Verlag, Berlin 1979, p. 1.

[2] P. Hautojärvi, C. Corbel, in: *Proceedings of the International School of Physics "Enrico Fermi",* Course CXXV, Ed. A. Dupasquier, A.P. Mills, IOS Press, Varenna 1995, p. 491.

[3] M.J. Puska, R.M. Nieminen, *Rev. Mod. Phys.* **66**, 841 (1994).

[4] L.M. Davies, *Int. Journal of Pressure Vessel and Piping* **76**, 163 (1999).

[5] W.K. Phythian, C.A. English, *J. Nucl. Mater.* **205**, 162 (1993).

[6] R. Birringer, *Mat. Sci. Eng. A* **117**, 33 (1989).

[7] R.Z. Valiev, A.V. Korznikov, R.R. Mulyukov, *Mat. Sci. Eng. A* **168**, 141 (1993).

[8] R.Z. Valiev, *Mat. Sci. Eng. A* **234-236**, 59 (1998).

[9] H.-E. Schaefer, R. Würschum, R. Birringer, H. Gleiter, *Phys. Rev. B* **38**, 9545 (1988).

[10] R. Würschum, M. Scheytt, H.-E. Schaefer, *phys. stat. sol. (a)* **102**, 119 (1987).

[11] Yu.M. Shirokov, N.P. Yudin, *Yadernaya Fizika,* Nauka, Moskva 1980.

[12] C.M. Lederer, V.S. Shirley (editors) *Table of Isotopes,* Seventh Edition, John Wiley & sons, INC., New York 1978

[13] I.K. MacKenzie, in: *Proceedings of the International School of Physics "Enrico Fermi",* Course LXXXIII, Ed. W. Brandt, A. Dupasquier, North-Holland Publishing Company, Varenna 1983, p. 196.

[14] A. Perkins, J.P. Carbotte, *Phys. Rev. B* **1**, 101 (1970).

[15] S. Valkealahti, R.M. Nieminen, *Appl. Phys. A* **32**, 95 (1983).

[16] R.H. Ritchie, *Phys. Rev.* **114**, 644 (1959).

[17] K.O. Jensen, A. Walker, *J. Phys.: Condens. Matter* **2**, 9757 (1990).

[18] W. Brandt, in: *Proceedings of the International School of Physics "Enrico Fermi",* Course LXXXIII, Ed. W. Brandt, A. Dupasquier, North-Holland Publishing Company, Varenna 1983, p. 1.

[19] R.M. Nieminen, J. Oliva, *Phys. Rev. B* **22**, 2226 (1980).

[20] W. Brandt, R. Paulin, *Phys. Rev. B* **15**, 2511 (1977).

[21] E. Soininen, H. Huomo, P.A. Huttunen, J. Mäkinen, A. Vehanen, P. Hautojärvi, *Phys. Rev. B* **41**, 6227 (1990).

[22] A.P. Mills, in: *Proceedings of the International School of Physics "Enrico Fermi",* Course LXXXIII, Ed. W. Brandt, A. Dupasquier, North-Holland Publishing Company, Varenna 1983, p. 432.

[23] A. Seeger, J. Major, F. Jaggy in *Positron Annihilation,* Ed. P.C. Jain, R.M. Singru, K.P. Gopinathan, World Scientific, Singapore 1985, p. 137.

[24] V.I. Goldanskii, *Atomic Energy Rev.* **6**, 3 (1968).

[25] A. Dupasquier, in: *Proceedings of the International School of Physics "Enrico Fermi"*, Course LXXXIII, Ed. W. Brandt, A. Dupasquier, North-Holland Publishing Company, Varenna 1983, p. 510.

[26] O. Megensen, *J. Chem. Phys.* **60**, 998 (1974).

[27] B. Bergensen, E. Pajane, *Appl. Phys.* **4**, 25 (1974).

[28] R.M. Nieminen, J. Laakkonen, *Apll. Phys.* **20**, 181 (1979).

[29] J. Bardeen, W. Shockley, *Phys. Rev.* **80**, 72 (1950).

[30] R.M. Nieminen, in: *Proceedings of the International School of Physics "Enrico Fermi"*, Course LXXXIII, Ed. W. Brandt, A. Dupasquier, North-Holland Publishing Company, Varenna 1983, p. 359.

[31] B. Bergensen, E. Pajane, P. Kubica, M.J. Stott, C.D. Hodges, *Solid State Commun.* **15**, 1377 (1974).

[32] R.O. Jones, O. Gunnarson, *Rev. Mod. Phys.* **61**, 689 (1989).

[33] R.M. Nieminen, E. Boroński, L. Lantto, *Phys. Rev. B* **32**, 1377 (1985).

[34] E. Boroński, R.M. Nieminen, *Phys. Rev. B* **34**, 3820 (1986).

[35] W. Kohn, L.J. Sham, *Phys. Rev. A* **140**, 1133 (1965).

[36] D.M. Ceperley, B.J. Alder, *Phys. Rev. Lett.* **45**, 566 (1980).

[37] J.P. Perdew, A. Zunger, *Phys. Rev. B* **23**, 5048 (1981).

[38] J.P. Perdew, Y. Wang, *Phys. Rev. B* **45**, 13244 (1992).

[39] R.M. Nieminen, in: *Proceedings of the International School of Physics "Enrico Fermi"*, Course CXXV, Ed. A. Dupasquier, A.P. Mills, IOS Press, Varenna 1995, p. 443.

[40] B. Barbiellini, M.J. Puska, T. Torsti, R.M. Nieminen, *Phys. Rev. B* **51**, 7341 (1995).

[41] A. Seeger, F. Banhart, *phys. stat. sol. (a)* **102**, 171 (1987).

[42] K.O. Jensen, M. Eldrup, S. Lidenroth, J.H. Evans, in: *Proceedings of the 8th International Conference on Positron Annihilation*, Ed. L. Dorikens-Vanpraet, M. Dorikens, D. Segers, World Scientific, Singapore 1988.

[43] A. Vehanen, P. Hautojärvi, J. Johanson, J. Yli-Kauppila, P. Moser, *Phys. Rev. B* **25**, 762 (1982).

[44] A. Dupasquier, R. Romero, A. Somoza, *Phys. Rev. B* **48**, 9235 (1993).

[45] G. Brauer, L. Liszkay, B. Molnar, R. Krause, *Nucl. Eng. Des.* **127**, 47 (1991).

[46] C.H. Hodges, *J. Phys. F: Met. Phys.* **4**, L230 (1974).

[47] R.N. West, in: *Positrons in Solids, Topics in Current Physics vol.*, 12, Ed. P. Hautojärvi, Springer-Verlag, Berlin 1979, p. 89.

[48] C.H. Hodges, *Phys. Rev. Lett.* **25**, 284 (1970).

[49] W. Brandt, R. Paulin, *Phys. Rev. B* **5**, 2430 (1972).

[50] M.J. Puska, R.M. Nieminen, *J. Phys. F: Met. Phys.* **13**, 333 (1983).

[51] J.-E. Kluin, Th. Hehenkamp, *Phys. Rev. B* **44**, 11597 (1991).

[52] K. Petersen, in: *Proceedings of the International School of Physics "Enrico Fermi"*, Course LXXXIII, Ed. W. Brandt, A. Dupasquier, North-Holland Publishing Company, Varenna 1983, p. 298.

[53] S. Mantl, W. Kesternich, W. Triftshäuser, *J. Nucl. Mater.* **69-70**, 593 (1987).

[54] R.W. Siegel in *Positron Annihilation,* Ed. P.G. Coleman, S.C. Sharma, L.M. Diana, North Holland, Amsterdam 1982, p. 351.

[55] H.-E. Schaefer in *Positron Annihilation,* Ed. P.G. Coleman, S.C. Sharma, L.M. Diana, North Holland, Amsterdam 1982, p. 369.

[56] K. Hinode, S. Tanigawa, M. Doyama, *Radiat. Eff.* **32**, 73 (1977).

[57] H. Häkkinen, S. Mäkinen, M. Manninen, *Phys. Rev. B* **41**, 12441 (1990).

[58] P. Hautojärvi, T. Judin, A. Vehanen, J. Yli-Kauppila, J. Johanson, J. Verdone, P. Moser, *Solid State Commun.* **29**, 855 (1979).

[59] Y. Kamimura, F. Hori, T.Tsutsumi, E. Kuramoto, *Mater. Sci. Forum* **175-178**, 403 (1995).

[60] M.J. Fluss, L.C. Smedsjaer, M.K. Chason, D.G. Legnini, R.W. Siegel, *Phys. Rev. B* **17**, 3444 (1978).

[61] P. Jena, M.J. Ponnambalam, M. Mainninen, *Phys. Rev. B* **24**, 2884 (1981).

[62] R.P. Gupta, R.W. Siegel, *Phys. Rev. B* **22**, 1572 (1980).

[63] T. McMullen, R.J. Douglas, N. Etherington, B.T.A. McKee, A.T. Steward, E. Zaremba, *J. Phys. Met. F: Met. Phys.* **11**, 1435 (1981).

[64] G. Dlubek, O. Brümmer, N. Meyendorf, P. Hautojärvi, A. Vehanen, J. Yli-Kauppila, *J. Phys. F: Met. Phys.* **9**, 1961 (1979).

[65] J. Johansson, A. Vehanen, J. Yli-Kauppila, P. Hautojärvi, P. Moser, *Radiat. Eff. Lett.* **58**, 31 (1981).

[66] J.W. Martin, R. Paetsch, *J. Phys. F: Met. Phys.* **2**, 997 (1972).

[67] L.C. Smedskjaer, M. Manninen, M.J. Fluss, *J. Phys. F: Met. Phys.* **10**, 2237 (1980).

[68] K. Petersen, I.A. Repin, G. Trumpy, *J. Phys.: Condens. Matter.* **8**, 2815 (1996).

[69] C. Hidalgo, G. González-Doncel, S. Linderoth, J.S. Juan, *Phys. Rev. B* **45**, 7017 (1992).

[70] Y.K. Park, J.T. Waber, M. Meshii, C.L. Snead, C.G. Park, *Phys. Rev. B* **34**, 823 (1986).

[71] P. Hautojärvi, A. Tamminen, P. Jauho, *Phys. Rev. Lett.* **24**, 459 (1970).

[72] B.T.A. McKee, S. Saimoto, A.T. Stewart, M.J. Stott, *Can. J. Phys.* **52**, 759 (1974).

[73] Y. Kamimura, T. Tsutsumi, E. Kuramoto, *Phys. Rev. B* **52**, 879 (1995).

[74] M. Doyama, R.M.J. Cotterill in *Proceedings of the 5th International Conference on Positron Annihilation, Japan, 1979* Ed. R.R. Hasiguti, K. Fujiwara, Japan Institute of Metals, Sendai 1979, p. 89.

[75] M. Iwami, E. Hashimoto, Y. Ueda, *J. Phys.: Condens. Matter.* **7**, 9935 (1995).

[76] C. Dauwe, M. Dorikens, L. Dorikens-Vanpraet, D. Segers, *Appl. Phys.* **5**, 117 (1974).

[77] T.K. Lepistö,V.-T. Kuokkala in *Proceedings of the Vth RisøInternational Symposium on Metalurgy and Materials Science,* Ed. N.H. Andersen, M. Eldrup, N. Hansen, D.J. Jensen, T. Leffers, H. Lillholt, O.B. Pedersen, B.N. Singh, RisøNational Laboratory, Risø, Denmark 1984.

[78] C. Hildago, S. Linderoth, G. González-Doncel, J.S. Juan in *Proceedings of the 8th International Conference on Positron Annihilation, Ghent, 1988,* Ed. L. Dorikens-Vanpraet, M. Dorikens, D. Segers, World Scientific, Singapore 1989.

[79] R.M.J. Cotterill, K. Petersen, G. Trumpy, J. Träff, *J. Phys. F: Met. Phys.* **2**, 459 (1972).

[80] M.J. Puska, P. Lanki, R.M. Nieminen, *J. Phys.: Condens. Matter.* **1**, 6081 (1989).

[81] D.W. Gidley, W.E. Frieze, *Phys. Rev. Lett.* **60**, 1193 (1988).

[82] B. Bengtson, M. Moszyński, *Nucl. Instr. Meth.* **81**, 109 (1970).

[83] B. Bengtson, M. Moszyński, *Nucl. Instr. Meth.* **204**, 129 (1982).

[84] M. Moszyński, *Nucl. Instr. Meth. A* **337**, 154 (1993).

[85] M. Laval, M. Moszyński, R. Allemand, E. Cormoreche, P. Guinet, R. Odru, J. Vacher, *Nucl. Instr. Meth.* **206**, 169 (1983).

[86] C.F. Coleman, F.A. Smith, A.E. Hughes, *Harwell Report* **AERE-R8551** (1976).

[87] R.G. Helmer, M.A. Lee, *Nucl. Instr. Meth.* **178**, 499 (1980).

[88] L. Van Hoorebeke, A. Fabry, E. van Walle, J. Van de Velde, D. Segers, L. Dorikens-Vanpraet, *Nucl. Instr. Meth. A* **371**, 566 (1996).

[89] B.L. Eyre, J.R. Matthews, *J. Nucl. Mater.* **205**, 1 (1993).

[90] M.K. Miller, K.F. Russell, J. Kočík, E. Keilová, *J. Nucl. Mater.* **282**, 83 (2000).

[91] P. Hautojärvi, L. Pöllänen, A. Vehanen, J. Yli-Kauppila, *J. Nucl. Mater.* **114**, 250 (1983).

[92] C. Lopes Gil, A.P. De Lima, N. Ayres De Campos, J.V. Fernandes, G. Kögel, P. Speer, W. Triftshäuser, D. Pachur, *J. Nucl. Mater.* **161**, 1 (1989).

[93] Radiation Embrittlement and Surveillance of Nuclear Reactor Pressure Vessels, ed. L.E. Steele, ASTM-STP 819 (1983).

[94] G.R. Odette, *Scripta metall.* **17**, 1183 (1983).

[95] J. Kočík, E. Keilová, J. Čížek, I. Procházka in: METAL 2000, Proceedings of 9-th International Conference on Metalurgy (CD-ROM), May 2000 Ostrava, Czech Repiblic, Tanger Ltd., paper No.719.

[96] F.A. Smidt, J.A. Sprague, *ASTM STP* **529**, 78 (1973).

[97] M.K. Miller, S.S. Brenner, *Res. Mech.* **10**, 161 (1984).

[98] M.K. Miller, R. Jayaram, P.J. Othen, G. Brauer, *Appl. Surf. Sci.* **76& 77**, 242 (1994).

[99] B.A. Gurovich, E.A. Kuleshova, O.V. Lavrenchuk, K.E. Prikhodko, Ya.I. Shtrombakh, *J. Nul. Mater.* **264**, 333 (1999).

[100] F. Frisius, D. Büneman in: *Proceedings of Conference on Irradiation Behaviour of Metallic Materials for Fast Reactor Core Components* CEA, Ajaccio, 1979 p. 247.

[101] V. Slugeň, V. Magula, *Nucl. Eng. Des.* **186**, 323 (1998).

[102] G. Brauer, K. Popp, *phys. stat. sol. (a)* **102**, 79 (1987).

[103] K. Ghazi-Wakili, U. Zimmermann, J. Brunner, P. Tipping, W.B. Waeber, F. Heinrich, *phys. stat. sol. (a)* **102**, 153 (1987).

[104] F. Bečvář, Y. Jirásková, E. Keilová, J. Kočík, L. Lešták, I. Procházka, B. Sedlák, M. Šob, *Mat. Sci. Forum* **105-110**, 905 (1992).

[105] A. Hempel, M. Saneyasu, Z. Tang, M. Hasegawa, G. Brauer, A. Plazaola, S. Yamaguchi in: *Effects of Radiation on Materials:* 19th *International Symposium ASTM STP 1366* ed. A.B. Smith, C.D. Jones, American Society for Testing and Materials, West Conshohocken, 1998.

[106] J. Hascik, V. Slugeň, J. Lipka, M. Miglierini, R. Grone, I. Toth, K. Vitazek, L. Kupca, *International Conference on Pressure Vessel Technology* **Volume 1**, ASME (1996).

[107] S.E. Cumblidge, A.T. Motta, G.L. Catchen, MRS 96$^{'}$ Fall Meeting, Boston, 1996

[108] X. Zhu, R. Birringer, U. Herr, H. Gleiter, *Phys. Rev. B* **35**, 9085 (1987).

[109] C.G. Granqvist, R.A. Burmann, *J. Appl. Phys.* **47**, 2200 (1976).

[110] F.H. Froes, C. Suryanarayna, *J. Met.* **6**, 12 (1989).

[111] P.G. Sanders, J.R. Weertman, J.G. Barker, *J. Mater. Res.* **11**, 3110 (1996).

[112] R.Z. Valiev, R.K. Islamgaliev in: *Superplasticity and Superplastic Forming 1998,* ed. A.K. Ghosh, T.R. Bieler, The Minerals, Metals and Materials Society 1998, p. 117.

[113] V.Yu. Gertzman, R. Birringer, R.Z. Valiev, H. Gleiter, *Scripta Met. Mater.* **30**, 229 (1994).

[114] R.K. Islamgaliev, F. Chmelík, R. Kužel, *Mat. Sci. Eng. A* **237**, 43 (1997).

[115] R.Z. Valiev, E.V. Kozlov, YU.F. Ivanov, J. LIan, A.A. Nazarov, B. Baudelet, *Acta metall. mater.* **42**, 2467 (1994).

[116] H. Karch, R. Birringer, H. Gleiter, *Nature* **330**, 556 (1987).

[117] H. Schladitz, *Z. Metallkd.* **59**, 18 (1968).

[118] H.F.F. Wilsdorf, O. Inal, E. Murr, *Z. Metallkd.* **69**, 701 (1978).

[119] J. Horvath, R. Birringer, H. Gleiter, *Solid State Commun.* **62**, 319 (1987).

[120] R. Birringer, H. Hahn, H. Höfler, J. Karch, H. Gleiter in: *Diffusion and Defect Data,* Trans Tech, Aedermannsdorf, 1988, p. 17.

[121] H.J. Klam, H. Hahn, H. Gleiter, *Acta Metall.* **35**, 2101 (1987).

[122] R.Z. Valiev, I.V. Alexandrov, R.K. Islamgaliev in: Nanocrystalline Materials Science and Technology. NATO ASI, ed. G.M. Chow, N.I. Noskova, Kluwer Publ. 1998, p. 121.

[123] Ultrafine grained materials produced by severe plastic deformation. Special issue. Ed. R.Z. Valiev. Annales de chimie - Science des Materiaux. **21**, 369 (1996).

[124] R. Birringer, U. Herr, H. Gleiter, *Trans. Jpn. Inst. Met. Suppl.* **27**, 43 (1986).

[125] N.M. Amirkhanov, J.J. Bucki, R.K. Islamgaliev, K.J. Kurzydlowski, R.Z. Valiev. submitted to *Mat. Sci. Eng.*

[126] U. Herr, J. Jing, R. Birringer, U. Gonser, H. Gleiter, *Appl. Phys. Lett.* **50**, 472 (1987).

[127] M. Eldrup, P.G. Sanders, J.R. Weertman, *Mat. Sci. Forum* **255-257**, 436 (1997).

[128] D. Segers, S. Van Petegem, J.F. Löffler, H. Van Swygenhoven, W. Wagner, C. Dauwe, *NanoStructured Materials* **12**, 1059 (1999).

[129] H.-E. Schaefer, K. Reimann, W. Straub, F. Phillipp, H. Tanimoto, U. Brossman, R. Würschum, *Mat. Sci. Eng.* in press.

[130] J. Kuriplach, S. Van Petegem, M. Hou, E.E. Zhurkin, H. Van Swygenhoven, F. Dalla Torre, G. Van Tendeloo, M. Yandouzi, D. Schryvers, D. Segers, A.L. Morales, S. Ettaoussi, C. Dauwe, *Mat. Sci. Forum*, in press.

[131] R. Würschum, W. Greiner, R.Z. Valiev, M. Rapp, W. Sigle, O. Schneeweiss, H.-E. Schaefer, *Scr. Metal. Mater.* **25**, 2451 (1991).

[132] I.V. Alexandrov, K. Zhang, A.R. Kilmametov, K. Lu, R.Z. Valiev, *Mat. Sci. Eng. A* **234-236**, 321 (1997).

[133] R.K. Islamgaliev, *private communication.*

[134] J.P. Hirth and J. Lothe, Theory of Dislocations, New York, McGraw-Hill (1982).

[135] G. Dlubek, *Mat. Sci. Forum* **13-14**, 15 (1987).

[136] R. Howell, Physics Space Technology.

[137] H. Rajainmäki, *Appl. Phys. A* **42**, 205 (1987).

[138] B. Bengston, M. Moszyński, *Nucl. Instr. Meth.* **81**, 109 (1970).

[139] B. Bengston, M. Moszyński, *Nucl. Instr. Meth.* **204**, 129 (1982).

[140] J. de Vries, *Positron Lifetime Technique with Applications in Materials Science,* Delftse Universitaire Pres, 1987.

[141] W.R. Leo, *Techniques for Nuclear and Particle Physics Experiments,* Springer-Verlag, Berlin 1987.

[142] I. Procházka, I. Novotný, F. Bečvář, *Mater. Sci. Forum* **255-257**, 772 (1997).

J. de Vries, F.E.T. Kelling, *Nucl. Instr. Meth. A* **262**, 385 (1987).

[143] P. Kirkegaard, M. Eldrup, O.E. Mogensen, N.J. Pedersen, *Comput. Phys. Commun.* **23**, 307 (1981).

[144] P.J. Schultz, K.G. Lynn, *Rev. Mod. Phys.* **60**, 701 (1988).

[145] Perkin-Elmer Instruments, cataloque 2001 (`www.par-online.com`).